NASA Technical Paper 1411

# Ion Confinement and Transport in a Toroidal Plasma With Externally Imposed Radial Electric Fields

J. Reece Roth, Walter M. Krawczonek,
Edward J. Powers, Young C. Kim,
and Jae Y. Hong

MARCH 1979

NASA

NASA Technical Paper 1411

# Ion Confinement and Transport in a Toroidal Plasma With Externally Imposed Radial Electric Fields

J. Reece Roth, Walter M. Krawczonek,
Edward J. Powers, Young C. Kim,
and Jae Y. Hong
*Lewis Research Center*
*Cleveland, Ohio*

National Aeronautics
and Space Administration

**Scientific and Technical
Information Office**

1979

CONTENTS

## SUMMARY

In the NASA Lewis bumpy-torus experiment, strong electric fields were imposed along the minor radius of the toroidal plasma by biasing it with electrodes maintained at kilovolt potentials. Digitally implemented spectral analysis techniques were used to experimentally investigate the characteristics of the plasma fluctuations and the frequency-dependent, fluctuation-induced transport of ions across the toroidal magnetic field. Plasma fluctuations became increasingly turbulent with higher densities and longer particle confinement times, and the amplitude statistics of both potential and ion density fluctuations became Gaussian. Coherent low-frequency disturbances characteristic of various magnetohydrodynamic instabilities were absent in the high-density, well-confined regime. High, direct-current, radial electric fields, with magnitudes up to 135 volts per centimeter, penetrated inward to at least one-half the plasma radius. When the electric field pointed radially inward, the ion transport was inward against a strong local density gradient, and the plasma density and confinement time were significantly enhanced. The radial transport along the electric field appeared to be consistent with fluctuation-induced transport and not with either a collisional Pedersen-current mechanism or the collisionless $\nabla E$ mechanism described by Cole. With negative electrode polarity, the particle confinement was consistent with a balance of two processes: a radial infusion of ions, in those sectors of the plasma not containing electrodes, that resulted from the radially inward electric fields; and ion losses to the electrodes, each of which acted as a sink and drew ions out of the plasma. A simple model of particle confinement was proposed, in which the particle confinement time is proportional to the plasma volume. The scaling predicted by this model was consistent with experimental measurements.

## INTRODUCTION

### Prior Investigations by Others

Pure magnetic confinement, in which a plasma is confined solely by strong magnetic fields, has been the dominant approach to plasma confinement since the beginning of controlled-fusion research. The principle of enhancing magnetic confinement by imposing strong, direct-current electric fields perpendicular to the confining magnetic field was demonstrated in an open-ended magnetic geometry by George in 1961 (ref. 1). Several investigators have since applied strong electric fields to plasmas in cusp (refs. 2 to 4) or mirror (refs. 5 and 6) configurations in an effort to enhance the otherwise poor confinement properties of these open-ended geometries. In other recent experiments (refs. 7 and 8) strong radial electric fields have been applied to plasmas in mirror geometries for the primary purpose of heating ions to high energies.

Externally applied electric fields have not thus far played a role in toroidal plasma confinement. It was suggested in 1967 (ref. 9) that a toroidal plasma could be heated and confined in a modified Penning discharge configuration. Theoretical papers by Kovrizhnykh (refs. 10 and 11) present the implications of ambipolar electric fields for diffusional transport of toroidal plasmas. Stix (refs. 12 and 13) examined theoretically how a radial electric field arising from preferential loss on divertors or limiters of large gyroradius ions would affect the confinement and stability of a toroidal plasma. The ambipolar electric fields considered by Kovrizhnykh and Stix were relatively weak and resulted in an $E/B$ drift velocity much less than the particle thermal velocity. Moreover, these ambipolar electric fields were not directly imposed by external power supplies. They therefore could neither do work on the plasma to heat it nor assist in its confinement by dynamic stabilization.

When the imposed radial electric fields reach values characteristic of the NASA Lewis bumpy-torus experiment, the $E/B$ drift velocities are comparable to the particle thermal velocities. Indeed, ions and electrons receive their energy from external power supplies through the imposed radial electric field. Under these conditions, the radial transport of particles is no longer diffusional in character. At least three mechanisms can result in ion transport along the electric field in a plasma subjected to crossed electric and magnetic fields. One such mechanism is fluctuation-induced transport due to fluctuating electric fields that point along the $\overline{E} \times \overline{B}$ direction. When binary collisions occur, a second transport mechanism along the electric field is the Pedersen current, which has been discussed by Alfven and Falthammar (ref. 14). When sufficiently strong and inhomogeneous radial electric fields exist in the collisionless regime, particles are transported along the electric field of a crossed-field geometry by the $\nabla E$ mechanism discussed by Cole (ref. 15).

The bumpy-torus configuration receives its name from the shape assumed by the confined plasma and consists of a number of coils (12 for the Lewis facility) arranged in a toroidal array. This magnetic geometry, in the form used in the Lewis facility, was proposed by Gibson, Jordan, and Lauer (ref. 16), who later extensively investigated single-particle motion relevant to it (ref. 17). Geller (ref. 18) operated a pulsed plasma source in a bumpy-torus geometry and reported near-classical confinement of the afterglow plasma (ref. 19). Fanchenko, et al. (ref. 20) have investigated turbulent heating in a bumpy-torus plasma; and Dandl, et al. (ref. 21) have carried out extensive experimental investigations on electron cyclotron resonance heating in the Oak Ridge ELMO bumpy-torus device. The approach taken in the NASA Lewis bumpy-torus project differs from that adopted in the ELMO experiment. The ELMO creates a stable magnetic well in each sector of the torus with high-beta, hot electrons that are generated by absorption of radiofrequency (rf) power; the ion population is heated by binary collisions with the more energetic electrons. In the electric field bumpy-torus approach at Lewis, the entire toroidal plasma is raised to high potentials by electrodes that are connected to external power supplies. The resulting radial electric fields profoundly influence confinement, as well as raise the ion population to high energies by E/B drift. The resulting thermalized ion temperatures are substantially higher than that of the electron population.

## Previous Investigations of the NASA Lewis Bumpy-Torus Plasma

The NASA Lewis bumpy-torus project was preceded by an investigation of the modified Penning discharge in a simple magnetic mirror configuration. During these investigations, the presence of kilovolt Maxwellian ions, isotropic in velocity space, was established (refs. 22 to 24). The plasma in the modified Penning discharge was found to be highly turbulent (ref. 25), and this turbulence evidently plays a role in the thermalization of the ion energies that result from E/B drift in the crossed electric and magnetic fields (ref. 22).

In the NASA experiment, the toroidal plasma was biased to high potentials by applying positive or negative direct-current voltage to 12 or fewer electrodes located in the midplanes of sectors of the toroidal array. An electric field distribution consistent with the investigations described in references 26 and 27 is shown schematically in figure 1 for negative electrode polarity. The toroidal plasma was biased to 80 or 90 percent of the potentials on the midplane electrodes. The electric field was strongest in the annular region between the grounded inner bores of the superconducting magnets and the plasma. The radial electric field has exceeded 1 kilovolt per centimeter at the plasma boundary and has penetrated inward to at least one-half of the plasma radius (ref. 27).

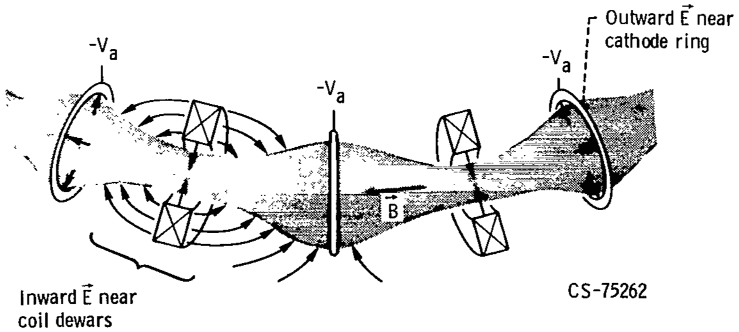

Figure 1. - Electric field structure in a bumpy-torus plasma with negative midplane electrodes.

Previous investigations of the bumpy-torus plasma, at relatively low densities and confinement times (refs. 26 and 27), have shown that - in common with Penning discharges and magnetron devices - the plasma formed rotating spokes that gyrated around its minor circumference at nearly the E/B drift velocity. As for the simple, modified Penning discharge (refs. 22 to 25), the ions in the rotating spokes formed an energy reservoir that was thermalized to the high kinetic temperatures observed. Ion kinetic temperatures up to 2.5 keV have been measured in deuterium. The thermal velocity of these hot ions was proportional to the spoke rotational velocity (ref. 27).

Previous work (ref. 27) has shown that the ion population can be heated equally well by positive or negative electrode polarities. However, investigations reported in references 28 and 29 indicate that the polarity of the electric field has a profound effect on the density and particle confinement time. Both were substantially greater when the electric field pointed radially into the plasma than they were when the electric field pointed outward and pushed ions out of the plasma.

As an aid in understanding this large difference in confinement, the fluctuation-induced particle transport rates were measured with a new technique, the key ideas of which are described in references 30 and 31. Experimental measurements of the transport resulting from fluctuating electric fields have shown that the plasma characteristically rotated with the E/B drift velocity at all frequency bands below a few hundred kilohertz (ref. 32). The ions were transported in the direction of the Pedersen currents, that is, radially inward when the electric field pointed inward and radially outward when the electric field pointed outward (refs. 33 and 34). This radial transport of plasma was sometimes associated with a single peak in the fluctuation spectrum, a rotating spoke. On other occasions it was associated with a broad spectrum of background turbulence under conditions for which no prominent peaks existed (refs. 33 and 34). The investigations reported in reference 34 made it clear that - by applying strong, radial electric fields - ions could be infused radially inward against a density gradient when the electric field pointed radially inward.

## Scope of Paper

This paper concentrates on those aspects of confinement and transport that are affected by the application of strong radial electric fields to a confined toroidal plasma. The first experimental section describes the characteristics of the plasma fluctuations under various conditions of turbulent or coherent wave propagation in the plasma. The fluctuation spectra, their amplitude statistics, their spectral index, and the implications for ion heating and thermalization are discussed. The second experimental section presents radial profiles of various plasma characteristics, including the relative number density, the floating potential, and the ion transport rate. The third section reports how the plasma characteristics depend on various independent parameters and yields scaling information that is useful in formulating physical models for the observed phenomena. The fourth section reports the functional dependence of radial transport on electrode polarity, electrode current, and a weak, vertical magnetic field applied to the confinement volume. The final experimental section outlines the "sink" model of confinement, a scaling relationship for the particle confinement time that is consistent with experimental measurements. Finally, the experimental data are discussed and used to narrow the range of physical models that can be used to describe the observed transport phenomena.

## EXPERIMENTAL APPARATUS

### Magnet Facility

An isometric cutaway drawing of the superconducting bumpy-torus magnet facility is shown in figure 2. This facility consists of 12 superconducting coils equally spaced

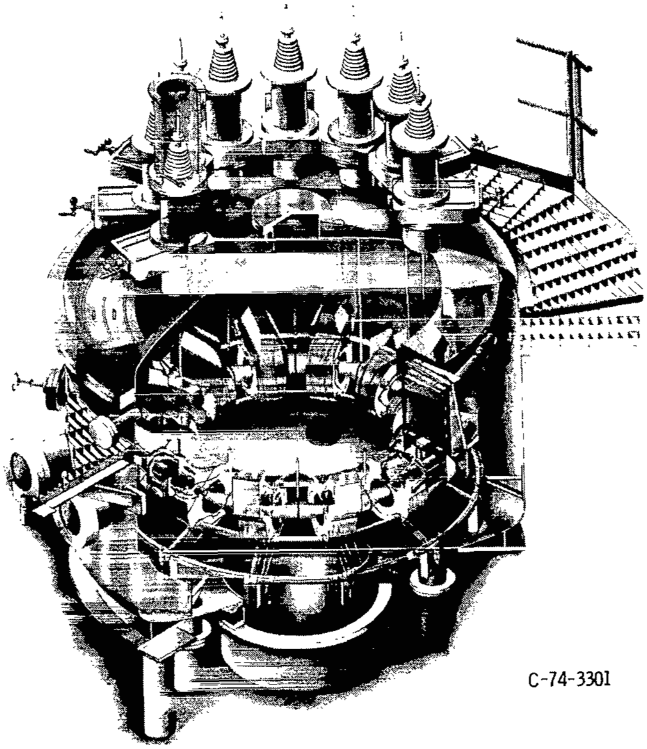

Figure 2. - Isometic cutaway drawing of the superconducting-magnet bumpy-torus facility.

around a toroidal volume 1.52 meters in major diameter. Each coil has an inner diameter of 19 centimeters, and the maximum magnetic field on the magnetic axis during the experiments reported in this paper was 2.4 teslas. The minimum magnetic field on the magnetic axis between coils is 40 percent of the maximum magnetic field. The coil array is contained in a single vacuum tank 2.6 meters in major diameter. The characteristics and performance of this superconducting magnet facility have been reported elsewhere (refs. 35 and 36).

## Biasing Electrodes

Various electrode shapes were tested for their ability to affect the plasma density and particle confinement time. Some of the electrode configurations examined are shown

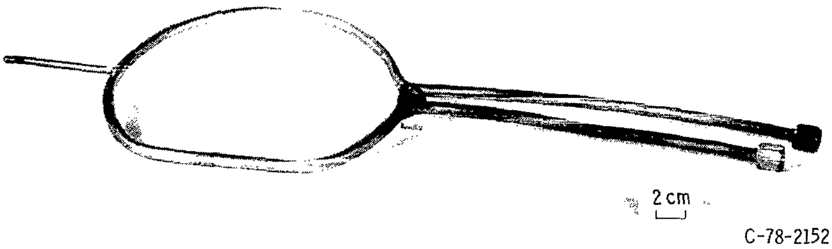

Figure 3. - Standard D-shaped electrode ring fabricated of 9.5-millimeter-diameter, water-cooled copper tubing.

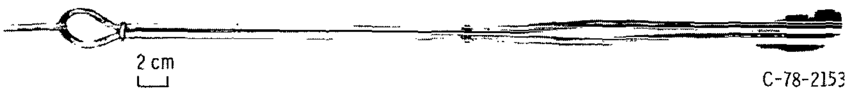

Figure 4. - Dual electrode fabricated from 6.4-millimeter-diameter, water-cooled, stainless-steel tubing.

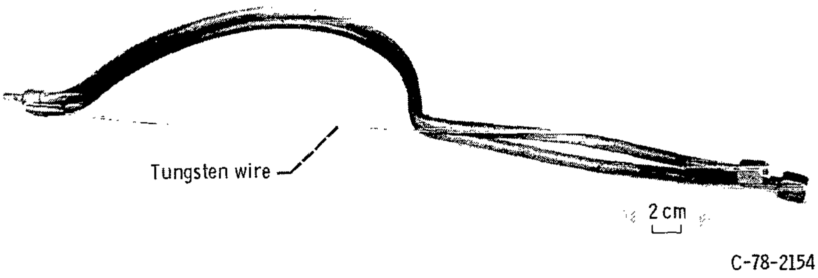

Figure 5. - Water-cooled electrode holder supporting a 1.5-millimeter-diameter, pure-tungsten wire. (Electrode holder remains outside plasma volume.)

in figures 3 to 5. How changing the number of identical electrodes used to bias the plasma affects the plasma characteristics has been reported in previous work (refs. 27, 28, and 37). In most of the investigations reported herein, only one or two identical electrodes were used to bias the plasma.

Three configurations produced high number densities and particle confinement times. One of these was the standard D-shaped electrode shown in figure 3. This electrode was inserted with the flat side of the D facing radially inward toward the major vertical axis of the torus. The electrode was made of 9.5-millimeter-diameter, water-cooled copper tubing. The pin on the lower end of the electrode was seated into a funnel-shaped aluminum retaining cup, which allowed the electrode to be repositioned reliably in the same location. All the electrodes discussed in this report could be moved 12 centimeters along the major toroidal radius in the midplane of the sector in which they were located. The standard D-shaped electrode (fig. 3) surrounded the minor circumference of the plasma and biased it through a sheath about 4 to 10 millimeters thick. Under characteristic operating conditions, the D-shaped electrode was located where the radial plasma density was no more than 20 percent of that on the plasma axis.

Another electrode that produced superior number densities and particle confinement times was the stainless-steel tube electrode shown in figure 4. This electrode - which consisted of dual 6.4-millimeter-diameter, stainless-steel, water-cooled tubes - passed across a minor diameter of the plasma. The center of the electrode passed through the region of maximum, axial plasma-number density but was shielded from direct interaction with the plasma by a dark, 4- to 8-millimeter-thick sheath, which could be observed visually. This sheath was visible in directions both parallel and perpendicular to the local magnetic field lines. This dual, stainless-steel tube electrode was also positioned by the pin at its lower end and could be moved along the major toroidal radius.

The third electrode, the performance of which is discussed later, was an uncooled, 1.5-millimeter-diameter, pure-tungsten wire that passed across the minor diameter of the plasma (fig. 5). This electrode has produced some of the highest number densities and particle confinement times, but at a severe trade-off in ion energy. Ion bombardment of this electrode associated with the collected current caused it to glow with a yellow heat, which was inadequate to emit thermionic electrons. This tungsten wire, when inserted in the plasma, was surrounded by a dark, 4- to 8-millimeter-thick sheath both parallel and perpendicular to the magnetic field.

## Microwave Interferometer

The average plasma number density was measured by a microwave interferometer that could be operated in either a polarization diplexing or a standard Michelson interfer-

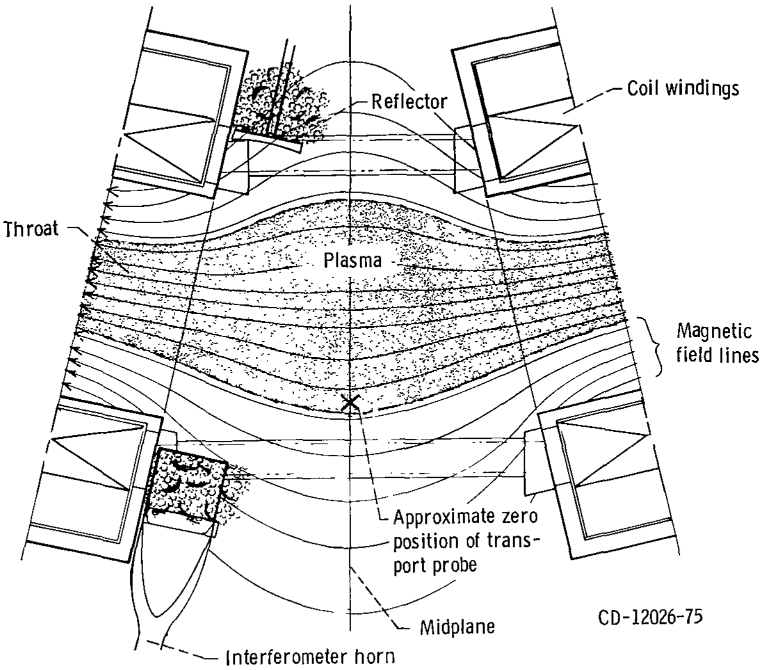

Figure 6. - Plan view of one sector of bumpy-torus plasma, showing position of microwave interferometer and standard (R = 0) probe position at which radial transport measurements were made.

ometer mode. The characteristics and performance of this interferometer have been described in references 28 and 38. In this series of investigations, the plasma number density was sufficiently high that the interferometer was operated in the standard Michelson mode. The location of the interferometer is shown on the plan view of figure 6. The interferometer horn was located on the outside major radius of the plasma, with a stationary reflector on the inside major radius. The axis of this interferometer was approximately halfway between the midplane and throat of the plasma sector in which it was located. The thickness of the plasma on the interferometer axis, approximately 13 centimeters, was used to reduce the observed phase shift to a spatially averaged electron number density across the plasma diameter.

## Diagnostic System for Particle Transport

The radial flux of ions in this plasma was measured with a transport diagnostic that was based the physical model discussed in reference 30. This model assumed such low-frequency ($\omega << \omega_{ci}$) electrostatic potential fluctuations that a particle's fluctuating velocity could be modeled in terms of $\tilde{E}/B$ drift, where $\tilde{E}$ is a fluctuating electric field and

B is the static, confining toroidal magnetic field. The time-averaged particle flux was then given by

$$\Gamma = \langle \tilde{n}\tilde{v} \rangle = \frac{\langle \tilde{n}\tilde{E} \rangle}{B} \tag{1}$$

which can also be expressed in terms of a transport spectral density function $T(\omega)$ as

$$\Gamma = \langle \tilde{n}\tilde{v} \rangle = \int_0^\infty T(\omega)d\omega \tag{2}$$

Reference 30 shows that the transport due to a small band of frequencies $\delta\omega$ centered at $\omega$ is given by $T(\omega)$ and is equal to

$$T(\omega)\delta\omega = \frac{k(\omega)}{B} n_{rms}(\omega)\varphi_{rms}(\omega) \sin \alpha_{n\varphi}(\omega) \left|\gamma_{n\varphi}(\omega)\right| \tag{3}$$

To relate the potential $\tilde{\varphi}$ and electric field $\tilde{E}$ fluctuations, we assumed an electrostatic approximation $\tilde{E} = -\nabla\tilde{\varphi} = ik(\omega)\tilde{\varphi}$. The transport associated with $T(\omega)$ depends on the product of the rms values of density $n_{rms}$ and potential $\varphi_{rms}$ fluctuations, the sine of the phase angle $\alpha_{n\varphi}(\omega)$ between the density and potential fluctuations, and the degree of mutual coherence $\left|\gamma_{n\varphi}(\omega)\right|$ between the potential and density fluctuations in the spectral band under consideration. The wave number $k(\omega)$ appears since the electrostatic approximation was assumed. The transport spectrum $T(\omega)$ is a real quantity and may be either positive or negative, depending on whether the transport is inward or outward.

To implement this transport diagnostic, it was necessary to develop a data acquisition system that could simultaneously acquire and digitize density and potential flucuation data and transfer the raw time-series data to a computer for processing. Expressing all spectra of interest (particularly the transport spectra) in absolute physical units, as was our objective, required knowledge of the system calibration data (e.g., voltage range settings on the digitizer, preamplifier gain settings, etc.). The system used to acquire and process the data discussed in this paper is described in reference 39.

A block diagram of the data acquisition system is shown in figure 7. The Langmuir and capacitive probes were used to measure $\tilde{n}$ and $\tilde{\varphi}$, respectively. Limitations had to be placed on the number density and energy density of the plasma in order to avoid damage to the probes. The Langmuir and capacitive probes were essentially identical to those discussed in reference 40. The Langmuir probe was maintained in ion saturation so that the saturation current and the voltage appearing across a resistor to ground were both proportional to the ion number density. The ion transport rate therefore resulted from the data-processing procedure.

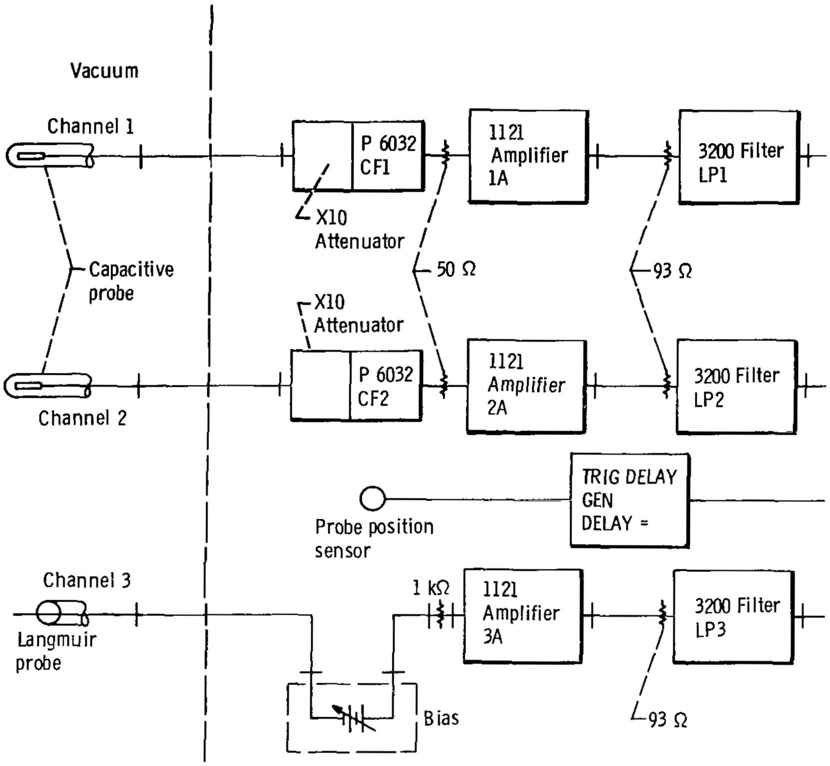

Figure 7. - Block diagram of data-

The fluctuating phenomena in the plasma were monitored with the probe array shown in figure 8. The probes were mounted on a fixture that was hydraulically actuated into the plasma for approximately 0.3 second. The travel of the probes was adjusted so that both capacitive probe 1 (channel 1) and the Langmuir probe were positioned about 7 centimeters from the plasma axis in the equatorial plane of the torus when data were being taken. Capacitive probe 1 and the Langmuir probe were displaced axially 1 centimeter from each other. With this arrangement the density and potential fluctuations could be measured at the same minor radius in the plasma for fluctuations with an axial wavelength much longer than 1 centimeter. Capacitive probe 2 (channel 2) was located $30^{o}$ above the equatorial plane in the same vertical plane and at the same minor plasma radius as the Langmuir probe. The entire array was inserted into the midplane of a toroidal sector that did not contain an electrode.

The location of the probe array when inserted into the plasma is shown in figure 6, although it should be kept in mind that the sector in which the probes were located was actually at the opposite major diameter from the sector containing the microwave interferometer. In some series of measurements, a radial profile of ion transport was taken, in which the probe assembly was moved 4 centimeters inward or outward from the arbitrary zero position indicated in figure 6.

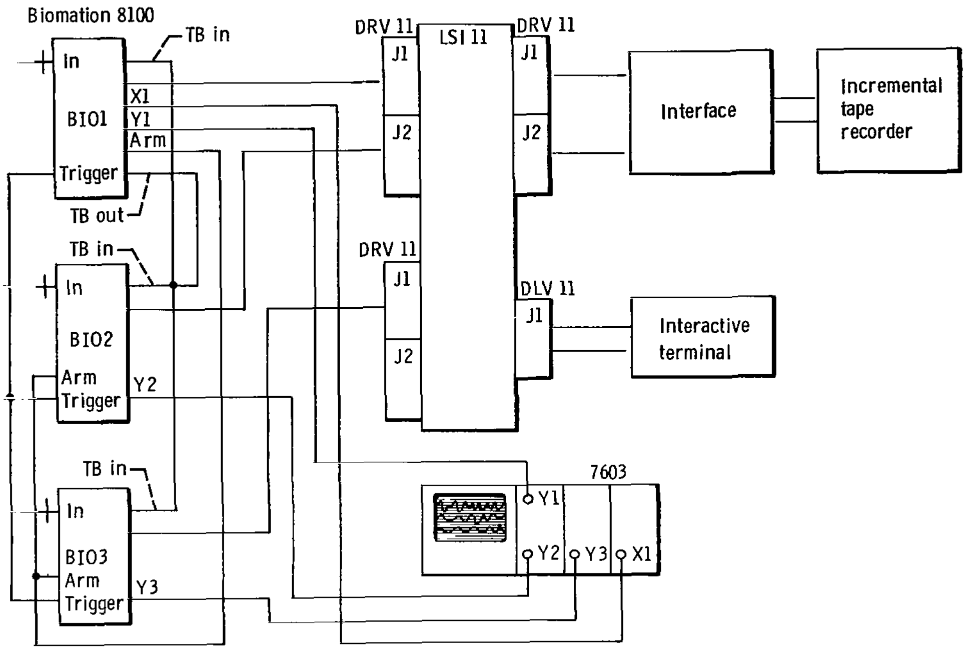

andling system for radial transport measurements.

As shown in figure 7, transient recorders were used to digitize both density and potential fluctuation data. All the spectra included in this paper were computed from a digitized version of $\tilde{n}$ or $\tilde{\varphi}$ consisting of 2048 eight-bit words. The data were stored on magnetic tape for processing by a high-speed computer program that employs a fast Fourier transform algorithm (ref. 39). The procedure used to calibrate the data-handling system is described in reference 39. For all data reported herein, the frequency response, simultaneity, and bandwidth were such that the results were not affected (ref. 39).

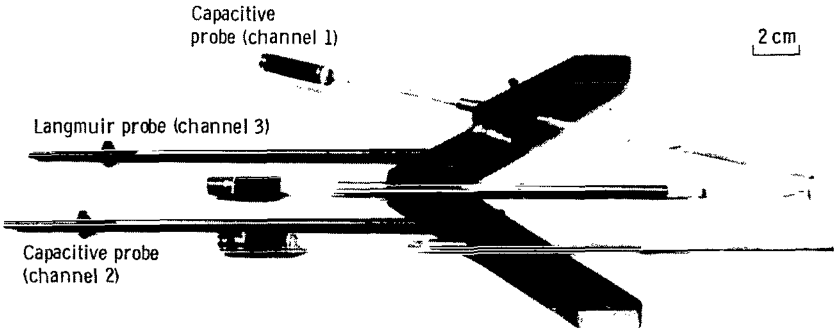

Figure 8. - Probe array used to measure radial transport rate.

## Estimates of Error

The theoretical understanding of physical processes in this plasma is not sufficiently advanced to allow experimental errors to be estimated by reference to theoretical models or analytical expressions, and the time and resources available during the experimental program were usually not adequate to take repeated experimental runs and thereby establish the limits of error. In spite of these restrictions, it was sometimes possible to repeat data under conditions that were similar but not identical to those selected for presentation in this report, and it was sometimes possible to establish a degree of jitter or fluctuation about a smoothly varying functional dependence of the quantity being investigated. Rough estimates of the experimental error were based on these consideration and, where possible, are shown on the appropriate experimental plot in the form of estimated-error bars.

TABLE I. - OPERATING CONDITIONS FOR EXPERIMENTAL RUNS

ILLUSTRATING PLASMA FLUCTUATIONS

| Operating condition | Experimental run | | | |
|---|---|---|---|---|
| | AHN-18A | AHN-9A | AJH-2 | AIN-2A |
| Number of electrodes | 2 | 2 | 1 | 2 |
| Type of electrode used | D | D | Stainless-steel rod | D |
| Location of electrodes, sector | 5,6 | 5,6 | 6 | 6,7 |
| Electrode polarity | Positive | Negative | Negative | Negative |
| Character of data | Turbulent | Quasi-turbulent | Turbulent | Coherent |
| Electrode voltage, $V_a$, kV | 0.45 | -1.5 | -2.5 | -2.5 |
| Electrode current, $I_a$, A | 0.29 | 0.50 | 2.0 | 0.92 |
| Plasma electron number density, $\bar{n}_e$, $cm^{-3}$ | $0.09\times10^{11}$ | $7.2\times10^{11}$ | $5.4\times10^{11}$ | $1.10\times10^{11}$ |
| Background pressure, $p_0$, particles/$cm^3$ (torr) | $1.8\times10^{12}$ ($5.3\times10^{-5}$) | | $2.6\times10^{12}$ ($7.6\times10^{-5}$) | |
| Electric field direction | Outward | Inward | Inward | Inward |

## CHARACTERISTICS OF PLASMA FLUCTUATIONS

Examples of fluctuation-related spectra that were obtained during a study of fluctuation-induced transport on the NASA Lewis bumpy-torus plasma are presented in this section. The four experimental runs selected for presentation are characteristic of highly turbulent, quasi-turbulent, and highly coherent fluctuating phenomena in the plasma. The characteristics of these four runs are shown in table I.

### Data Sampling

It was not possible to leave the probe assembly in the plasma continuously because damage from plasma bombardment would have resulted. During these investigations, the probe assembly was inserted in the plasma for approximately 0.3 second. The time history of floating potential from the Langmuir probe, operated into a high-impedance voltmeter, is shown in figure 9. The probe was actuated into the plasma at $t = 0$. After approximately 0.1 second, the initial transients due to mechanical overshoot and/or clean-

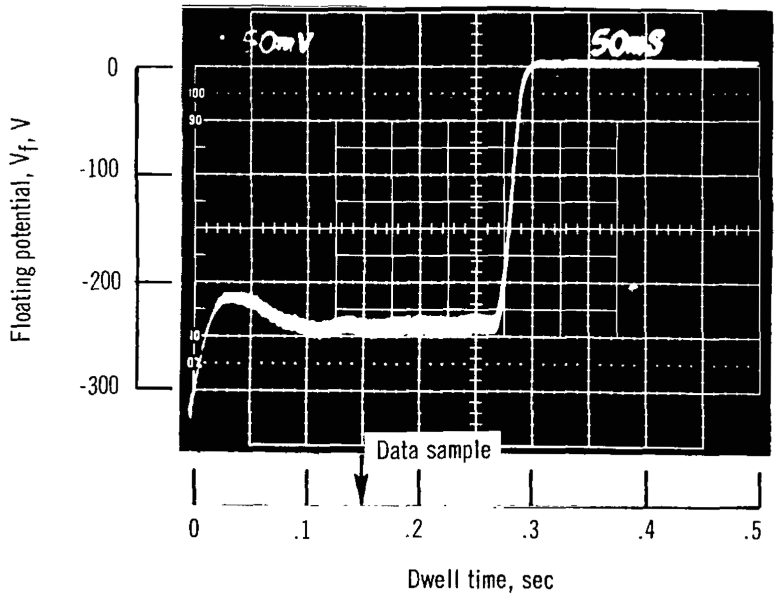

Figure 9. - Potential on floating Langmuir probe as function of dwell time, for single insertion of probe assembly into plasma. Electrode polarity, negative; electrode voltage, $V_a$, -2.5 kV; electrode current, $I_a$, 0.96 A; average electron number density, $\bar{n}_e$, $8.3\times10^{10}$ cm$^{-3}$; background neutral gas density, $p_0$, $1.58\times10^{12}$ particles/cm$^3$ ($4.6\times10^{-5}$ torr).

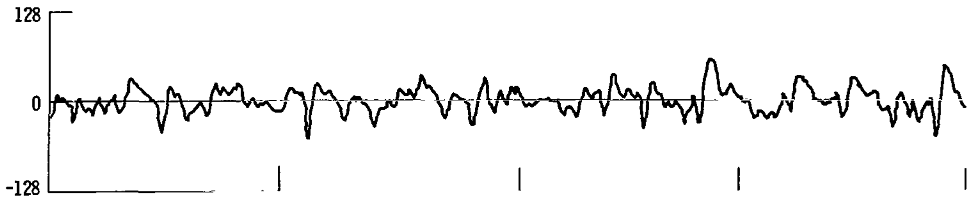

(a-1) Channel 1.

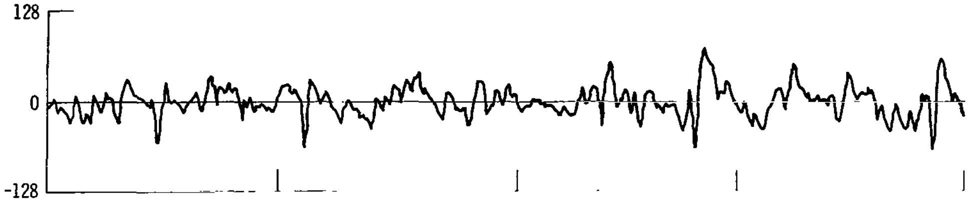

(a-2) Channel 2.

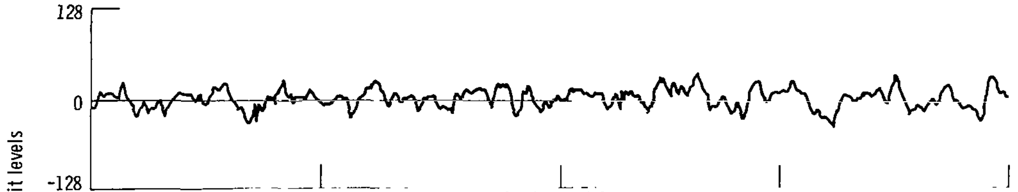

(a-3) Channel 3.

(a) Run AHN-18A (table I).

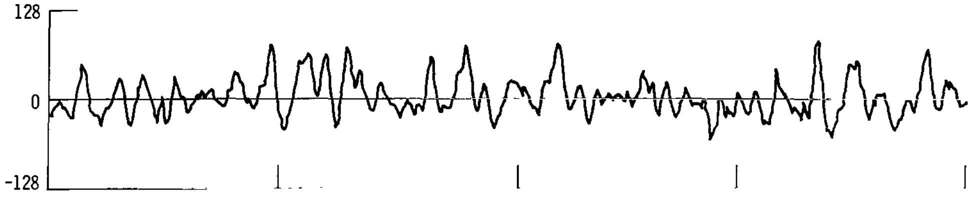

(b-1) Channel 1.

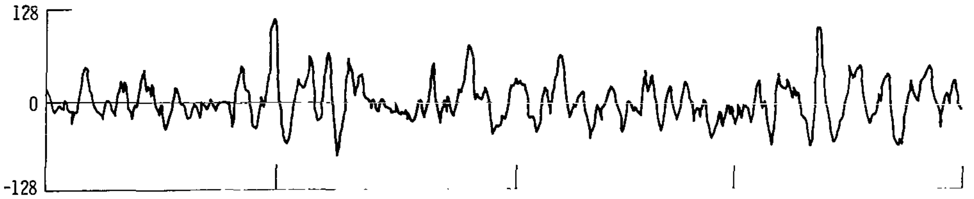

(b-2) Channel 2.

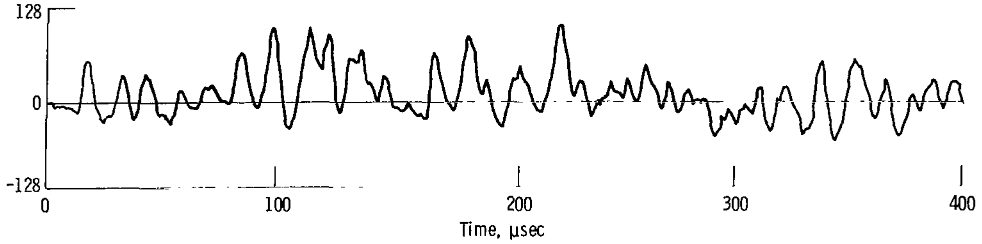

(b-3) Channel 3.

(b) Run AHN-9A (table I).

Figure 10. - Simultaneously sampled waveforms of floating potential on capacitive probes (channels 1 and 2) and of density fluctuations measured with biased Langmuir probe (channel 3).

ing of the probe tip had died out, leaving the plasma in a quasi-steady state for the following 0.17 second. The floating potential in this instance was approximately -240 volts. The spectra were computed from a time series consisting of 2048 eight-bit samples taken every 1 microsecond. Thus, the duration of each record was 2.048 milliseconds and the Nyquist frequency was 500 kilohertz. This approximately 2-millisecond data window was taken at the 150-millisecond point shown on the abscissa of figure 9. The spectral plots were frequency averaged over nine elementary frequency bands, for a spectral bandwidth (the frequency separation of the discrete points plotted in the fluctuation spectra) of 4.39 kilohertz (9/2.048 msec). A cosine-bell data window was applied to the raw time-series data in order to minimize the effects of leakage.

## Fluctuation Waveforms

Figure 10 illustrates the nature of the raw time-series data from which the fluctuation spectra were computed. Figures 10(a) and (b) correspond, respectively, to the first two experimental runs in table I. In these two figures, channels 1 and 2 are the simultaneously sampled potential waveforms from the capacitive probes. Channel 3 is the simultaneously sampled ion saturation current flowing to the biased Langmuir probe. The eight-bit amplitude capability of the waveform recorders has been divided into 256 intervals. The absolute amplitudes corresponding to these intervals are determined by the settings of the waveform recorder and other instruments in the data-handling system (ref. 39). The abscissa shows the data points from the first 400 of the 2048 data samples. These waveforms therefore cover the approximately 20 percent of the data in each channel that were used to compute the fluctuation spectra discussed here.

The data in figure 10(a) were taken for positive polarity conditions that resulted in a highly turbulent plasma without discrete peaks in the spectra. Careful examination of the signals in channels 1 and 2 shows that the signal in channel 1 was slightly delayed with respect to the signal in channel 2. The data in figure 10(b) were taken for negative polarity conditions, when the electric field pointed radially inward, which resulted in a quasi-turbulent plasma (i.e., discrete peaks are visible in the fluctuation spectra, but their amplitude scarcely rises above the background turbulent spectrum). In figure 10(b) the signal in channel 2 was slightly delayed with respect to the signal in channel 1 because the direction of wave propagation, associated with reversal of the direct-current, radial electric field in the plasma, was reversed. The density waveform in channel 3 was also slightly delayed with respect to the potential waveform in channel 1.

The pair of simultaneously sampled density and potential waveforms in figure 10 are characteristic of those used as input for the data analysis program that produced the fluctuation spectra. Waveforms similar to those in figure 10 were displayed on an oscilloscope before the data were committed to magnetic tape for later analysis. Data that showed defects caused by arcing, changes in the plasma during the run, or voltage transients were rejected and the experimental run was repeated.

## Fluctuation Spectra

The physics information that can be obtained from the fluctuation-induced plasma transport diagnostic is illustrated by the four experimental runs in table I and the related spectral plots in figures 11 to 14. Each figure consists of eight computer-generated spectra. The spectra in parts (a) to (d) and (f) correspond to the five spectral quantities on the right side of equation (3).

Spectrum (a) is the autopower spectrum of $\tilde{\varphi}_1(t)$. All system calibration factors have been taken into account, so that the ordinate of each data point corresponds to the mean squared value (i.e., $\varphi^2_{rms}(\omega)$) of the potential fluctuations over a 4.39-kilohertz spectral bandwidth. Spectrum (b) is the autopower spectrum of the density fluctuations, with each point denoting the mean squared value (i.e., $n^2_{rms}(\omega)$) of the density fluctuations over a 4.39-kilohertz spectral bandwidth.

Spectra (c) and (d) are both phase spectra. Spectrum (c) corresponds to the phase $\theta_{12}(\omega)$ of the cross-power spectrum computed from $\tilde{\varphi}_1(t)$ and $\tilde{\varphi}_2(t)$. From the phase spectrum $\theta_{12}(\omega)$ the wave number $k_\theta(\omega)$ can be readily determined by using the approach described in references 31 and 41. From $k_\theta(\omega)$ the azimuthal phase velocity $\omega/k_\theta(\omega)$ can be computed. Generally, the phase velocities associated with the $\theta_{12}(\omega)$ plots in figures 11 to 14 were about $10^6$ centimeters per second. This is within a factor of 2 of the $E_r/B$ drift, where $E_r$ - the static, radial electric field resulting from direct-current voltage applied to the electrodes - was about 100 volts per centimeter and B - the toroidal magnetic field at the point at which the measurements were being made - was 0.67 tesla.

Spectrum (d), the phase of the cross-power spectrum computed from $\tilde{\varphi}_1(t)$ and $\tilde{n}(t)$, represents the phase difference $\alpha_{n\varphi}(\omega)$ between the density and potential fluctuations on a spectral basis. Spectrum (e), the squared coherency spectrum between channels 1 and 2, measures the relative degree of coherence between the electrostatic potential fluctuations sampled by the two capacitive probes. Spectrum (f), the square of the degree of mutual coherence $|\gamma_{n\varphi}(\omega)|^2$ between channels 1 and 3, enters into equation (3) because we are considering polychromatic fluctuations rather than the special case of monochromatic fluctuations where $|\gamma_{n\varphi}| = 1$. Further properties of coherency spectra are discussed in reference 42.

Spectrum (g) is the transport spectrum $T(\omega)$. Since $T(\omega)$ was computed from digitized data, we actually plotted a transport spectrum (number of particles/area·time) not a transport spectral density function (number of particles/area· time· frequency). Thus the ordinate of each point in the transport spectrum denotes the fluctuation-induced transport associated with a 4.39-kilohertz spectral band centered at the frequency in question. The transport spectrum $T(\omega)$ is a real quantity and may be either positive or negative, indicating that the transport is in either the inward or outward direction, respectively. Equation (3) reveals that only two quantities determine the sign of $T(\omega)$ and hence the direction of transport. The first quantity is the phase difference $\alpha_{n\varphi}(\omega)$ between density and potential fluctuations. If $\alpha_{n\varphi}(\omega)$ changes sign, $T(\omega)$ changes sign since $T(\omega)$ is proportional to $\sin \alpha_{n\varphi}(\omega)$. The second quantity determining the sign of $T(\omega)$ is the sign of $k_\theta(\omega)$, which in turn is determined by the direction of wave propagation (in the azimuthal direction).

Spectrum (h), the cumulative transport spectrum, was found by summing the transport spectrum $T(\omega)$ from zero frequency to the frequency on the abscissa. The cumulative transport at 500 kilohertz is the total fluctuation-induced transport associated with the fluctuation spectrum extending from 0 to 500 kilohertz.

Figure 11 shows the fluctuation spectra for run AHN-18A (table I), which had positive electrode polarity. This run was characterized by a high degree of turbulence. The phase spectrum of figure 11(c) shows that the dispersion relation was linear and that the fluctuating disturbances rotated with a common drift velocity to frequencies of at least 150 kilohertz. This phase velocity also had a positive slope for the positive polarity, indicating drift in the E/B direction. The cumulative transport was radially outward, in the direction of the electric field, as indicated by the negative transport spectra in figures 11(g) and (h).

Figure 12 shows the fluctuation spectra for run AHN-9A (table I), which had negative electrode polarity. Under these operating conditions, the fluctuations were quasi-turbulent. Both the potential and density fluctuations (figs. 12(a) and (b), respectively) exhibit discrete low-amplitude peaks that are also evident in the squared coherency spectra (figs. 12(e) and (f)). The phase spectrum (fig. 12(c)) shows a linear dispersion relation with a common drift velocity to 200 kilohertz in the E/B direction. This relation resulted from the negative polarity and the inward-pointing electric field. The transport spectra in figures 12(g) and (h) indicate radially inward transport that is positive in sign.

Figure 13 shows the fluctuation spectra for run AJH-2 (table I), which had negative electrode polarity. This run was characterized by turbulence. No discrete peaks are apparent in the spectra of either the potential or density fluctuations (figs. 13(a) and (b)), the coherency (figs. 13(e) and (f)) was relatively low, and the transport was spread over a broad range of frequencies to 120 kilohertz. The entire turbulent mass of plasma rotated with a common velocity in the E/B direction and with a negative slope, as is evident in the phase spectrum (fig. 13(c)). The dispersion relation was linear to 120 kilohertz.

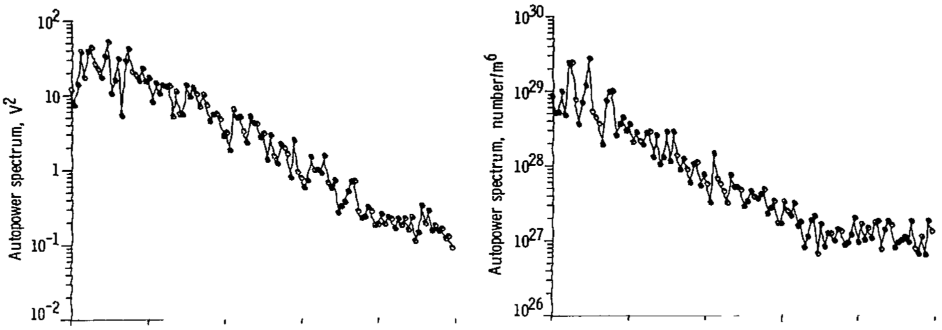

(a) Autopower spectrum of potential fluctuations in channel 1.

(b) Autopower spectrum of density fluctuations in channel 3.

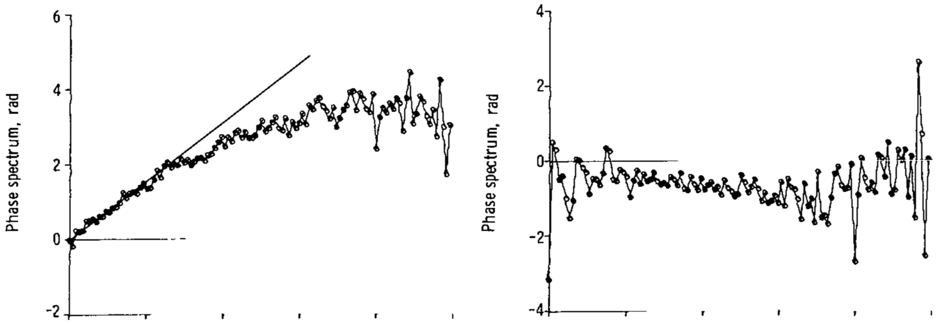

(c) Phase spectrum between channels 1 and 2.

(d) Phase spectrum between density and potential fluctuations, channels 1 and 3.

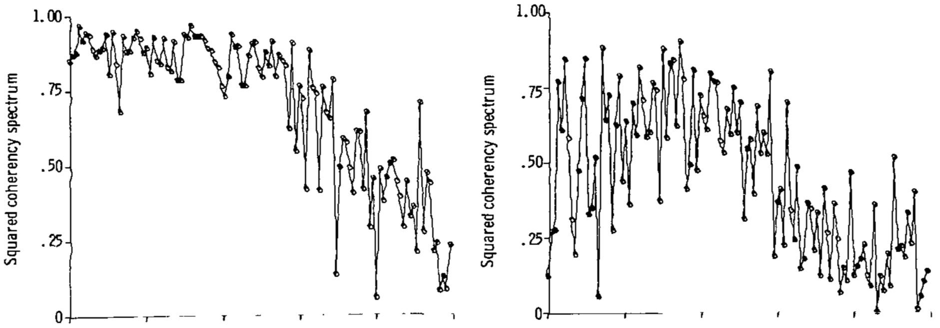

(e) Squared coherency spectrum between channels 1 and 2.

(f) Squared coherency spectrum between density and potential fluctuations, channels 1 and 3.

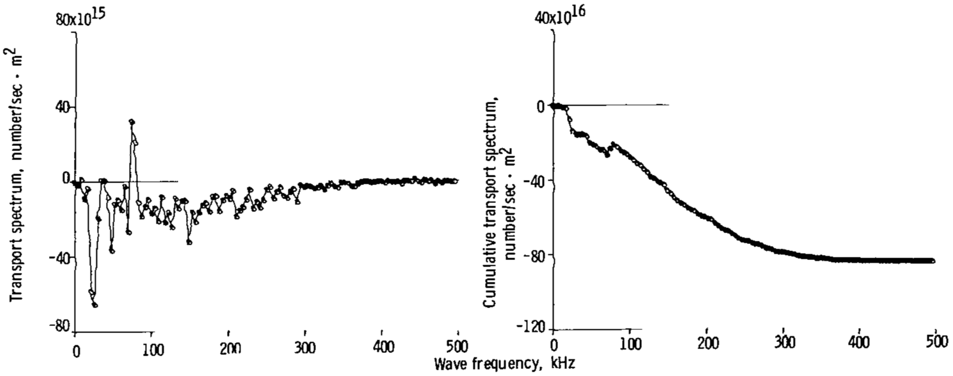

(g) Transport spectrum.

(h) Cumulative transport spectrum.

Figure 11. - Computer-generated spectra over frequency range 0 to 500 kilohertz - run AHN-18A (table I).

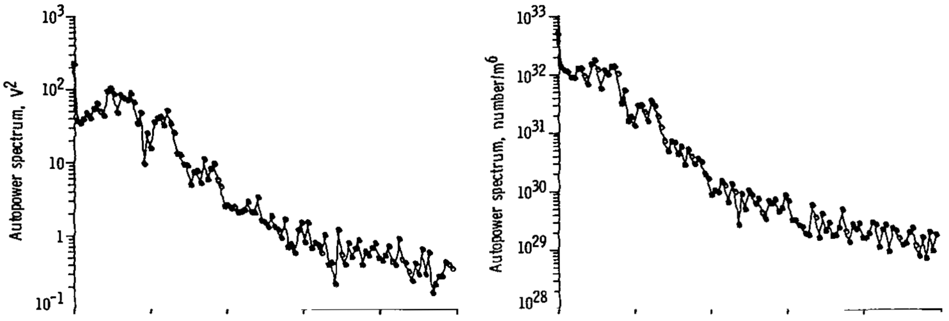

(a) Autopower spectrum of potential fluctuations in channel 1.

(b) Autopower spectrum of density fluctuations in channel 3.

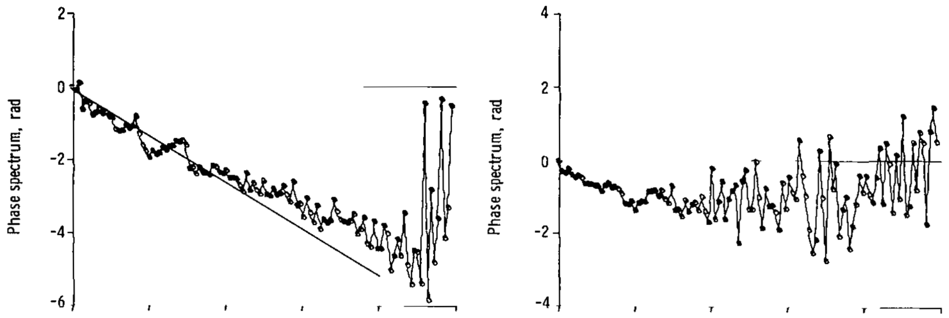

(c) Phase spectrum between channels 1 and 2.

(d) Phase spectrum between density and potential fluctuations, channels 1 and 3.

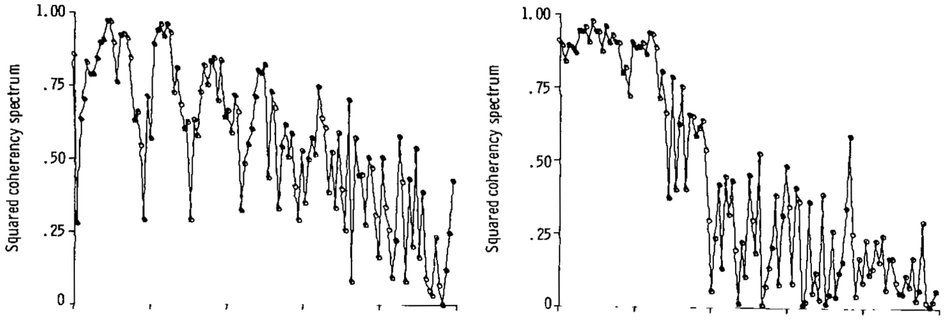

(e) Squared coherency spectrum between channels 1 and 2.

(f) Squared coherency spectrum between density and potential fluctuations, channels 1 and 3.

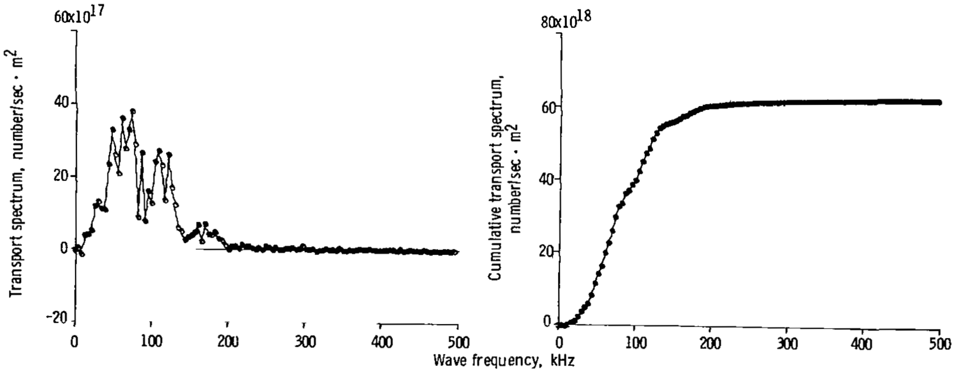

(g) Transport spectrum.

(h) Cumulative transport spectrum.

Figure 12. - Computer-generated spectra over frequency range 0 to 500 kilohertz - run AHN-9A (table I).

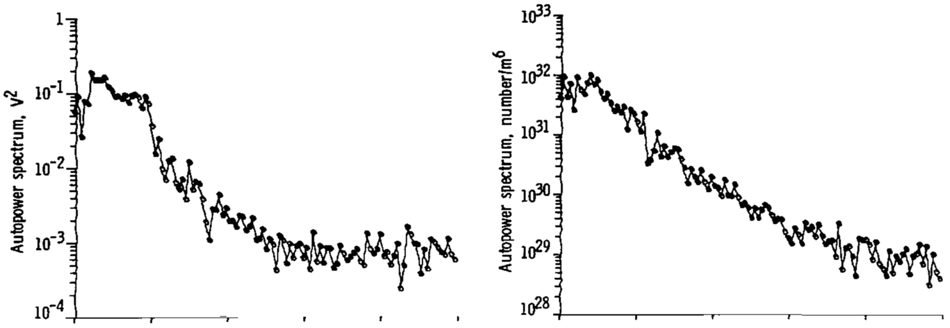

(a) Autopower spectrum of potential fluctuations in channel 1.

(b) Autopower spectrum of density fluctuations in channel 3.

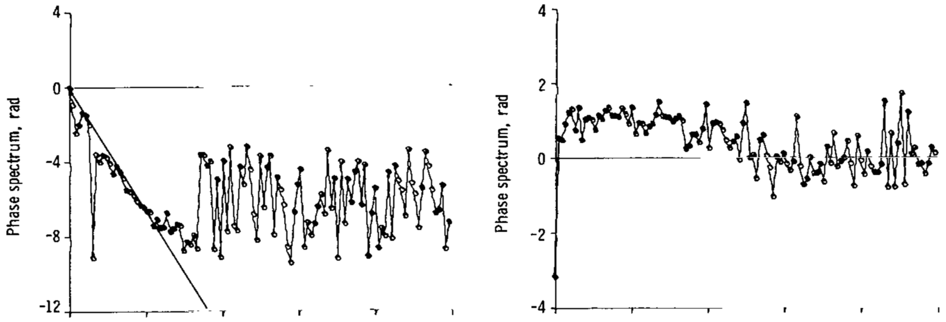

(c) Phase spectrum between channels 1 and 2.

(d) Phase spectrum between density and potential fluctuations, channels 1 and 3.

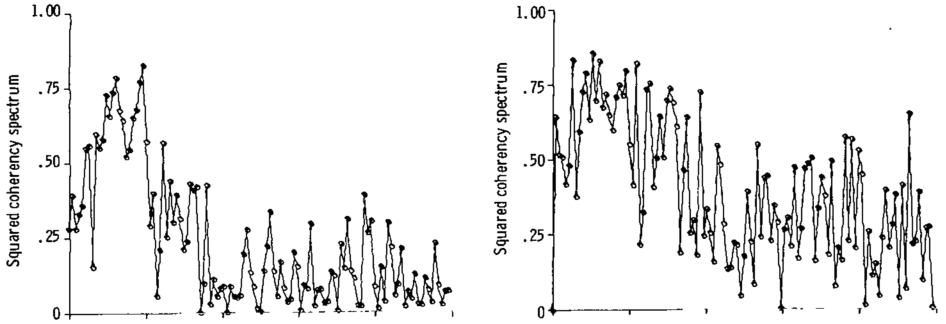

(e) Squared coherency spectrum between channels 1 and 2.

(f) Squared coherency spectrum between density and potential fluctuations.

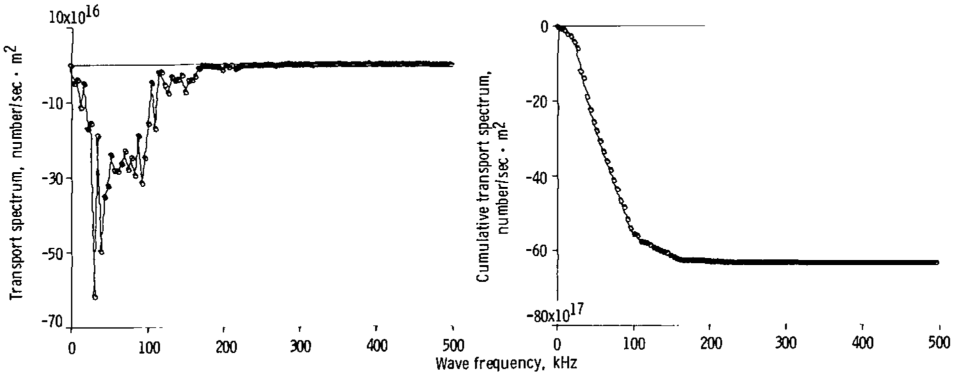

(g) Transport spectrum.

(h) Cumulative transport spectrum.

Figure 13. - Computer-generated spectra over frequency range 0 to 500 kilohertz - run AJH-2 (table I).

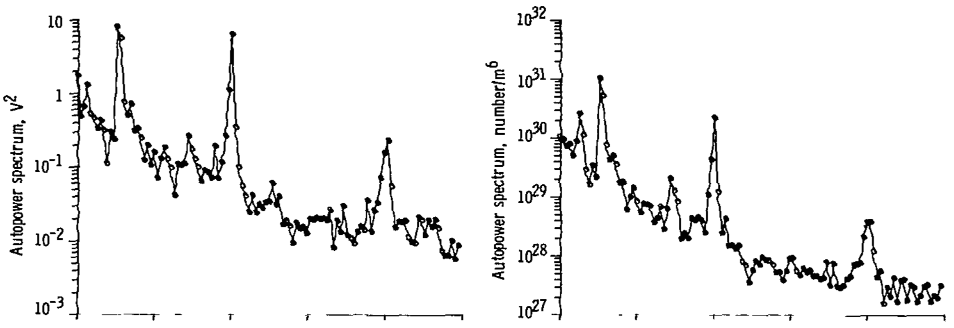

(a) Autopower spectrum of potential fluctuations in channel 1.

(b) Autopower spectrum of density fluctuations in channel 3.

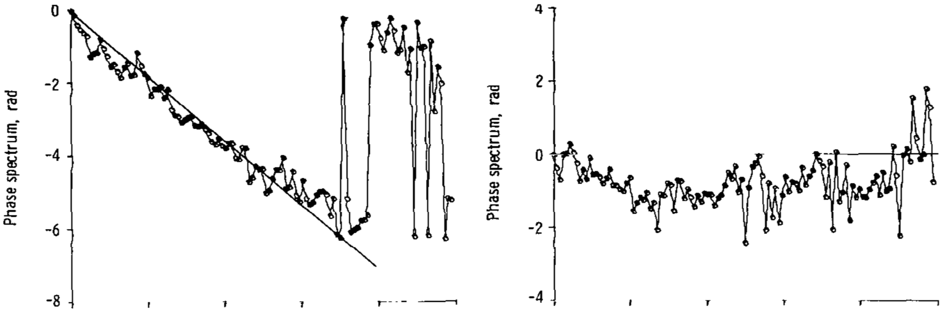

(c) Phase spectrum between channels 1 and 2.

(d) Phase spectrum between density and potential fluctuations, channels 1 and 3.

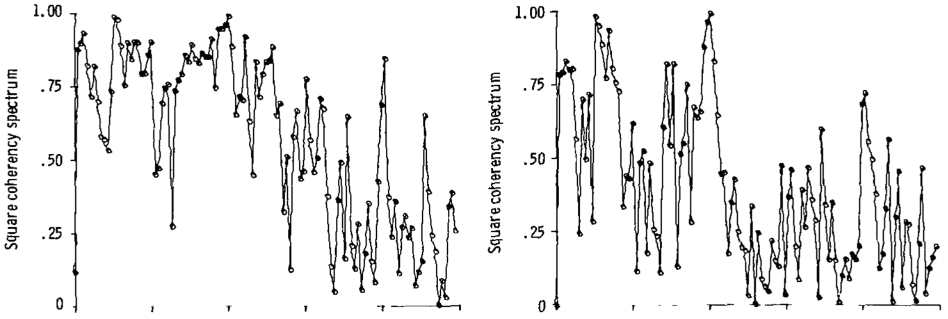

(e) Squared coherency spectrum between channels 1 and 2.

(f) Squared coherency spectrum between density and potential fluctuations, channels 1 and 3.

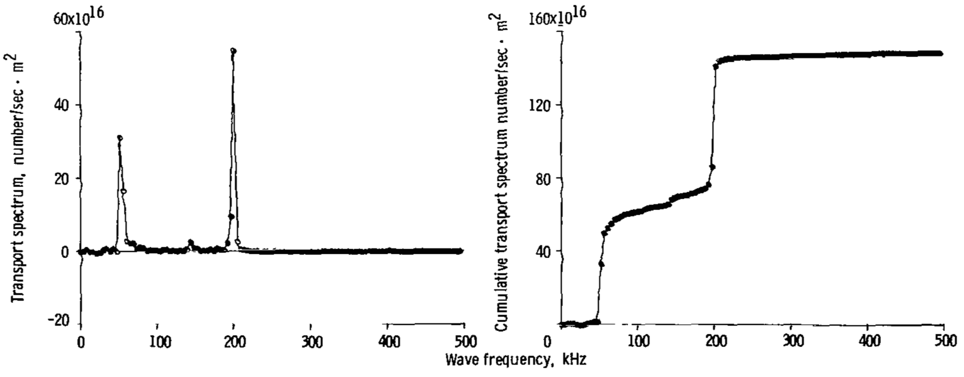

(g) Transport spectrum.

(h) Cumulative transport spectrum.

Figure 14. - Computer-generated spectra over frequency range 0 to 500 kilohertz - run AIN-2A (table I).

Figure 14 shows an example in which at least two discrete modes of oscillation were present in the plasma. The two discrete frequencies of approximately 50 and 200 kilohertz have amplitudes at least 10 and 100 times, respectively, greater than the background turbulent spectrum of the potential and density fluctuations. As is evident from the phase spectrum (fig. 14(c)), however, the entire plasma, including both the turbulent and discrete frequency bands, convected past the probes with a common drift velocity in the E/B direction. The dispersion relation was linear to at least 400 kilohertz. The coherence was highest at the peak frequencies and somewhat lower for the background turbulence. As is evident from figures 14(g) and (h), virtually all transport was associated with the two discrete rotating spokes, and ions were being convected radially inward at both frequencies.

## Amplitude Statistics

One method of determining the degree of randomness in the fluctuation data is to compare it against Gaussian random noise as a standard. This was done by taking the raw waveform amplitudes for density and potential fluctuations, such as those shown in figure 10, and apportioning the amplitudes among 30 positive and 30 negative discrete bins, which were used to form cumulative probability distributions. The amplitude statistics for the four runs in table I were plotted in figures 15 to 18. In each figure, part (a) is the cumulative probability of the potential fluctuations in channel 1, and part (b) is the cumulative probability of the density fluctuations in channel 3. The cumulative probability was plotted on probability paper, for which the abscissa (which represents the amplitude) had been normalized with respect to the standard deviation. To convert the abscissa to absolute units, multiply by the standard deviation given at the top of table II. It is a characteristic of probability paper that the cumulative probability of a Gaussian distribution will be a straight line on such a plot. The mean and standard deviations are given by the horizontal lines on these cumulative probability plots. The degree to which the cumulative probability of the potential or density fluctuations departs from a straight line is a measure of the extent to which the distribution departs from Gaussian noise.

Two other measures of the departure from a Gaussian distribution are mentioned in table II: skewness and kurtosis. Skewness, a normalized third moment of a probability distribution function, measures the degree of asymmetry about the mean value. For a Gaussian distribution, the skewness is zero. Kurtosis, a normalized fourth moment of a probability distribution function (see ref. 32 for further discussion), measures the degree of broadening of the distribution function about the mean value. For a Gaussian distribution, the kurtosis is 3.0.

## TABLE II. - AMPLITUDE STATISTICS AND SPECTRAL INDICES OF ILLUSTRATIVE EXPERIMENTAL RUNS

| Operating condition | Experimental run | | | |
|---|---|---|---|---|
| | AHN-18A | AHN-9A | AJH-2 | AIN-2A |
| Standard deviation: | | | | |
| Channel 1, V | 29 | 43 | 1.6 | 6.0 |
| Channel 2, V | 8.1 | 12 | 2.4 | 8.6 |
| Channel 3, particles/$m^3$ | $1.6\times10^{15}$ | $5.4\times10^{16}$ | $3.6\times10^{16}$ | $5.7\times10^{15}$ |
| Skewness: | | | | |
| Channel 1 | -0.07 | 0.44 | -0.22 | -0.17 |
| Channel 2 | -0.03 | 0.63 | -0.07 | 0.06 |
| Channel 3 | 0.06 | 0.54 | 0 | -0.32 |
| Kurtosis: | | | | |
| Channel 1 | 3.2 | 3.0 | 2.8 | 2.7 |
| Channel 2 | 3.3 | 3.9 | 2.9 | 2.7 |
| Channel 3 | 2.7 | 2.9 | 2.7 | 3.0 |
| Spectral index, p: | | | | |
| Channel 1 | 4.7 | 2.8 | 2.5 | 1.9 |
| Channel 2 | 3.6 | 2.9 | 2.7 | 2.2 |
| Channel 3 | 2.8 | 3.7 | 3.8 | 2.3 |
| Frequency proportional to wave number? | No | Yes | No | Yes |

Figures 15(a) and (b) show the cumulative probability distributions for the potential and density fluctuations, respectively, of the first experimental run in table I. They are consistent with the impression that the spectra shown in figure 11 are turbulent. Because the cumulative probability distribution is quite close to a straight line in both cases, the density and potential fluctuation spectra are shown to be Gaussian.

Figures 16(a) and (b) show the cumulative probability distributions for the potential and density fluctuations, respectively, of the second experimental run in table I. The corresponding fluctuation spectra are given in figure 12. Because these cumulative probability plots are not a straight line, the amplitude statistics are therefore non-Gaussian.

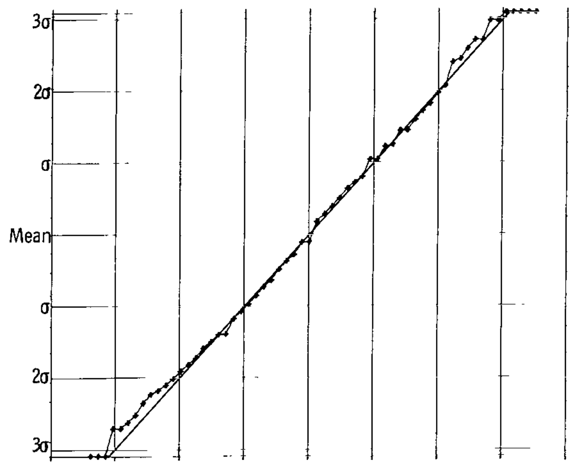

(a) Amplitude statistics of potential fluctuations in channel 1.

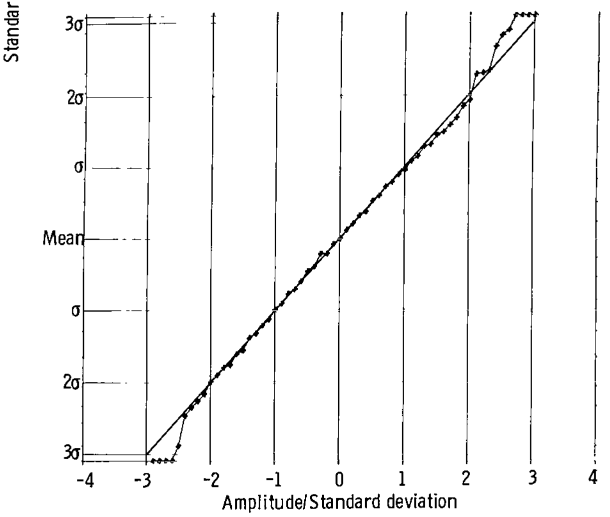

(b) Amplitude statistics of density fluctuations in channel 3.

Figure 15. - Amplitude statistics plotted on probability paper, with amplitude normalized with respect to standard deviation - run AHN-18A (tables I and II).

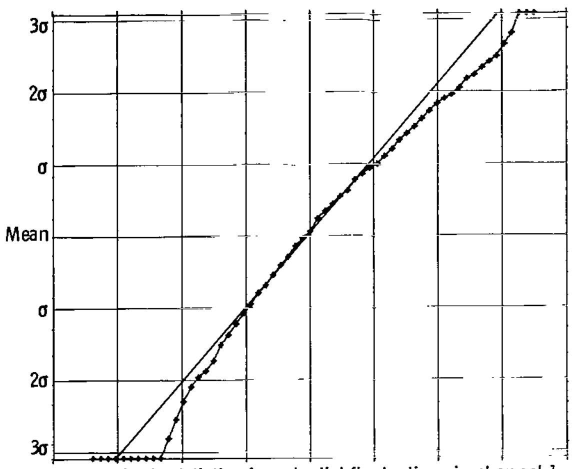

(a) Amplitude statistics for potential fluctuations in channel 1.

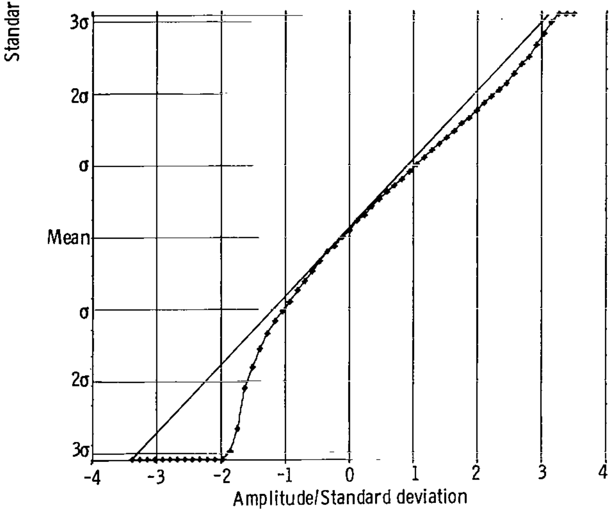

(b) Amplitude statistics for density fluctuations in channel 3.

Figure 16. - Amplitude statistics plotted on probability paper, with amplitude normalized with respect to standard deviation - run AHN-9A (tables I and II).

Figures 17(a) and (b) show the cumulative probability distributions of the potential and density fluctuations, respectively, of the third experimental run in table I. The corresponding fluctuation spectra, shown in figure 13, indicate turbulence. In this case, because the cumulative probability plots approximate a straight line, the amplitude statistics are shown to be Gaussian.

Finally, figures 18(a) and (b) show the cumulative probability plots for the highly coherent data of the fourth experimental run in table I. The corresponding fluctuation spectra are exhibited in figure 14. These amplitude statistics depart significantly from a Gaussian for large positive fluctuation amplitudes.

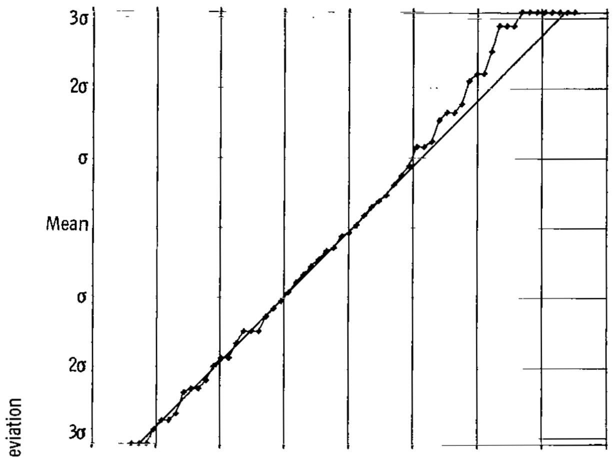

(a) Amplitude statistics for potential fluctuations in channel 1.

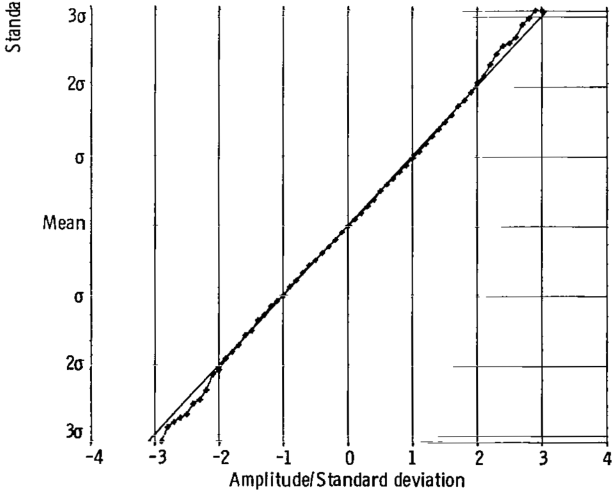

(b) Amplitude statistics for density fluctuations in channel 3.

Figure 17. - Amplitude statistics plotted on probability paper, with amplitude normalized with respect to standard deviation - run AJH-2 (tables I and II).

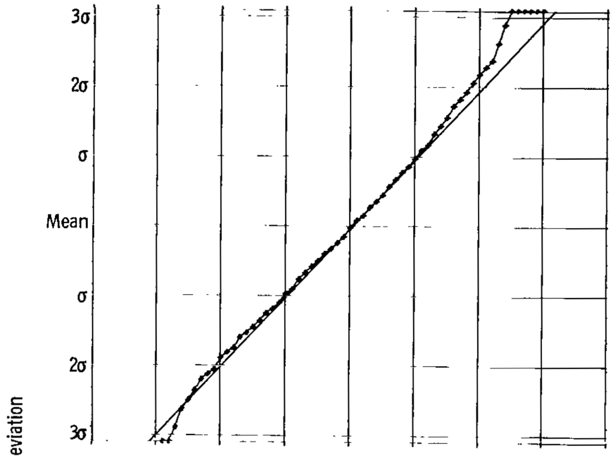

(a) Amplitude statistics for potential fluctuations in channel 1.

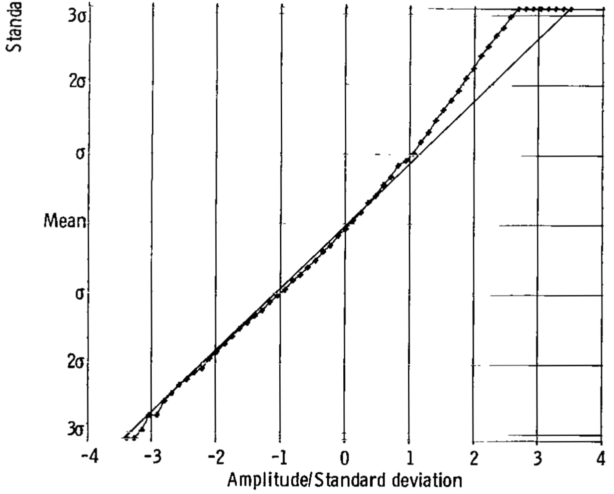

(b) Amplitude statistics for density fluctuations in channel 3.

Figure 18. - Amplitude statistics plotted on probability paper, with amplitude normalized with respect to standard deviation - run AIN-2A (tables I and II).

The four experimental runs selected as examples are characteristic of the general run of data in that the amplitude statistics are more nearly Gaussian than not. The standard deviation, skewness, and kurtosis of the four illustrative examples are listed in table II. The higher moments were normalized with respect to the standard deviation and are dimensionless quantities. No systematic trend of these moments with plasma operating conditions emerged from the data considered in this paper.

## Spectral Index

Previous investigation of plasma turbulence in a modified Penning discharge operated in an axisymmetric magnetic mirror geometry (ref. 25) revealed that the background electrostatic turbulence in such a plasma tended to obey a power law of the general form

$$\varphi^2 = \varphi_0^2 \nu^{-p} \tag{4}$$

where $\nu$ is the frequency and p is the spectral index. Available theories of plasma turbulence, cited in reference 25, predict that the spectral index should be 5.0. The results reported in reference 25 show that the spectral indices differed greatly from the predicted value of 5.0. Later investigations by Smith and Powers (ref. 41) in a drift-wave-dominated plasma appeared to indicate that the plasma turbulence obeyed equation (4), with the theoretically predicted spectral index of 5.0, whenever the dispersion relation $k(\omega)$ versus $\omega$ was linear (i.e., whenever the phase spectrum between channels 1 and 2 was a straight line).

For this plasma, in which drift waves were not observed, the frequency spectra of the potential and density fluctuations shown in figures 11 to 14 were plotted on log-log paper to exhibit the extent to which the spectra had a power-law form. The results were plotted in figures 19 to 22, where part (a) is the spectrum of potential fluctuations in channel 1 and part (b) is the spectrum of density fluctuations in channel 3. Since the square of the fluctuating quantity was plotted in both cases, the theoretically expected spectral index is 5.0.

Figure 19 shows the density and potential fluctuation spectra on log-log axes for the first experimental run in table I. These data were turbulent and had Gaussian amplitude statistics, with no prominent peaks at low frequencies. The data are characteristic in that the density and potential fluctuations had different spectral indices. Channel 2, the second capacitive probe, had a spectral index that differed from that of channel 1. This is consistent with the findings of reference 25 that the spectral index differed when electrostatic potential fluctuations were sampled at two different locations within the same plasma.

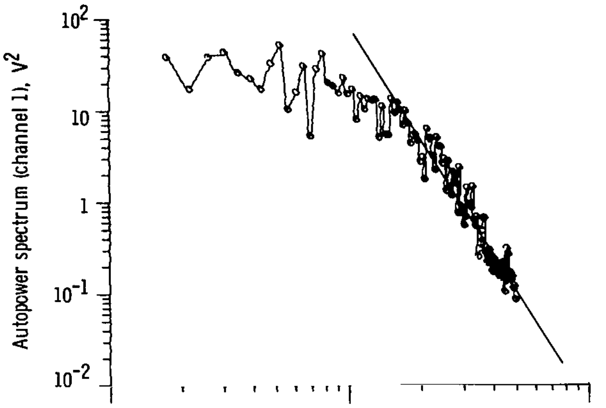

(a) Potential fluctuations, with spectral index of 4.7.

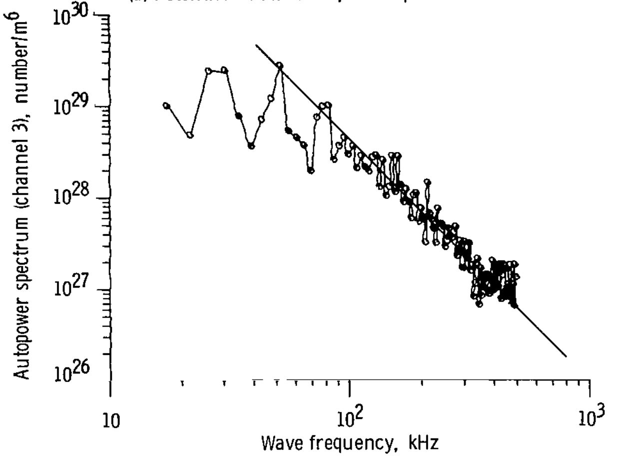

(b) Density fluctuations, with spectral index of 2.8.

Figure 19. - Amplitude spectrum of potential and density fluctuations plotted on log-log paper to exhibit power-law dependence of amplitude spectrum at high frequencies - run AHN-18A (table I).

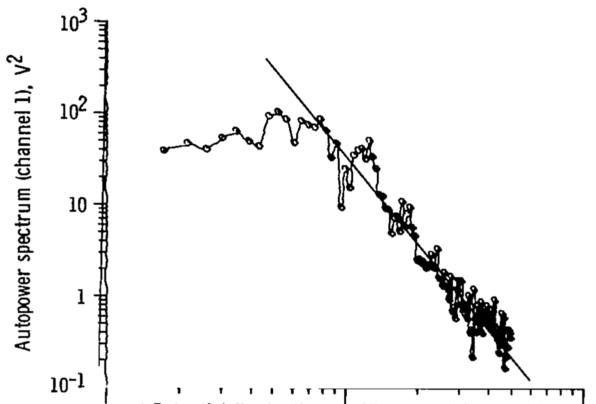

(a) Potential fluctuations, with spectral index of 2.8.

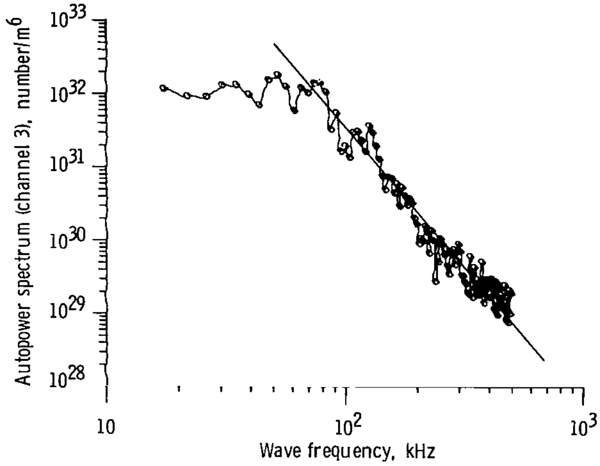

(b) Density fluctuations, with spectral index of 3.7.

Figure 20. - Amplitude spectrum of potential and density fluctuations plotted on log-log paper to exhibit power-law dependence of amplitude spectrum at high frequencies - run AHN-9A (table I).

Figure 20, for the quasi-turbulent second experimental run in table I, shows a broad frequency band from 100 to 500 kilohertz over which a straight line can be drawn through the spectra. The spectral indices differ for the density and potential fluctuations, and both differ substantially from the theoretically expected value of 5.0.

Figure 21 shows the third experimental run in table I, a turbulent case with negative electrode polarity. The region over which the potential fluctuation spectrum follows a straight line on the log-log paper is relatively limited, since the spectrum falls into the noise level at frequencies near 300 kilohertz.

Figure 22 shows the highly coherent fourth experimental run in table I. The coherent peaks are far above the background spectrum, but the background itself appears to obey a straight-line relationship, with spectral indices much less than the theoretical value of 5.0. This power-law dependence of the background spectrum is consistent with the observations reported in reference 25.

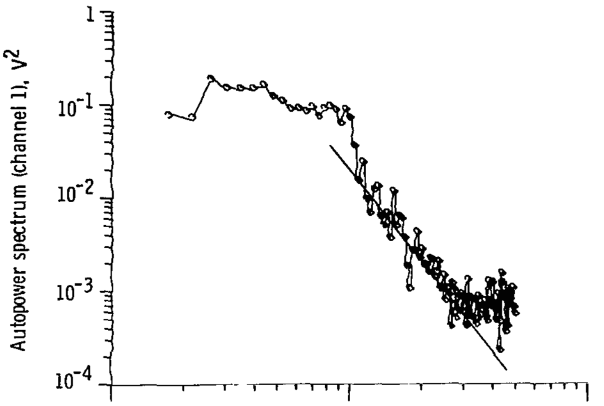

(a) Potential fluctuations, with a spectral index of 2.5.

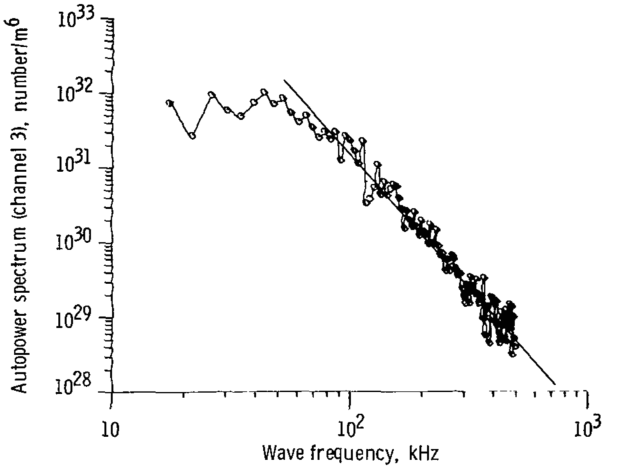

(b) Density fluctuations, with spectral index of 3.8.

Figure 21. - Amplitude spectrum of potential and density fluctuations plotted on log-log paper to exhibit power-law dependence of amplitude spectrum at high frequencies - run AJH-2 (table I).

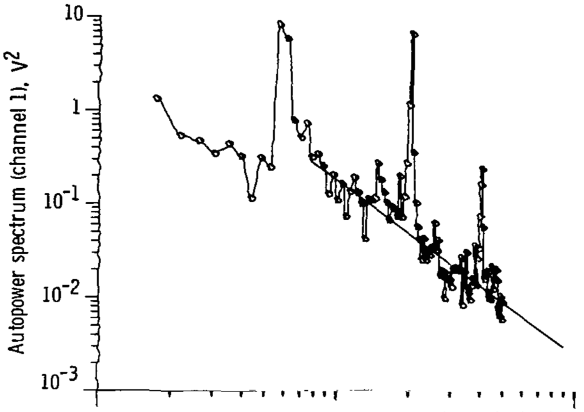

(a) Potential fluctuations, with a spectral index for background turbulence of 1.9.

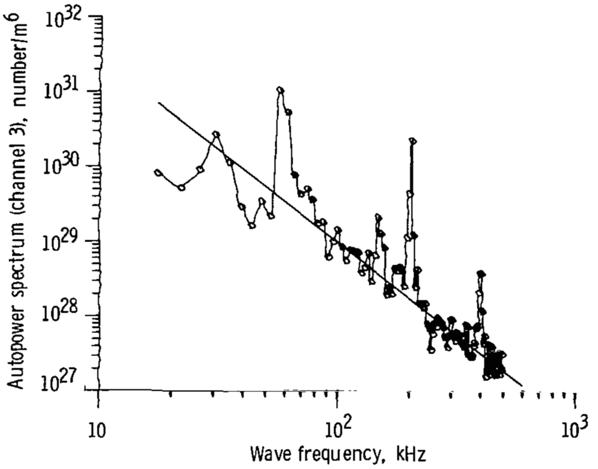

(b) Density fluctuations, with spectral index for background turbulence of 2.3.

Figure 22. - Amplitude spectrum of potential and density fluctuations plotted on log-log paper to exhibit power-law dependence at high frequencies - run AIN-2A (table I).

The spectral indices for the two potential fluctuation spectra and the one density fluctuation spectrum are given in table II for the four illustrative experimental runs in table I. No systematic trend of spectral index with operating parameters is evident. Fifteen additional experimental runs were reduced and their fluctuation spectra plotted on log-log paper. The resulting spectral indices for the potential and density spectra were obtained and are shown as scatter plots in figure 23, along with the data for the four experimental runs in table I. The spectral indices scatter over a wide range of values, most of which are below the theoretical value of 5.0. In some cases, the phase spectrum between channels 1 and 2 indicated that $\omega$ was not proportional to k (nonlinear dispersion relation) over the range in which the spectrum obeyed a power law, and these data

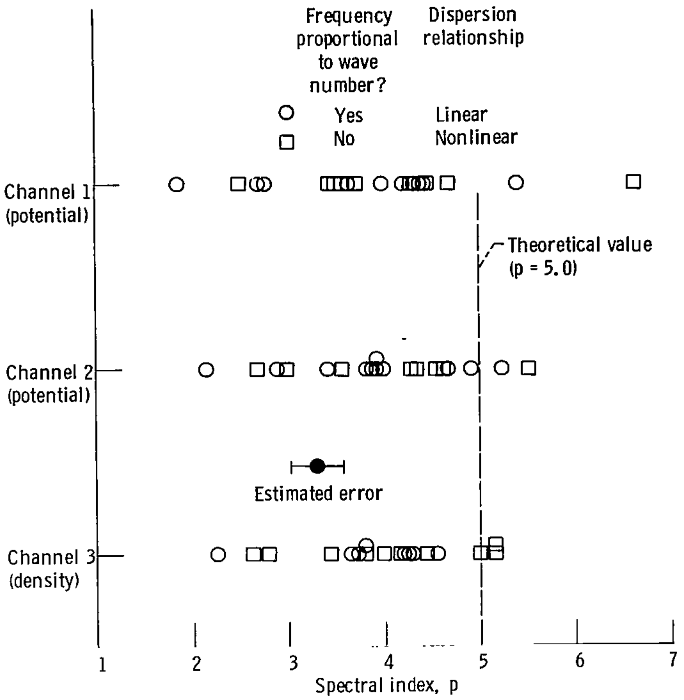

Figure 23. - Scatter plot of spectral indices of characteristic experimental runs.

were plotted as open squares. There were other runs for which $\omega$ was proportional to k over the range fitted by a power law (linear dispersion relation), and these data were plotted as open circles. The data associated with neither the linear nor the nonlinear dispersion relations agree with the theoretically expected spectral index of 5.0.

## Ion Heating and Thermalization

A characteristic feature of the plasmas generated in the modified Penning discharge and in the bumpy-torus facility has been the extraordinary degree of Maxwellianization of the ion energy distribution function (refs. 22 to 24, 26, and 27). It is self-consistent that a plasma highly turbulent in the way illustrated by the preceding data should also possess a Maxwellian ion energy distribution function. Indeed, previous work (refs. 24 to 26) indicated that the degree of Maxwellianization of the ion energy distribution function increased with increasing number density, magnetic field strength, and level of background turbulence. Ion energy distribution functions were not measured in the course of taking the data listed in table I. However, some characteristic ion energy distribution functions are shown in figure 24 to illustrate the degree of Maxwellianization that could be attained by this plasma.

Figure 24(a) shows an ion energy distribution function for deuterium gas, taken under conditions analogous to those of the third experimental run in table I. The reduced data from a charge-exchange neutral energy analyzer are shown by the open circles, and the best-fitting Maxwellian with an ion kinetic temperature of approximately 700 eV is shown by the triangular symbols. This distribution function is remarkable not only for the de-

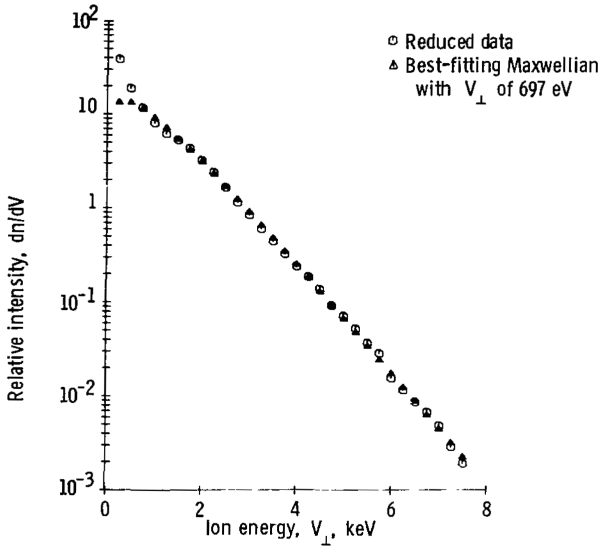

(a) Deuterium ion kinetic temperature, approximately 700 eV.

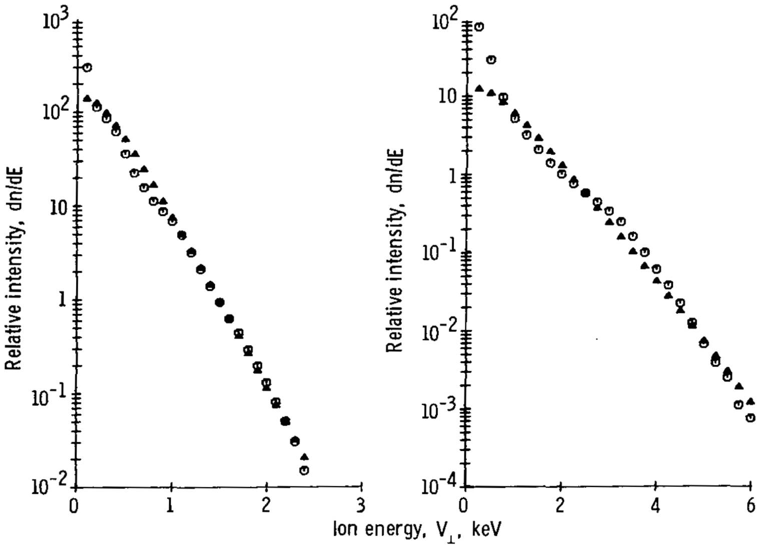

(b) Deuterium ion kinetic temperature, 220 eV.

(c) Deuterium ion kinetic temperature, 530 eV.

Figure 24. - Characteristic examples of highly Maxwellian ion energy distribution functions.

gree of Maxwellianization, but also for the great distance into the Maxwellian tail over which the distribution remained Maxwellian - over nine energy e-folding lengths.

Figure 24(b) shows an ion energy distribution function taken under operating conditions analogous to those for the fourth experimental run in table I. In this case, the ion kinetic temperature was approximately 220 eV, and the distribution function also remained Maxwellian over nine energy e-folding lengths.

Figure 24(c) shows an ion energy distribution function that departed slightly from a Maxwellian but that also extended about nine energy e-folding lengths into the Maxwellian tail. In this case, the applied electrode voltage (2 kV) was well within the region covered by the data. The presence of the electrode caused no perturbations in the distribution function, such as might result if the particles were accelerated in a sheath surrounding the electrode.

The preceding data are characteristic of the ion energy distribution functions observed in this plasma under the more turbulent, higher density, higher magnetic field regimes of operation. These distribution functions are consistent with the turbulent, random amplitude statistics prevalent in this plasma.

The high degree of randomness exhibited by this plasma suggests that coherent phenomena, which might serve as reservoirs of free energy to drive instabilities, were minimized. In other words, the plasma was already operating in the nonlinear limit of instabilities, without reservoirs of free energy in the plasma itself that could assist the plasma in escaping confinement. Thus, this plasma appears to satisfy the requirements for application of the Bohr - Van Leeuwen theorem discussed in reference 9.

## RADIAL PROFILES OF PLASMA CHARACTERISTICS

To properly interpret data on radial plasma transport, we obtained radial profiles of the parameters that might affect it. These parameters included the relative number density and the floating potential, as well as the transport rate itself.

Radial profiles of relative number density were made by noting the current on a Langmuir probe biased to ion saturation as it probed various radial positions. These measurements immediately preceded those of the transport rate and used the same probe and probe assembly. The radial profile of floating potential was made by allowing the Langmuir probe to float and measuring the floating potential with a high-impedance voltmeter.

The radial span over which data could be taken was limited by damage to the probes as they penetrated toward the axis of the plasma and, in the outward direction, by the limited travel of the probe assembly.

TABLE III. - OPERATING CONDITIONS FOR EXPERIMENTAL RUNS

TO MEASURE RADIAL PROFILES

[Number of electrodes, 1; electrode location, sector 6; electrode current, $I_a$, 2.0 A; background neutral gas pressure, $p_0$, $2.6\times10^{12}$ particles/cm$^3$ ($7.6\times10^{-5}$ torr).]

| Operating condition | Experimental run series | | | |
|---|---|---|---|---|
| | AJV | AJT | AJZ | AJX |
| Type of electrode | Stainless-steel rod | Stainless-steel rod | Standard D | Standard D |
| Electrode polarity | Positive | Negative | Positive | Negative |
| Electrode voltage, $V_a$, kV | 0.40 | -2.50 | 0.47 | -4.1 |
| Average electron number density, $\bar{n}_e$, cm$^{-3}$ | $1.0\times10^{11}$ | $5.0\times10^{11}$ | $0.89\times10^{11}$ | $3.1\times10^{11}$ |
| Particle confinement time, $\tau$, msec | 0.68 | 3.3 | 0.60 | 2.1 |
| Electric field direction | Outward | Inward | Outward | Inward |

Radial profiles of the plasma characteristics were taken for two electrode configurations: the standard D-shaped electrode (fig. 3) and the dual, stainless-steel tube electrode (fig. 4). The plasma was generated by a single electrode in sector 6, two sectors away from the probe assembly located in sector 4. The operating conditions for which these radial profiles were taken are listed in table III and provide paired comparisons of positive and negative polarities for each of the two electrode configurations. The arbitrary zero position of the probe was approximately 1 centimeter inside the visible plasma boundary and approximately 7 centimeters from the geometric axis of the plasma. As shown later, the geometric axis of the plasma and the axis of rotation of the rotating disturbances do not necessarily coincide.

## Radial Profiles of Relative Number Density

Figure 25 shows radial profiles of relative plasma number density obtained from the ion saturation voltage appearing across a 1000-ohm resistor connected to a biased Langmuir probe. These four radial profiles correspond to the four sets of operating conditions in table III. The relative number densities with positive polarity were approximately 1/5 or 1/6 of the relative number densities characteristic of negative polarity,

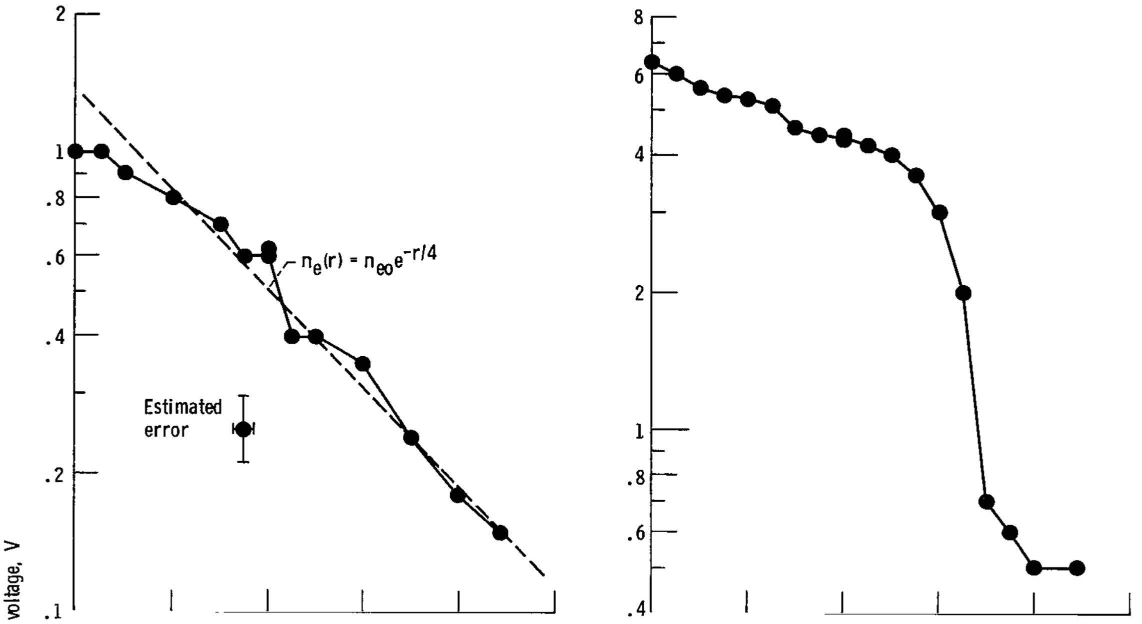

(a) Run series AJV.

(b) Run series AJT.

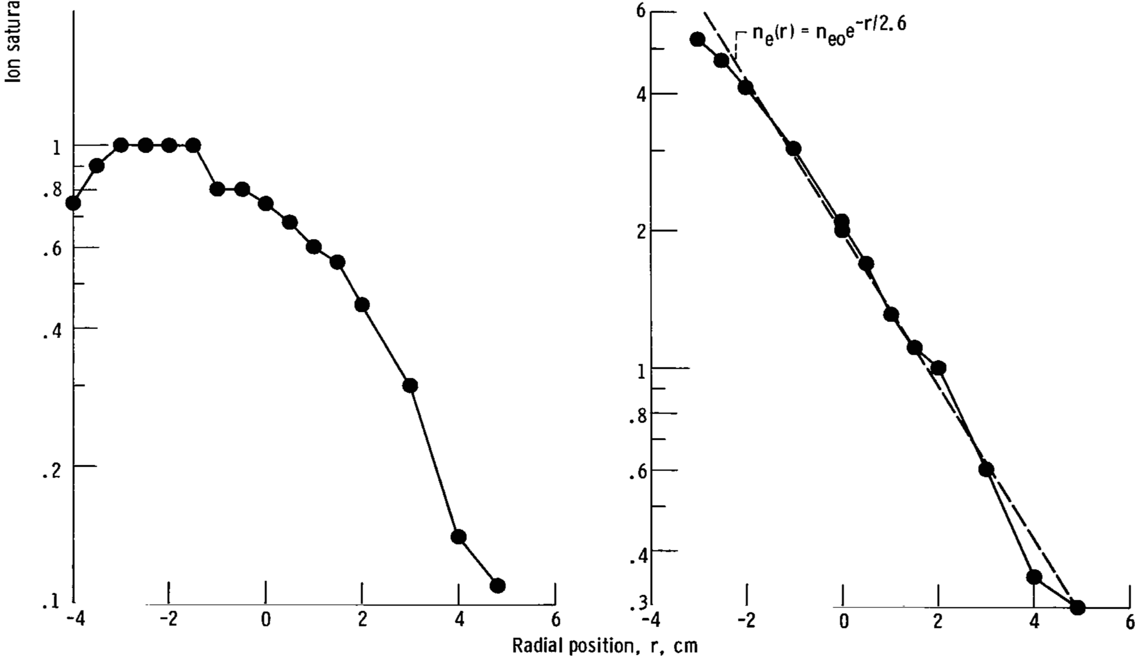

(c) Run series AJZ.

(d) Run series AJX.

Figure 25. - Radial profiles of ion saturation voltage (relative ion number density) for conditions listed in table III.

in agreement with the previously observed tendency of confinement to be improved by electric fields pointing radially inward. In two cases (figs. 25(a) and (d)) the radial density profiles assumed an exponential dependence on radius, with characteristic e-folding lengths of 4 centimeters in figure 25(a) and 2.6 centimeters in figure 25(d). For the run with the standard D-shaped electrode and negative polarity (fig. 25(c)), the axis of plasma was only about 2.5 centimeters radially inward from the arbitrary zero position for the radial measurements, as is evident by the maximum in the relative number density.

## Radial Profiles of Floating Potential

The radial profiles of floating potential were measured by inserting the Langmuir probe to various radial positions and allowing it to assume a floating potential during its 0.3-second dwell time within the plasma. As shown in figure 9, this dwell time permitted the floating potential to achieve a steady state, which is believed to be characteristic of the plasma potential at the radius being sampled. Figure 26 shows the floating potentials measured as a function of radial position. In figures 26(a), (b), and (d), the potential profile could be approximated by an exponential function over a portion of its length, with characteristic e-folding lengths of about $1\frac{1}{2}$ centimeters. This characteristic scaling distance is comparable to the ion gyro diameter, for ion energies of about 400 eV, but is at least 50 times greater than the relevant Debye length. It is also clear from the profiles in figure 26 that electric fields in excess of 100 volts per centimeter penetrated at least halfway to the plasma axis.

A comparison of figures 25(c) and 26(c) shows that, although the density profile passed through a maximum at a radial position of approximately -2.5 centimeters, the floating potential profile did not reach a maximum 4 centimeters into the plasma. It appears that, for this third set of operating conditions (table III), the axis of the density distribution did not coincide with the axis of the electrostatic potential distribution. It is also evident from these floating potential profiles that, near the plasma boundary, the electric field pointed radially inward when the plasma was negatively biased and radially outward when the plasma was positively biased.

## Radial Profiles of Ion Transport Rate

Data were taken that should have yielded radial profiles of the ion transport rate for the four sets of operating conditions in table III. Upon reducing the data, we found that the coherence of the signals for the second and fourth sets was so low that the computer program used to analyze the data could not determine a meaningful transport spectrum. It was possible, however, to obtain radial profiles of the ion transport rate for the positive polarity data for the first and third sets of operating conditions.

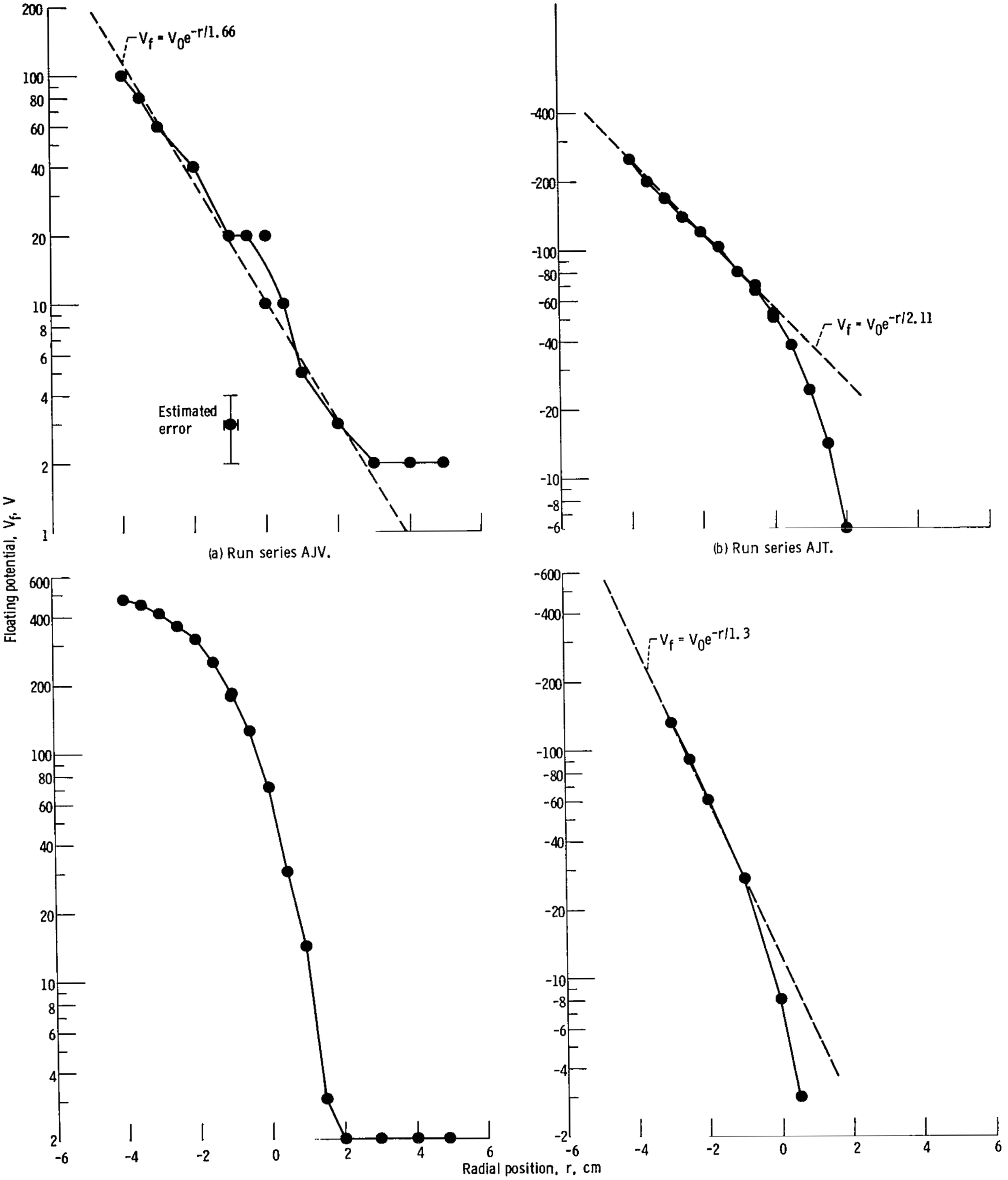

(a) Run series AJV.

(b) Run series AJT.

(c) Run series AJZ.

(d) Run series AJX.

Figure 26. - Potential measurements obtained from floating Langmuir probe for conditions listed in table III.

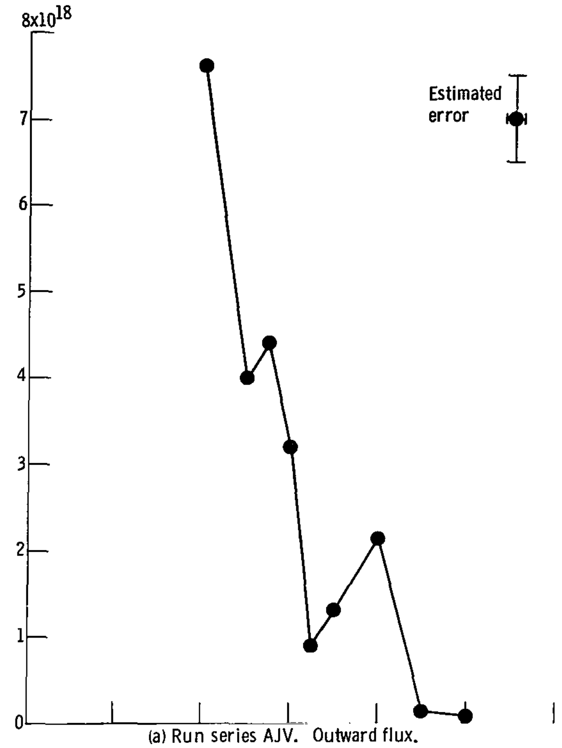

(a) Run series AJV. Outward flux.

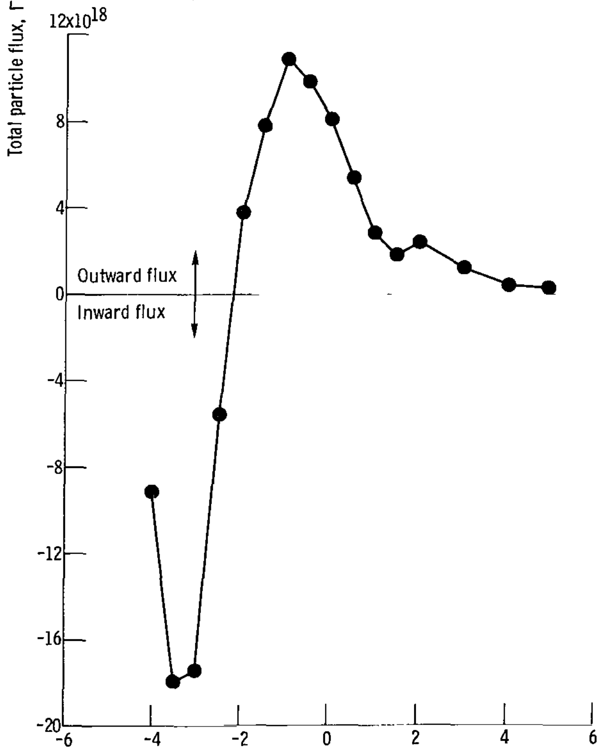

(b) Run series AJZ. Inward and outward flux.

Figure 27. - Radial profile of ion particle flux for two experimental run series listed in table III.

Figure 27(a) shows the radial profile of outward ion flux as a function of radius for the first set of operating conditions in table III and the density and potential profiles in figures 25(a) and 26(a), respectively. It is evident that the radial transport rate of the outward flux increased substantially as the probe moved inward toward the center of the plasma, with a possible local maximum near the outskirts of the plasma at +2 centimeters.

Figure 27(b) shows the radial profile of outward ion flux for the third set of operating conditions in table III and the density and potential profiles in figure 25(c) and 26(c), respectively. In this case, the radial transport rate of the outward flux decreased as the probe moved radially outward from the starting point. As the probe moved into the plasma, the direction of particle flux reversed and was radially inward for the innermost four points. The density reached a maximum at approximately -2 centimeters (fig. 25(c)). The probe assembly appears to have traversed the plasma axis and to have seen a declining density profile on the other side of the plasma axis, where the ion flux was radially outward toward the major vertical axis of the toroidal array. The maximum outward ion flux shown in figure 27(b) corresponds to a current density of about 1.6 amperes per square meter.

## FUNCTIONAL DEPENDENCE OF PLASMA CHARACTERISTICS

A series of paired comparisons were made to determine the effects of electrode polarity and configuration on the scaling of confinement-related plasma characteristics. Two electrode configurations were investigated: the dual, stainless-steel tube electrode inserted across a minor diameter of the plasma (fig. 4) and the standard D-shaped electrode (fig. 3). The operating conditions used for the individual experimental runs are listed in table IV. The independent parameters varied during a particular run are indicated as "variable" in the appropriate column entry.

TABLE IV. - OPERATING CONDITIONS FOR EXPERIMENTAL RUNS TO DETERMINE PARAMETRIC VARIATIONS

[Number of electrodes, 1; electrode location, sector 6.]

| Operating condition | Experimental run series | | | | | | | |
|---|---|---|---|---|---|---|---|---|
| | AJW | AJU | AKA | AJY | AKC | AKF | AKB | AKE |
| Type of electrode | Stainless-steel rod | Stainless-steel rod | Standard D | Standard D | Stainless-steel rod | Standard D | Stainless-steel rod | Standard D |
| Electrode polarity | Positive | Negative | Positive | Negative | Negative | Negative | Negative | Negative |
| Electrode current $I_a$, A | Variable | Variable | Variable | Variable | 2.0 | 2.0 | 2.0 | 2.0 |
| Background neutral-gas pressure, $p_0$, particles/cm$^3$ (torr) | $2.6\times10^{12}$ $(7.6\times10^{-5})$ | $2.6\times10^{12}$ $(7.6\times10^{-5})$ | $2.6\times10^{12}$ $(7.6\times10^{-5})$ | $2.6\times10^{12}$ $(7.6\times10^{-5})$ | Variable | Variable | $2.6\times10^{12}$ $(7.6\times10^{-5})$ | $2.6\times10^{12}$ $(7.4\times10^{-5})$ |
| Electric field direction | Outward | Inward | Outward | Inward | Inward | Inward | Inward | Inward |

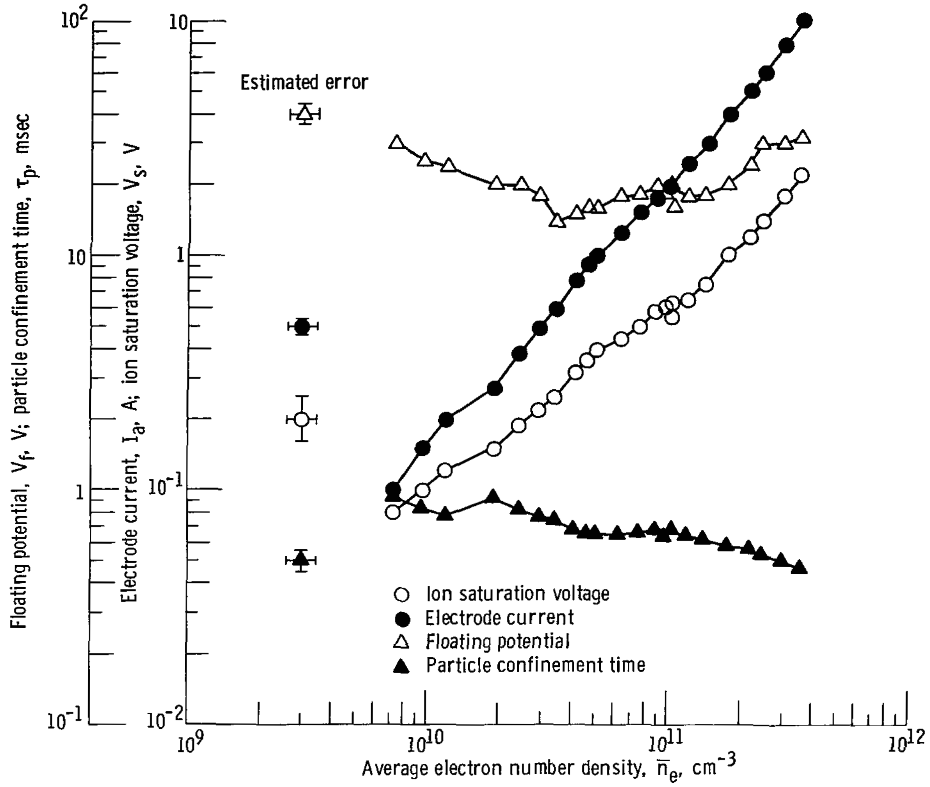

Figure 28. - Parametric variation of particle confinement time, floating potential, electrode current, and ion saturation voltage (relative ion number density) as function of average electron number density - run series AJW (table IV).

## Dependence on Electron Number Density

Figure 28 shows the functional dependence of the electrode current $I_a$, the Langmuir probe voltage proportional to the ion saturation current at the zero radial position $V_s$, the Langmuir probe floating potential at the zero radial position $V_f$, and the particle confinement time $\tau_p$ based on the average electron number density measured by the microwave interferometer. The method used to determine $\tau_p$ is described later, in the section Calculation of Particle Confinement Time. These data were taken for the first set of operating conditions in table IV, for positive polarities, with the stainless-steel tube electrode.

The ion saturation current (ion number density) was linearly proportional to the average electron number density, suggesting that the radial profiles of ion number density did not change for the various electron number densities shown. The electrode current increased more rapidly than a direct proportionality to the number density, a consequence of the slowly decreasing particle confinement time with increasing average number density. Because the floating potential varied by only a factor of 2 over the range of number densities shown, the floating potential profiles were probably geometrically similar over this range.

Figure 29 shows similar data for the same electrode but with negative polarity. Because both the ion saturation current and the electrode current were linearly proportional to the average electron number density, the density profiles were probably geometrically similar over the range of number densities shown. The particle confinement time was almost independent of average number density over more than a factor-of-50 variation in these quantities, and the floating potential varied relatively little over the same range. The radial profiles of the floating potential were probably geometrically similar over the range of number densities shown.

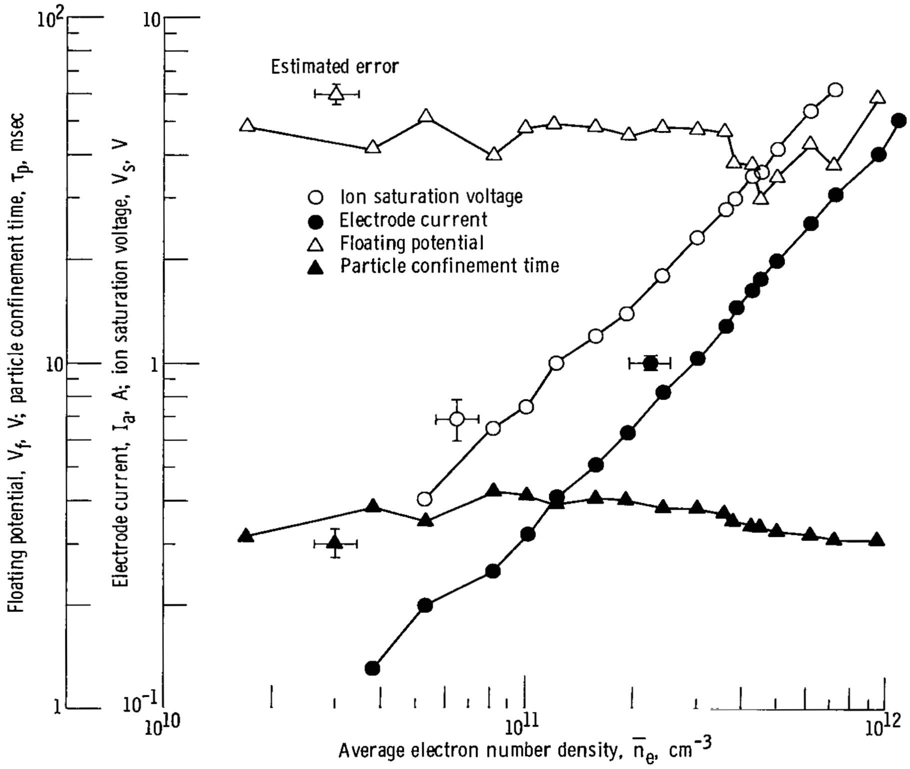

Figure 29. - Parametric variation of particle confinement time, floating potential, electrode current, and ion saturation voltage (relative ion number density) as functions of average electron number density - run series AJU (table IV).

Figure 30 shows the same parameters as a function of average electron number density for the standard D-shaped electrode with positive polarity. Because the floating potential was almost independent of electron number density, the radial profiles were probably geometrically similar over this density range. The particle confinement time slowly decreased with increasing density. Because the voltage proportional to the ion saturation current on the Langmuir probe was almost directly proportional to the average number density, the radial profiles of density were probably geometrically similar over the range of densities shown.

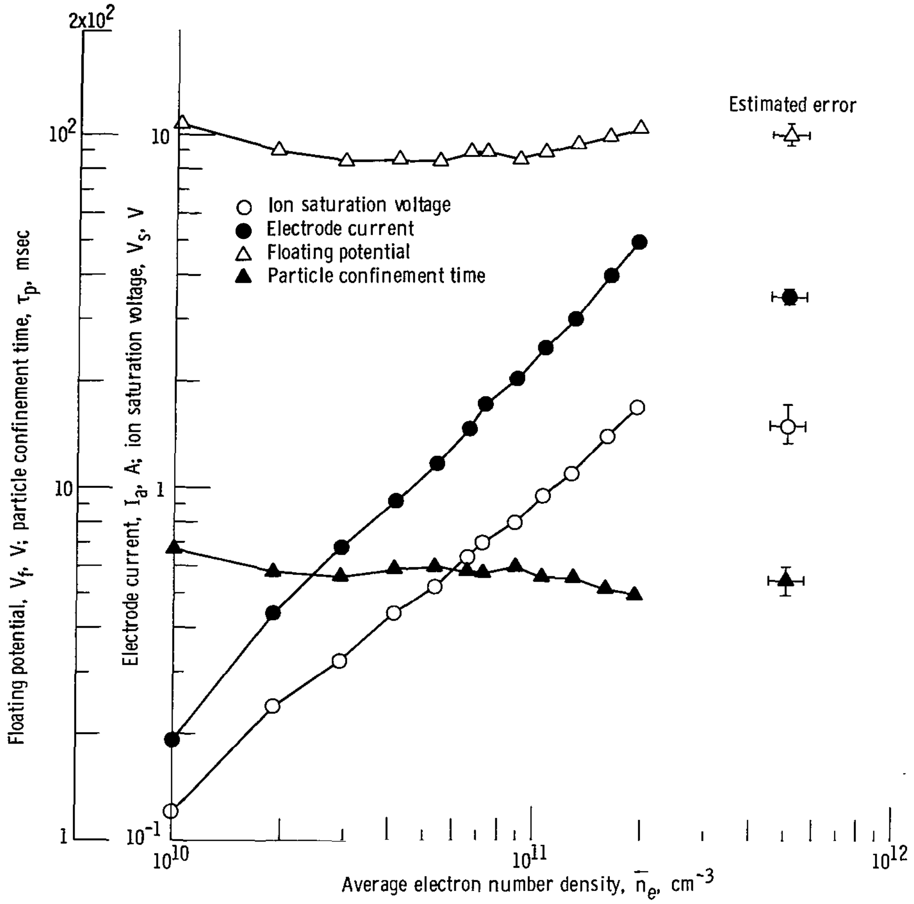

Figure 30. - Parametric variation of particle confinement time, floating potential, electrode current, and ion saturation voltage (relative ion number density) as function of average electron number density - run series AKA (table IV).

Figure 31 shows the same four parameters as a function of average electron number density for the standard D-shaped electrode with negative polarity. The floating potential changed substantially with average number density, and the particle confinement time dropped by more than a factor of 2 over the same range. Because the voltage proportional to the ion saturation current was linearly proportional to the average number density, the radial profiles of number density were probably geometrically similar over the range of number densities shown. Although the floating potential and the particle confinement time for the three preceding figures were relatively independent of average number density, it is evident from figure 31 that, for the standard D-shaped electrode with negative polarity, these parameters were a function of the average electron number density.

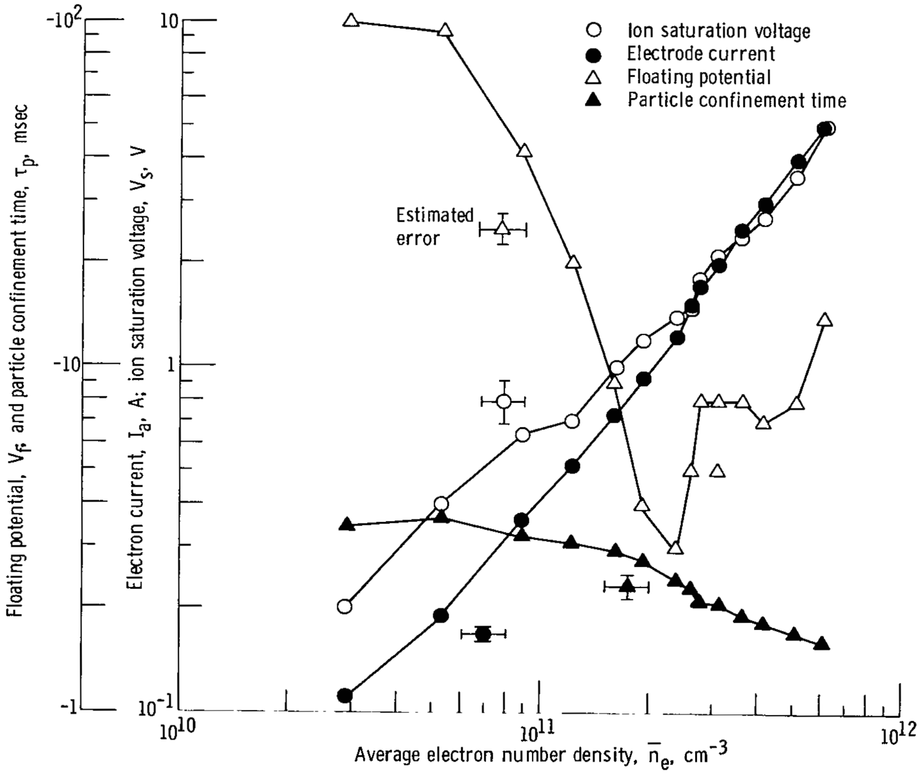

Figure 31. - Parametric variation of particle confinement time, floating potential, electrode current, and ion saturation voltage (relative ion number density) as functions of average electron number density - run series AJY (table IV).

## Effect of Electrode Polarity

The effect of electrode polarity on the particle confinement time and the average electron number density is illustrated by replotting the results for the first four experimental runs of table IV in figure 32. With positive electrode polarity the particle confinement time ranged from about 0.5 to 0.9 millisecond, but with negative polarity and the radial electric field pointing inward the particle confinement time ranged from 4.5 down to 1.6 millisecond. It is evident from figure 32 that negative polarity, with the radial electric field pointing inward, offered substantially improved particle confinement over that possible with positive polarity and the radial electric field pointing outward. It is also clear that the dual, stainless-steel tube electrode (fig. 4) provided longer confinement times than the standard D-shaped electrode. In addition, the particle confinement time did not drop off as rapidly with increasing plasma number density as it did with the standard D-shaped electrode.

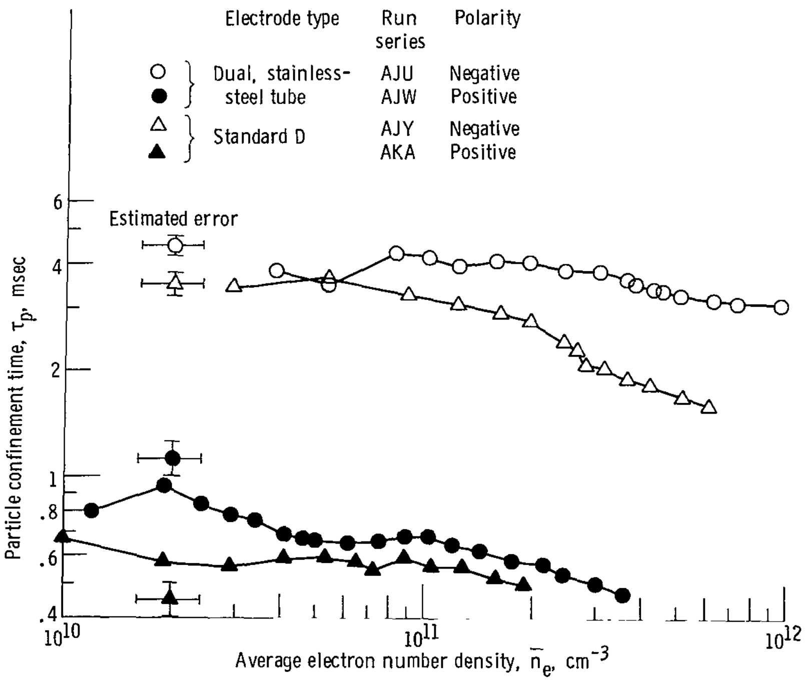

Figure 32. - Particle confinement time as function of average electron number density - run series AJW, AJU, AKA, and AJY (table IV).

The improved confinement can also be exhibited in terms of average electron number density at a given electrode current. In figure 33 the average number density is plotted as a function of electrode current for the first four sets of operating conditions in table IV. At a given electrode current, the average number density was at least 5 times higher with negative electrode polarity and an inward-pointing electric field than with positive polarity and an outward-pointing electric field. The improved confinement associated with the stainless-steel tube electrode was evident in that it produced number densities about 1.5 times higher than those of the standard D-shaped electrode. In addition, the average number density with the tube electrode was almost directly proportional to the electrode current, rather than tending to fall off with increasing electrode current as did the density with the standard D-shaped electrode.

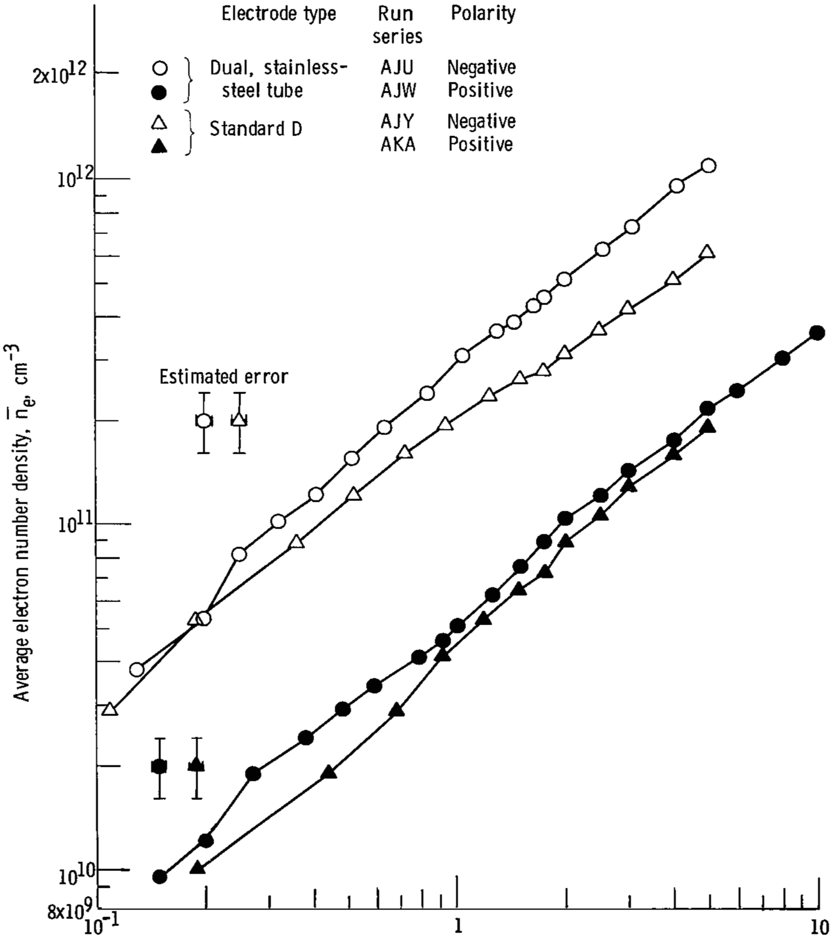

Figure 33. - Average electron number density as function of electrode current - run series AJW, AJU, AKA, and AJY (table IV).

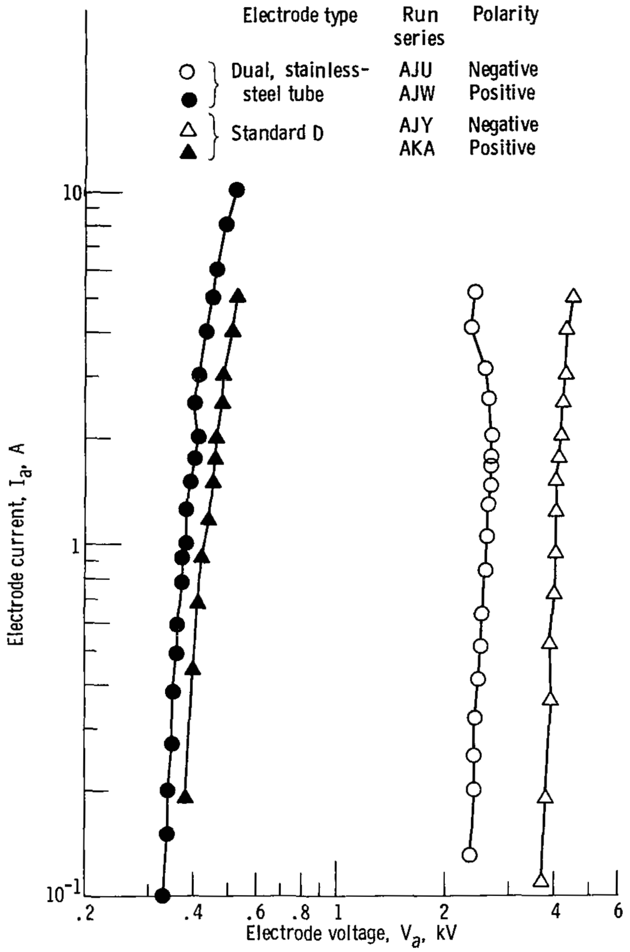

Figure 34. - Current-voltage characteristics of plasmas used in run series AJW, AJU, AKA, and AJY (table IV).

## Current-Voltage Curves for Plasma

The plasma current-voltage curves that were mapped out in the course of the parametric variations shown for the first four experimental runs in table IV are shown in figure 34. The current-voltage curves have a near-infinite slope with some evidence of a negative resistance in the stainless-steel tube electrode at higher electrode currents. For positive polarities, and for reasons that are not understood, the current-voltage curves exhibited very low electrode voltages (~400 V). The voltages associated with negative polarity operation were about 2.5 and 4 kilovolts for the stainless-steel tube electrode and the standard D-shaped electrode, respectively. When the object is to heat ions effectively, it is desirable to have the highest possible radial electric fields since these fields are proportional to the electrode voltage. For this reason, the electrode voltages associated with positive polarity operation are of minimal interest. Based on the scaling laws discussed in reference 23, the ion kinetic temperatures associated with positive polarity operation would be about one-eighth of the ion kinetic temperatures associated with negative polarity operation.

## Effect of Neutral Gas Pressure

The floating potential, particle confinement time, and average electron number density were measured as functions of background deuterium gas pressure for the fifth and sixth sets of operating conditions in table IV. Figure 35 shows these parameters as a function of background gas pressure for negative polarity operation of the dual, stainless-steel electrode. Because the particle confinement time and average number density were virtually independent of the background gas pressure over a factor-of-3 variation in this quantity, they probably were not determined by binary collisions with the background deuterium gas. But because the floating potential varied significantly over this pressure range, the shape of its radial profile, and hence the radial electric field, probably does depend on the gas pressure.

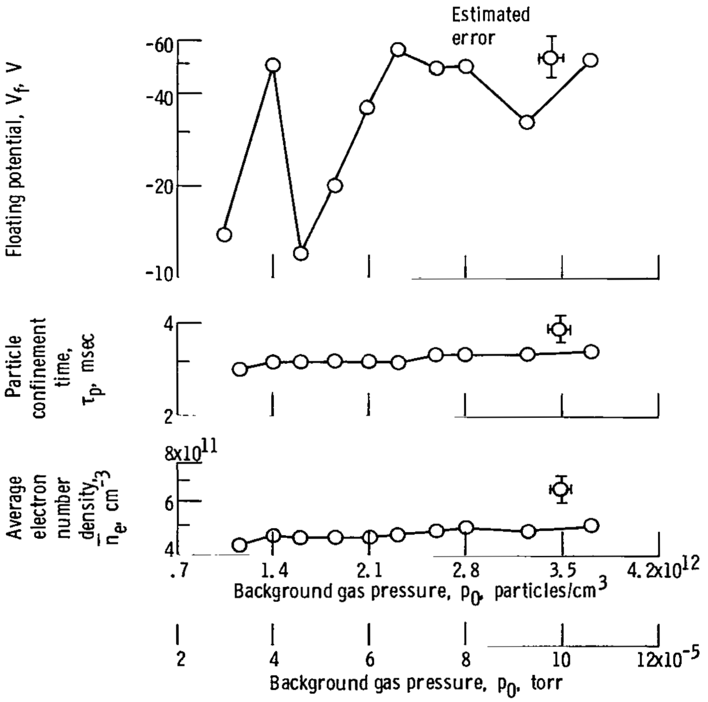

Figure 35. - Floating potential, particle confinement time, and average electron number density as functions of background gas pressure of deuterium - runs series AKC (table IV).

Figure 36 shows the same three parameters as functions of background gas pressure for negative polarity operation with the standard D-shaped electrode. In this case, there was a systematic functional dependence of all three parameters on background gas pressure, with all three increasing as the background gas pressure increased. The reason why the electrode configuration should affect the functional dependence of these parameters on background gas pressure is not clear.

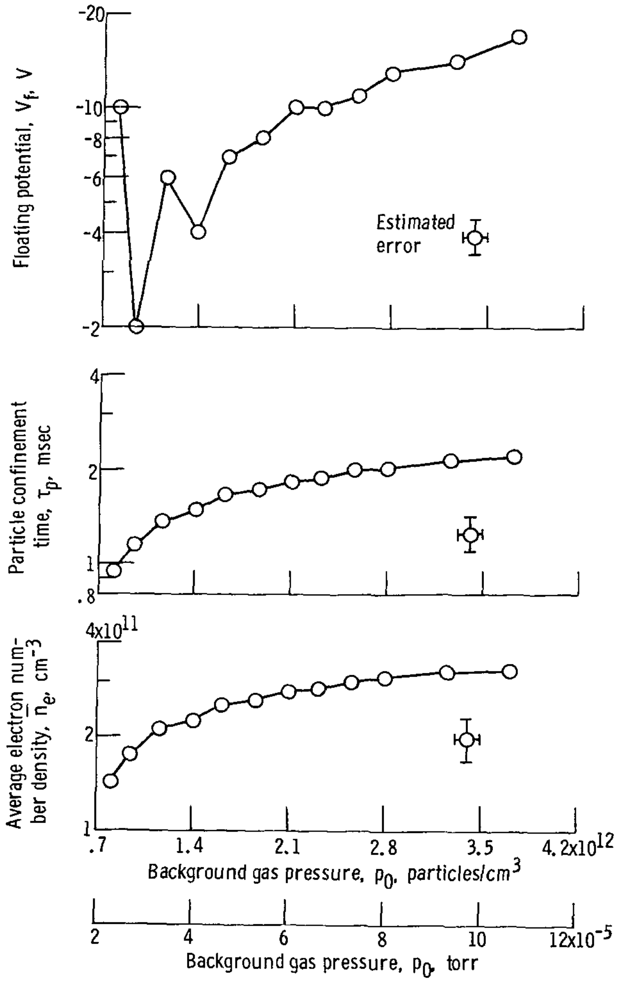

Figure 36. - Floating potential, particle confingement time, and average electron number density as functions of background gas pressure of deuterium - run series AKF (table IV).

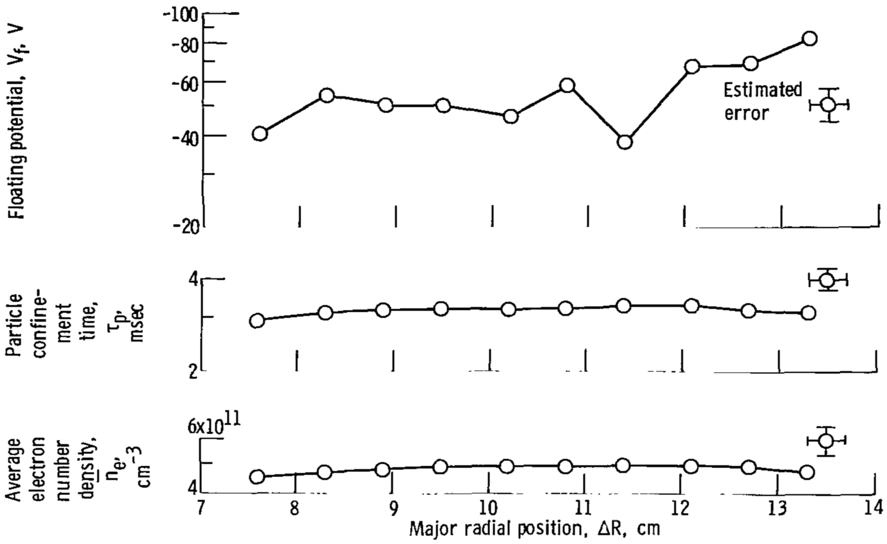

Figure 37. - Floating potential, particle confinement time, and average electron number density as functions of major radial position of stainless-steel tube electrode - run series AKB (table IV).

## Effect of Major Radial Position

The major radial positions of the dual, stainless-steel tube electrode and the standard D-shaped electrode were varied for the seventh and eighth sets of operating conditions in table IV. Figure 37 shows how the floating potential, the particle confinement time, and the average electron number density depend on the major radial position of the stainless-steel tube electrode over a range of 6 centimeters and for negative polarity. The particle confinement time and average number density were independent of the major radial position over this range. But there was a slight tendency of the floating potential to increase as the major radial position of the electrode was moved radially outward toward the probe position.

The same parameters are plotted in figure 38 for the standard D-shaped electrode with negative polarity. In this case, the particle confinement time and average number density were also independent of major radial position, but the floating potential tended to increase significantly as the D-shaped electrode approached the radial position of the probe itself. The plasma quenched when the D-shaped electrode was moved beyond the 11-centimeter major radial position.

The major radial positions plotted in figures 37 and 38 were measured from an arbitrary zero position on the outside face of the inner spacer bars that separated the coils. It appears that, although the major radial position did affect the profile of the electrostatic potential, it did not affect the particle confinement time or the plasma electron number density.

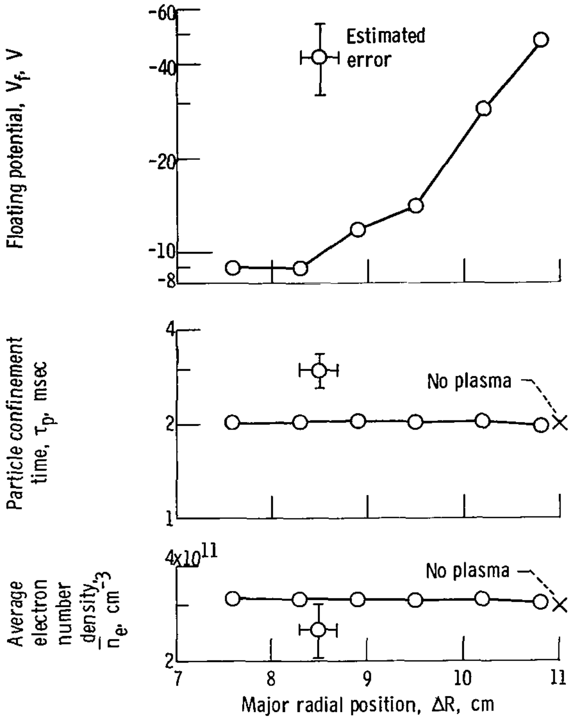

Figure 38. - Floating potential, particle confinement time, and average electron number density as functions of major radial position of standard D-shaped electrode - run series AKE (table IV).

## FUNCTIONAL DEPENDENCE OF RADIAL TRANSPORT

The dependence of radial transport on plasma radius has already been discussed. A series of experimental runs using the transport diagnostic were made to determine the dependence of the radial ion flux on electrode polarity, on electrode current, and on the value of a weak, vertical magnetic field applied to the plasma by two "trim" coils wrapped around the outer circumference of the vacuum tank.

### Dependence on Electrode Polarity

The effect of the direction of the electric field on particle confinement time and electron number density is shown in figure 39 for the first two sets of operating conditions in table V. The only conditions that differed were the polarity of the two midplane electrode rings used and the geometric position of the midplane electrodes, which was optimized for each polarity (ref. 28). The solid symbols represent positive polarity, for which the radial electric field points (and pushes ions) radially outward. The open symbols represent negative polarity, for which the radial electric field points (and pushes ions) radially inward. Both the particle confinement time and the average electron number density were at least five times higher when the radial electric field pointed inward than when it pointed outward.

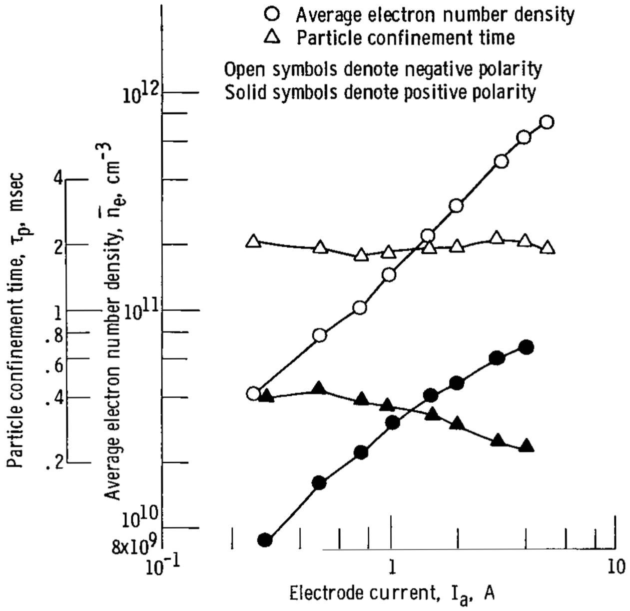

Figure 39. - Average electron number density and particle confinement time as functions of electrode current for positive and negative electrode polarity - run series AHN 1-9 and AHN 18-25 (table V).

TABLE V. - OPERATING CONDITIONS FOR PARAMETRIC

TRANSPORT RUNS

[Number of electrodes, 2; type of electrode, standard D; electrode location, sectors 5, 6; background neutral gas pressure, $p_0$, $1.8\times10^{12}$ particles/cm$^3$ ($5.3\times10^{-5}$ torr).]

| Operating condition | Experimental runs | | |
|---|---|---|---|
| | AHN 1-9 | AHN 18-25 | AHF 13-24 |
| Electrode polarity | Negative | Positive | Negative |
| Electrode voltage, $V_a$, kV | Variable | Variable | 2.50 |
| Electric field direction | Inward | Outward | Outward |

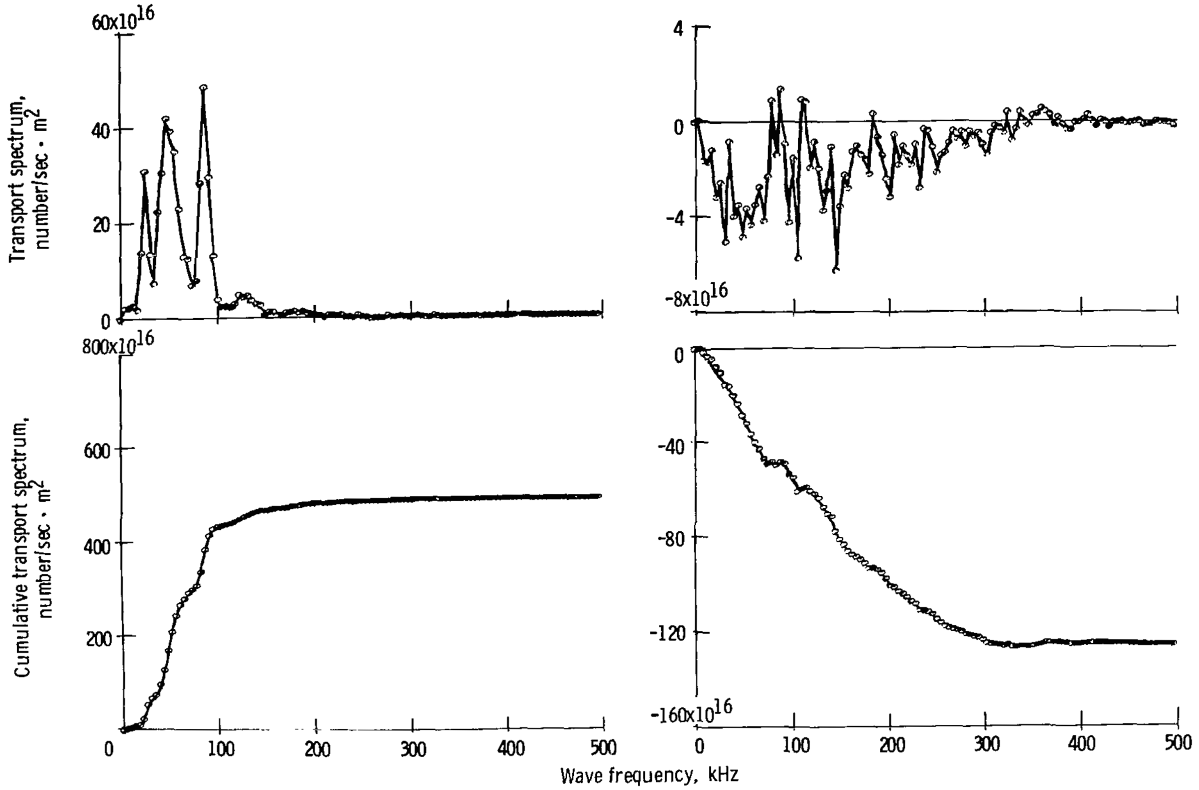

(a) Negative electrode polarity. Run AHN 3 (table V).

(b) Positive electrode polarity. Run AHN 20 (table V).

Figure 40. - Characteristic transport and cumulative transport spectra for electrode current of 0.75 A.

Figure 40 shows four characteristic transport spectra that correspond to an electrode current of 0.75 ampere, which is plotted in figure 39. There are two spectra for negative electrode polarity and two for positive electrode polarity. In each case the upper graph is the transport spectrum $T(\omega)$, and the lower graph is the ion cumulative transport up to the frequency shown on the abscissa. In figure 40(a), the negative electrode with a radially inward-pointing electric field has a transport spectrum that is positive in sign, indicating radially inward transport. The transport is associated with three discrete peaks below 150 kilohertz. For this condition, the ion flux was radially outward in the sheaths that surrounded the negative electrodes, and the net ion confinement was a balance between infusion in the empty sectors and losses in the sectors with electrode rings. In figure 40(b), the positive electrode has a transport spectrum that is negative in sign, indicating radially outward transport toward the surrounding walls. This outward transport occurred over a broad frequency band out to 350 kilohertz and could be considered "turbulent transport."

### Dependence on Electrode Current

The asymptotic cumulative transport for the two electrode polarities shown in figures 39 and 40 is plotted as a function of electrode current in figure 41. For both electrode polarities, the radial transport increased with increasing electrode current in an almost linear manner. The ions flowed radially outward with positive polarity, in the direction of the outward-pointing electric field, and radially inward with negative polarity, in the direction of the inward-pointing electric field.

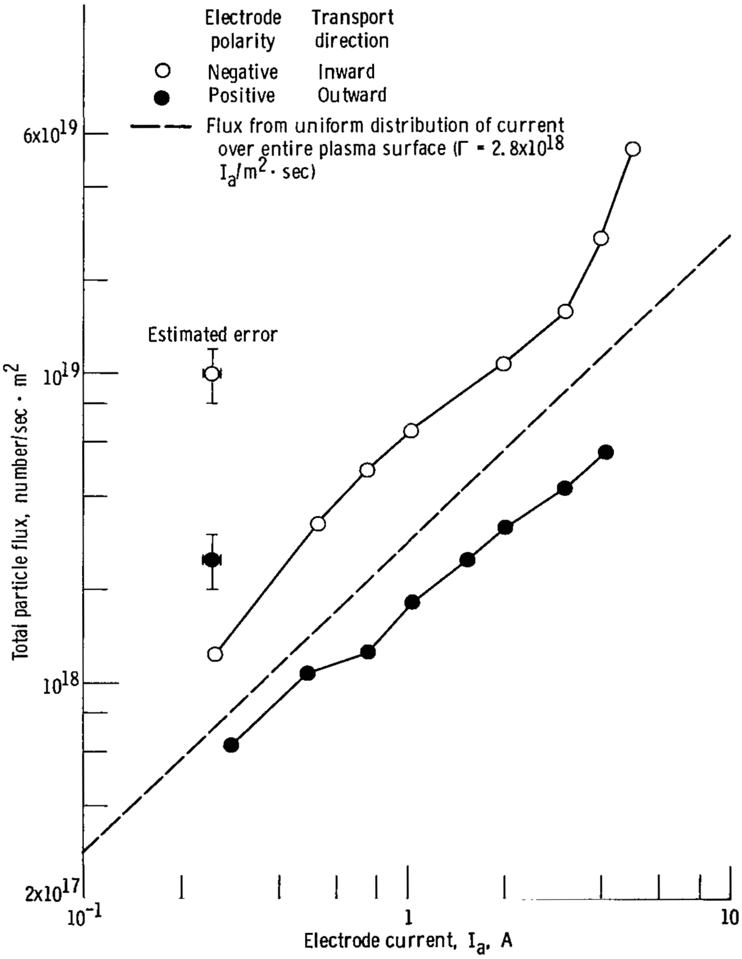

Figure 41. - Total particle flux for positive and negative electrode polarity as function of electrode current - run series AHN 1-9 and 18-25 (table V).

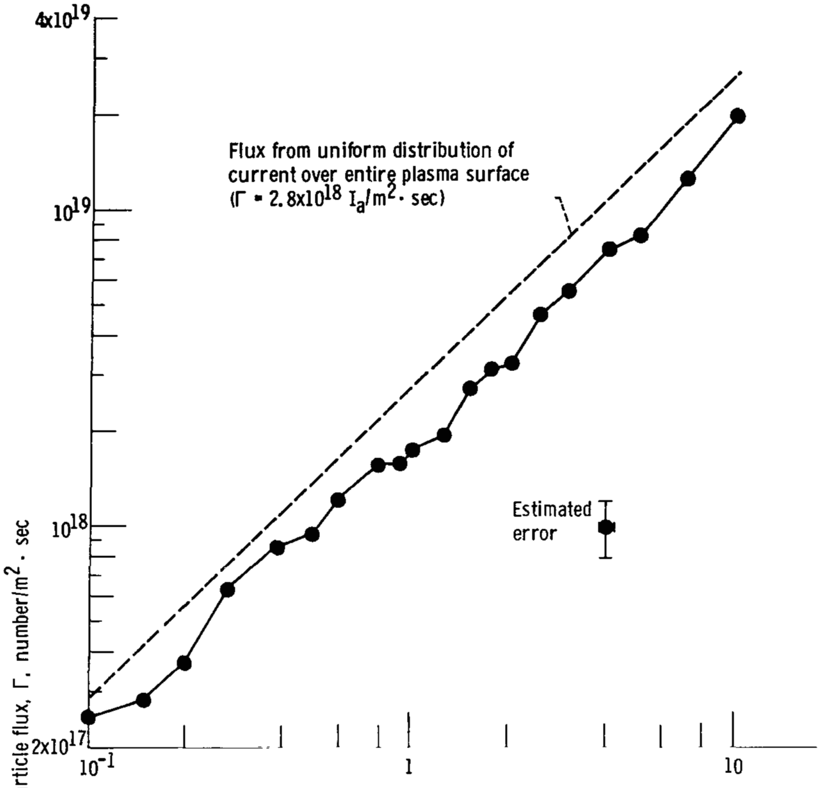

(a) Run series AJW.

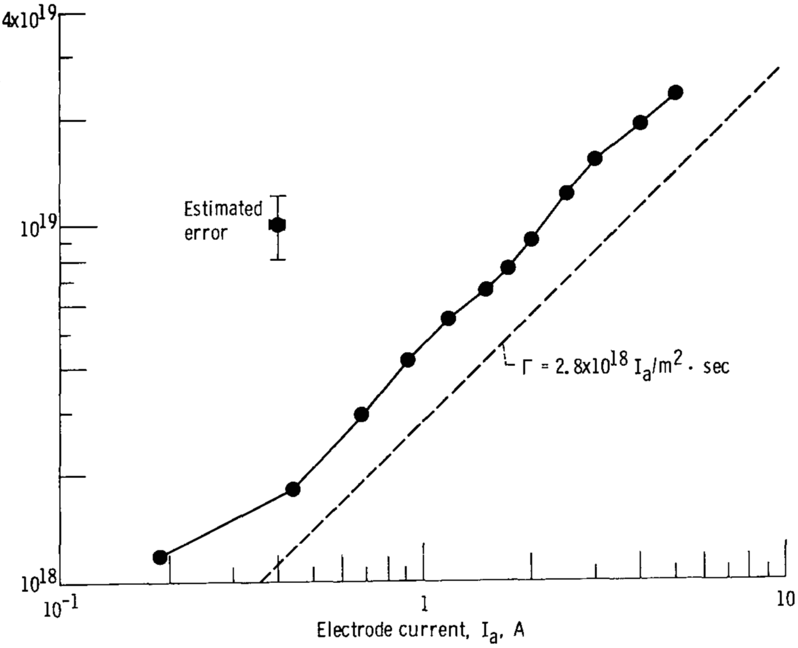

(b) Run series AKA.

Figure 42. - Total outward particle flux as function of electrode current - run series AJW and AKA (table IV).

The radial ion flux was measured at the standard radial zero position for the first and third experimental runs in table IV. These two runs had positive polarity, with a radially outward-pointing ion flux. Their transport rates were plotted in figure 42(a) for the stainless-steel tube electrode, and in figure 42(b) for the standard D-shaped electrode. The electrode current varied by a factor of 100 in the first case and by a factor of 25 in the second. It is notable that in both cases the radial transport rate was linearly proportional to the electrode current. This implies that the fluctuation-induced radial transport measured by this diagnostic technique was the dominant radial transport process in this plasma over the entire range of electrode currents for which data were taken. If fluctuation-induced transport made a minor contribution to the total electrode current, and hence to the total particle losses from the plasma, the electrode current would vary independently of the radial ion flux.

Another significant observation was that the ion fluxes were in good quantitative agreement with the observed electrode currents. The relationship between the electrode current and the particle flux can be written as

$$I_a = e\Gamma A_P \tag{5}$$

where $A_P$ is the surface area of the plasma at the probe radius, which for the bumpy-torus plasma was approximately 2.2 square meters. The dashed lines in figures 41 and 42 represent equation (5). Thus, if the plasma lost ions uniformly over its entire surface, the dashed lines should give the outward particle flux. The fact that the observed particle fluxes were within about a factor of 1.5 of this theoretical straight line is remarkable and indicates that there was good quantitative as well as qualitative agreement between the particle fluxes and the total electrode current flowing from the plasma to the power supply. The small quantitative discrepancy that is evident can be attributed to the possibility that 2.2 square meters was not the correct surface area at the probe location for both of these electrode geometries, or, more likely, that the outward flux was not uniform over the entire plasma surface and was different in the region of higher electric fields where the plasma necks down and goes through the inner bores of the superconducting magnets.

## Dependence on Weak Vertical Magnetic Field

The particle confinement time and average electron number density in this plasma were extraordinarily sensitive to a weak vertical magnetic field, about one-thousandth of the toroidal magnetic field, applied to the confinement volume. These vertical fields were generated by two coils wrapped around the exterior of the vacuum tank and ranged over ±0.01 tesla (positive is upward). The effect of this vertical magnetic field on the average electron number density is shown in figure 43(a). When these data were taken, electrode voltage, deuterium background pressure, maximum magnetic field, and other independent variables were held constant at the second set of operating conditions in table V. There was a region between 2 and 3.2 milliteslas in which no plasma could be generated. The effect of vertical magnetic field on the ion flux at the probe location is shown in figure 43(b). The vertical magnetic fields that resulted in the highest inward

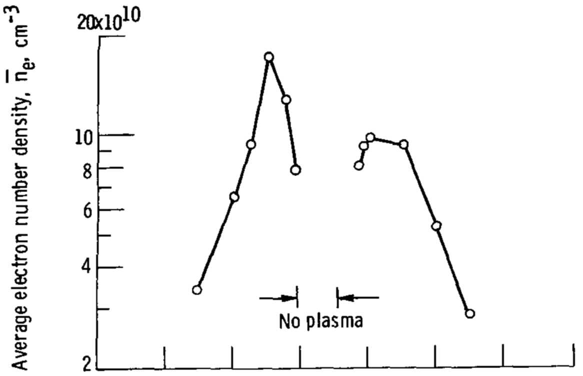

(a) Average electron number density.

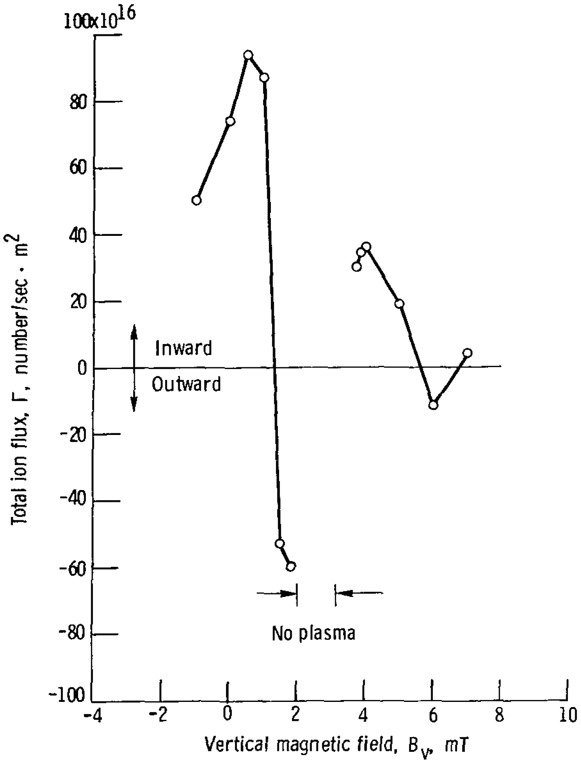

(b) Total ion flux.

Figure 43. - Effect of weak, vertical magnetic field on confinement - run series AHF 13-24 (table V).

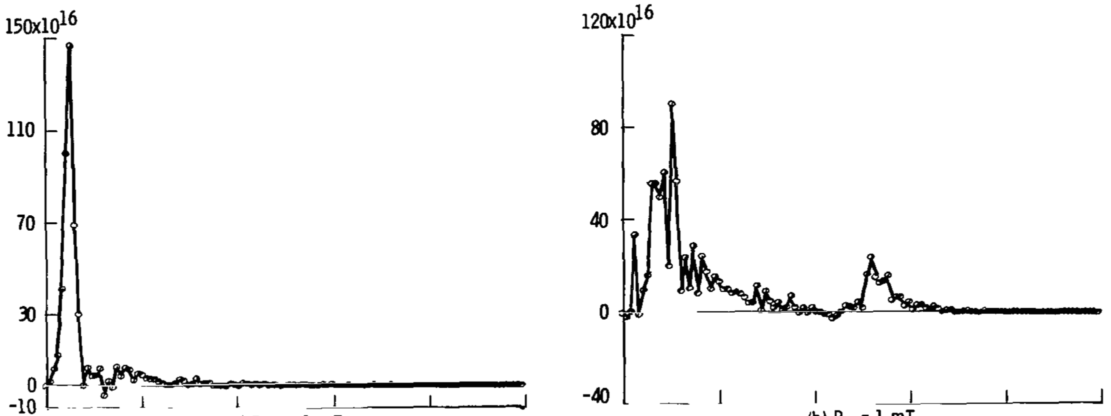

(a) $B_V$ = -1 mT.

(b) $B_V$ = 1 mT.

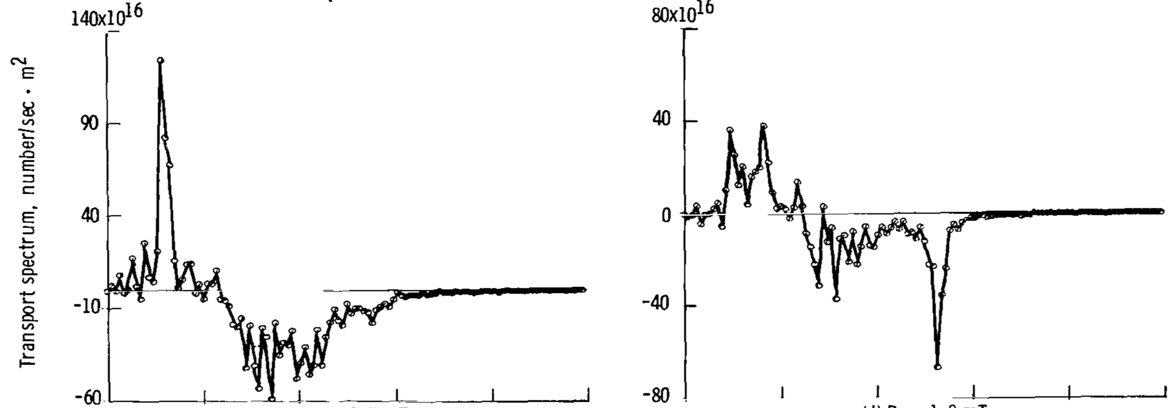

(c) $B_V$ = 1.5 mT.

(d) $B_V$ = 1.8 mT.

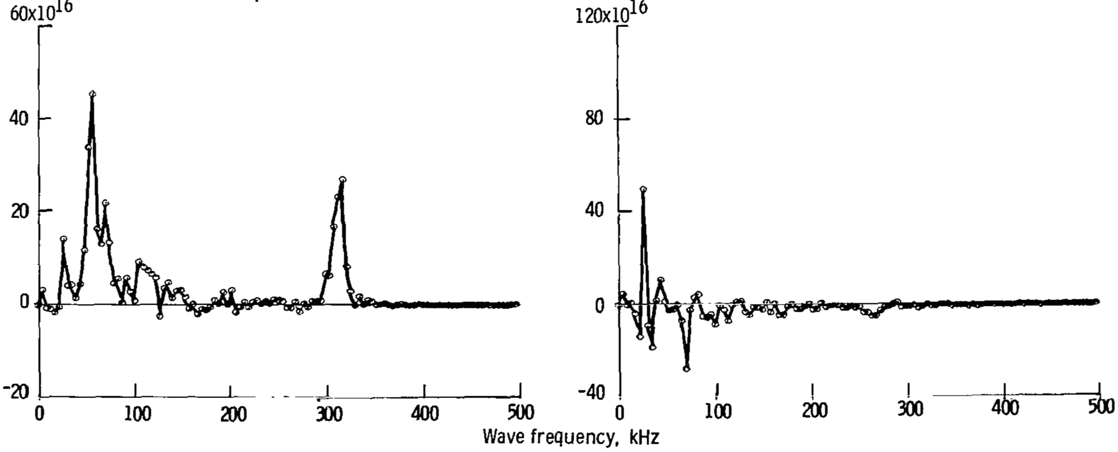

(e) $B_V$ = 4 mT.

(f) $B_V$ = 6 mT.

Figure 44. - Radial transport spectra for six vertical magnetic fields $B_V$.

transport of ions corresponded to the highest electron number densities, and the vertical magnetic fields that resulted in the highest outward transport of ions corresponded to the lowest electron number densities, where the plasma is approaching extinction. The transport spectral density function for six values of the vertical magnetic field plotted in figure 43 is shown in figure 44 in absolute units for frequencies up to 500 kilohertz. When the vertical magnetic field was -1 millitesla, the radially inward transport was dominated by a large peak at 20 kilohertz. As the vertical magnetic field was increased to 1 millitesla, the inward transport was found over a broad, almost turbulent, spectrum from 0 to 150 kilohertz, and a peak of inward transport also appeared at about 250 kilohertz. As the vertical magnetic field was increased to 1.5 and 1.8 milliteslas, which are near the region of plasma extinction in figure 43, the transport near 250 kilohertz reversed direction and flowed radially outward. The area under the curve in this portion of the spectrum dominated the total transport and resulted in net outward transport of ions. Beyond the region of plasma quenching from 2 to 3.2 milliteslas, two major peaks at a vertical field of 4 milliteslas dominated the transport and were radially inward. As the vertical magnetic field was further increased to 6 milliteslas, the importance of the high-frequency peak diminished and the total transport rate became much smaller in magnitude.

Spectral plots like those in figures 11 to 14 show that the direction of transport associated with the peak near 250 kilohertz in figure 44 was reversed because the phase angle between density and potential fluctuations $\alpha_{n\varphi}$ changed sign as the vertical magnetic field was changed from run to run. As is indicated by equation (3), a change in sign of the phase angle $\alpha_{n\varphi}$ results in a change in the direction of fluctuation-induced transport.

## SINK MODEL OF CONFINEMENT

### Calculation of Particle Confinement Time

A series of calorimetric and other investigations (ref. 28) showed that no parasitic currents were flowing outside the plasma volume or directly along the magnetic field lines that might short circuit the power supply to ground, and that no ambipolar currents were flowing to either electrode. The latter condition implies that the cathode did not emit electrons and that all ion-electron pairs were created by volume ionization within the bulk of the plasma. The calorimetric measurements showed that parasitic or ambipolar currents contributed no more than 1 percent to the current flowing to the power supply (ref. 28).

Under these conditions, the direct current flowing to the power supply was a measure of the charge losses of the plasma, with all ions flowing to the cathodes and all electrons flowing to the anodes. The total power supply current to this steady-state plasma can be written

$$I_a = \frac{\bar{n}_e e V_P'}{\tau_p} \quad \text{amperes} \tag{6}$$

where $\bar{n}_e$ is the average number density measured by the microwave interferometer, e is the electronic charge, $V_P'$ is the plasma volume (82 liters for this plasma), and $\tau_p$ is the overall particle confinement time. Equation (6) can be rearranged to yield

$$\tau_p = \frac{\bar{n}_e e V_P'}{I_a} \quad \text{seconds} \tag{7}$$

so that the particle confinement time can be calculated from the average number density and the direct current flowing to the power supply.

## Scaling of Particle Confinement Time

The total power supply current $I_a$ can be divided into two parts: a sheath current $I_s$ due to the flow of ions across the electrode sheaths that separate the plasma from the electrodes, and an "intrinsic" current $I_{in}$ arising from ion losses to the electrode (or to the electrode supports) that are associated with all other physical processes. The intrinsic losses may include ions intercepted by the electrodes or the electrode supports outside the plasma volume as a result of static $E/B$ drifts, $\nabla B$ drifts, or instability-related radial transport. The total current is

$$I_a = I_s + I_{in} \tag{8}$$

The sheath current $I_s$ carried by ions that flow across the electrode sheaths of total area A with current density $J_s$ can be written

$$I_s = J_s A = \frac{e\bar{n}_e V_P'}{\tau_s} \tag{9}$$

where $\tau_s$ is the particle confinement time resulting from the sheath current $I_s$. The ion current density in the sheath can be written

$$J_s = \frac{1}{4} e n_s v_i \tag{10}$$

where $n_s$ is the ion number density at the outer boundary of the sheath and $v_i$ is the thermal velocity of the ions. If each of N identical electrodes surrounding the plasma has associated with it a sheath of area $A_s$, then $A = NA_s$ and the particle confinement time associated with the electrodes can be obtained by combining equations (9) and (10).

$$\tau_s = \frac{4\bar{n}_e V_P'}{n_s v_i A} = \frac{4\bar{n}_e V_P'}{N n_s v_i A_s} = \frac{\tau_o}{N} \tag{11}$$

where $\tau_o$ is the particle confinement time resulting from a single electrode:

$$\tau_o = \frac{4\bar{n}_e V_P'}{n_s v_i A_s} \tag{12}$$

The scaling implied by equations (11) and (12) states that if the particle confinement can be optimized so that $I_{in}$ is negligible and the dominant ion loss is through the electrode sheaths, the particle confinement time will be inversely proportional to the number of identical electrodes. It also follows from equation (12) that the particle confinement time resulting from the irreducible minimum of one electrode required to bias the plasma is proportional to plasma volume and inversely proportional to the area of the sheath separating the electrode from the plasma. The particle confinement time does not depend on the electron kinetic temperature, the electrode voltage, or the magnetic field.

The particle confinement time $\tau_{in}$ associated with the ion losses included in the intrinsic current $I_{in}$ can be written

$$I_{in} = \frac{e\bar{n}_e V_P'}{\tau_{in}} \tag{13}$$

If equations (6), (8), (9), and (13) are combined, the particle confinement time $\tau_p$ is

$$\frac{1}{\tau_p} = \frac{1}{\tau_s} + \frac{1}{\tau_{in}} \tag{14}$$

After the rightmost member of equation (11) is substituted into equation (14), the particle confinement time can be written as

$$\tau_p = \frac{\tau_o \tau_{in}}{\tau_o + N\tau_{in}} \tag{15}$$

Equation (15) predicts that the particle confinement time will improve if the number of electrodes is reduced.

Equation (6) can be solved for the average electron number density in the plasma. Substituting equation (15) for the particle confinement time yields

$$\bar{n}_e = \frac{I_a \tau_p}{eV_P} = \frac{I_a \tau_o \tau_{in}}{eV_P (\tau_o + N\tau_{in})} \tag{16}$$

The average electron number density is directly proportional to the electrode current and inversely proportional to the number of electrodes for those cases in which the interception rate of the electrodes dominates the intrinsic losses, $\tau_{in} >> \tau_o$.

TABLE VI. - OPERATING CONDITIONS FOR SINK MODEL TESTS

[Electrode polarity, negative; electrode voltage, variable; electrode current, variable; electric field direction, inward.]

| Operating condition | Experimental run series | | | |
|---|---|---|---|---|
| | AGY, AGZ, AHA, AHB | AGV, AGV, AGW | AJL | AJJ |
| Number of electrodes, N | Variable | Variable | 1 | 1 |
| Type of electrode | Standard D | Standard D | Stainless-steel rod | Stainless-steel rod |
| Electrode location | Variable | Variable | Sector 5 | Sector 5 |
| Background neutral-gas pressure, $p_0$, particles/cm$^3$ (torr) | $1.8\times10^{12}$ $(5.3\times10^{-5})$ | $1.8\times10^{12}$ $(5.3\times10^{-5})$ | $2.5\times10^{12}$ $(7.5\times10^{-5})$ | $2.6\times10^{12}$ $(7.6\times10^{-5})$ |

## Experimental Evidence for Sink Model

A series of measurements were carried out to test the sink model of confinement, under the conditions specified in table VI. These consisted of measurements of the average electron number density as a function of the electrode current, for several combinations of negatively biased electrodes. Figures 45 and 46 show the particle confinement time and average electron number density as functions of electrode current for 12, 9, 6, 4, 3, and 2 electrodes, respectively. The nine electrodes were arranged in three triads with missing electrodes 120° apart; the six electrodes were located in alternate sectors; the four electrodes were arranged in two symmetric pairs in sectors 5 and 6 and 11 and 12; the three electrodes were located in sectors 120° apart; and the two electrodes were placed in sectors 5 and 6.

The arrows on the ordinates in figures 45 and 46 were drawn on the assumption that sheath losses are the sole particle-loss mechanism and that a particle confinement time $\tau_o$ of 4.9 milliseconds would result if the plasma could be generated with a single elec-

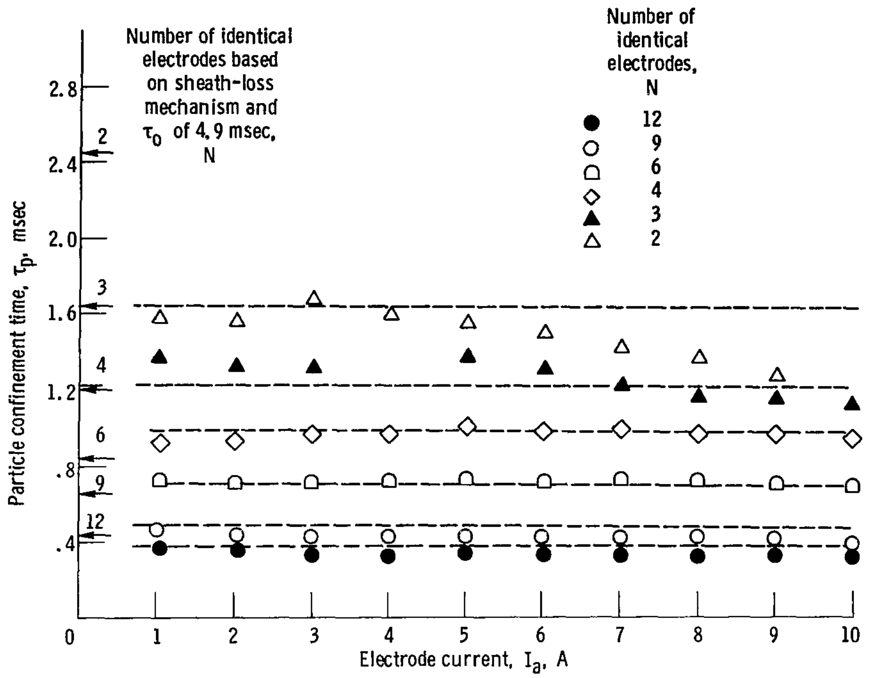

Figure 45. - Particle confinement time as function of electrode current for various numbers of identical electrodes surrounding plasma volume - run series AGY, AGZ, AHA, and AHB (table VI).

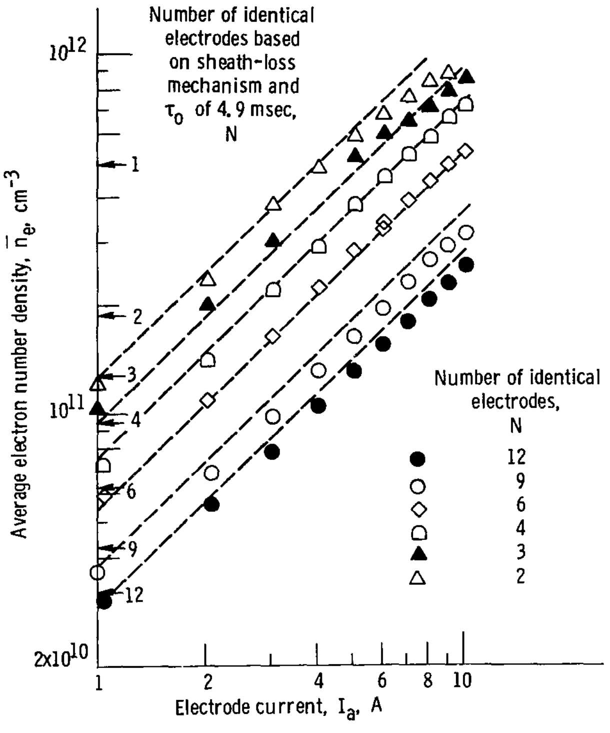

Figure 46. - Average electron number density as function of electrode current - run series AGY, AGZ, AHA, and AHB (table VI).

trode. As is evident, the experimental data lie somewhat below the arrows, suggesting that an additional, "intrinsic" loss process occurs in this plasma. The dashed lines in figures 45 and 46 are based on the particle confinement time given by equation (15), with N denoting the appropriate number of electrode rings. The best-fitting intrinsic confinement time for these data was 5.0 milliseconds. In another similar series of measurements made under more nearly optimized operating conditions, the intrinsic confinement time was 12.4 milliseconds.

The data of figure 47 tend to confirm the volume scaling predicted by equation (11). This equation states that if intrinsic losses are negligible, the particle confinement time will be proportional to the specific volume (i.e., the volume of plasma per electrode). The radial profiles of number density did not change as the number of electrodes was changed, so the ratio $\bar{n}_e/n_s$ in equation (11) should remain constant. The sheath area per electrode $A_s$ and the ion kinetic temperature $\mathscr{T}_i$ are known from previous work (refs. 27 and 28) not to depend on the number of electrodes. The solid line in figure 47 is the predicted particle confinement time for no intrinsic losses, a single electrode, and a single-electrode particle confinement time $\tau_0$ of 4.9 milliseconds. The open data

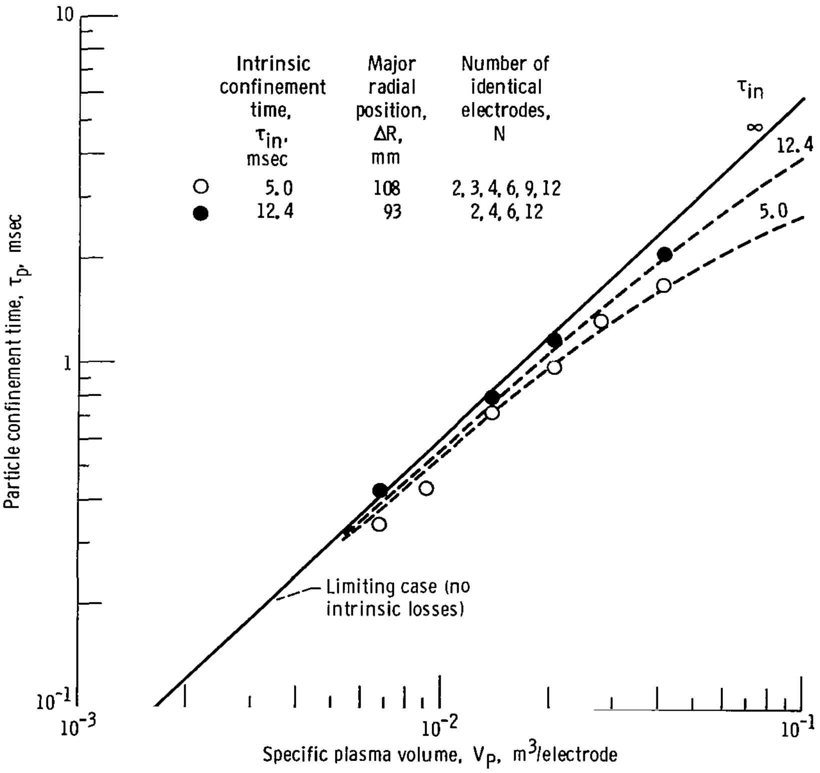

Figure 47. - Particle confinement time as function of specific plasma volume - run series AGY, AGZ, AHA, AHB, AGU, AGV, and AGW (table VI). Single-electrode confinement time, $\tau_0$, 4.9 msec.

points in figure 47 are the same data plotted in figures 45 and 46, with 2, 3, 4, 6, 9, and 12 electrodes and an intrinsic confinement time $\tau_{in}$ of 5.0 milliseconds. The solid data points represent nearly optimum confinement ($\tau_{in}$ of 12.4 msec) with 2, 4, 6, and 12 electrodes. The dashed lines represent the particle confinement times $\tau_p$ predicted by equation (15) for a $\tau_0$ of 4.9 milliseconds and the values of $\tau_{in}$ and $\Delta R$ shown in the key. The particle confinement time scales with the plasma volume per electrode as predicted by equation (11), with the departures of the experimental data from a 45° direct proportionality being consistent with intrinsic losses unrelated to processes in the electrode sheath.

A further test of the scaling law of equation (11) can be made by varying the electrode cross-section. If a toroidal plasma has a mean minor radius a and a major radius R, the toroidal volume is

$$V_p' = 2\pi^2 a^2 R \tag{17}$$

If an electrode encircles the plasma minor circumference and if the sheath has a diameter $d_s$, the sheath area is

$$A_s = 2\pi^2 a d_s \tag{18}$$

Substituting these two expressions into equation (11) yields

$$\tau_s = \frac{4\bar{n}_e aR}{N n_s v_i d_s} \tag{19}$$

When all other factors are held constant, the particle confinement time is inversely proportional to the sheath minor diameter.

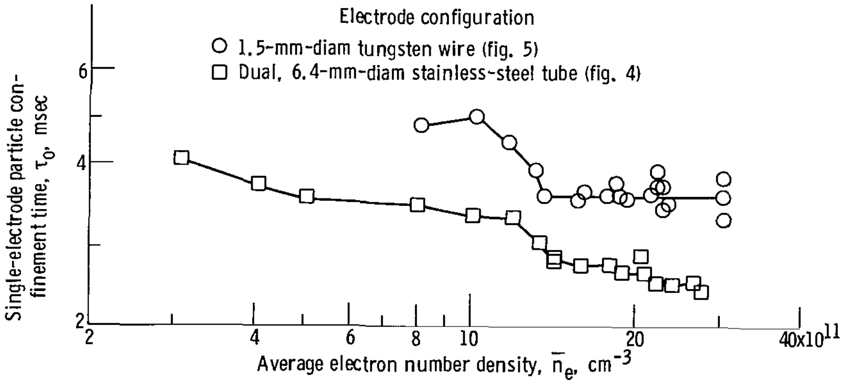

Figure 48. - Particle confinement time as function of average electron number density for two electrode configurations - run series AJL and AJJ (table VI).

Figure 48 shows the particle confinement time as a function of the plasma electron number density for single electrodes with two different cross-sections. The data represented by the open circles were taken with the tungsten-wire electrode (fig. 5), and the data represented by the open squares were taken with the dual, stainless-steel tube electrode (fig. 4). From visual observations the sheaths appeared to have a radial thickness of about 6 millimeters. The smaller diameter, tungsten-wire electrode gives particle confinement times about 1.7 times longer than those of the stainless-steel electrode, as is consistent with the functional dependence predicted by equation (19).

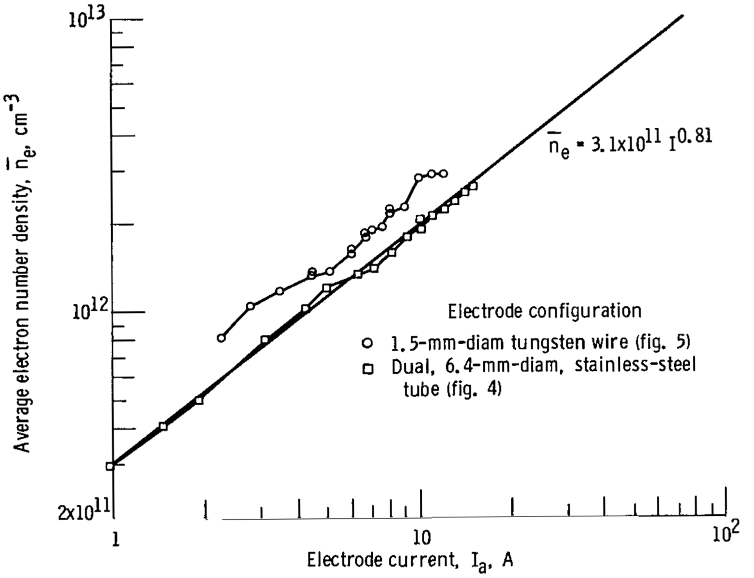

Figure 49. - Average electron number density as function of electrode current for two electrode configurations - run series AJL and AJJ (table VI).

Figure 49 also shows results of the third experimental run in table VI. These data show the enhancement of plasma density, at a given electrode current, that results from the improved confinement of a smaller diameter electrode.

Finally, equation (11) predicts that the particle confinement time is independent of magnetic field. This has been confirmed in reference 26, where, under poorly optimized operating conditions, it was shown that the confinement time was approximately independent of magnetic field over a factor-of-10 variation in the magnetic field strength. These data were replotted in figure 50. The data are consistent with a particle confinement time independent of magnetic field strength and are inconsistent with Bohm or classical scaling, where the functional dependence on magnetic field would be proportional to B or $B^2$, respectively.

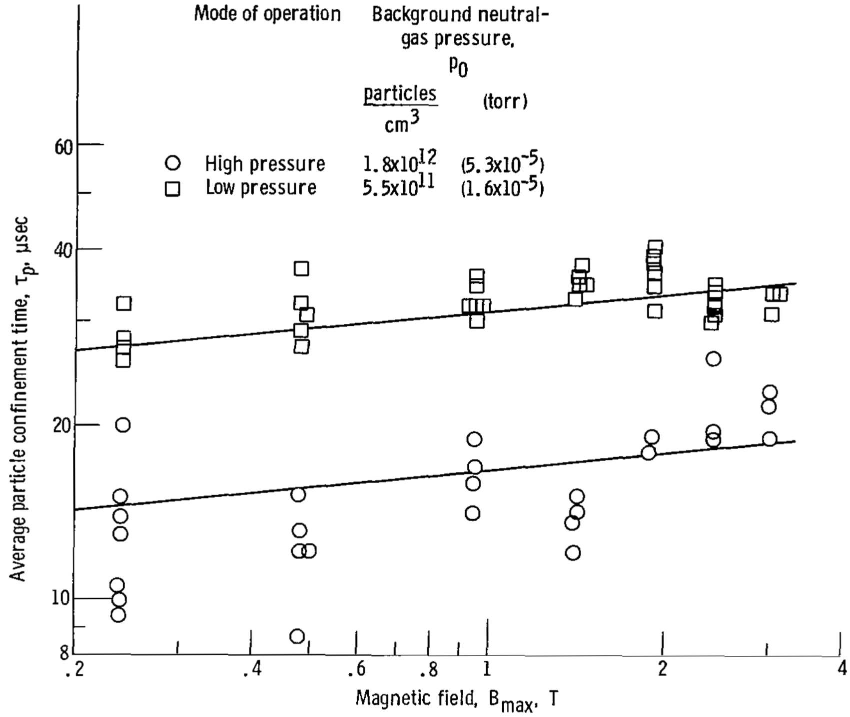

Figure 50. - Particle confinement time as function of magnetic field strength, for off-optimum operating conditions that resulted in poor confinement.

## DISCUSSION

### Absence of Magnetohydrodynamic Instabilities

Plasmas that are confined only by static magnetic fields are subject to a variety of magnetohydrodynamic (MHD) instabilities, which arise from reservoirs of free energy associated with the confined plasma. In the ELMO bumpy-torus configuration, low-frequency, long-wavelength MHD instabilities pose the greatest threat to confinement (refs. 43 and 44). The most severe of these are driven by centrifugal forces associated with motion of the particles along the curved magnetic field lines in the midplanes where the field lines bow outward and also by the centrifugal forces associated with the drift of particles about the magnetic axis. In the ELMO experiment, MHD modes are stabilized by the perturbed magnetic field resulting from relativistic, high-beta electron rings that are trapped in the midplane of each sector.

The radial electric fields characteristic of the NASA Lewis bumpy-torus experiment exert forces on individual particles that dominate the relatively weak centrifugal or "gravitational" forces responsible for the usual MHD instabilities. To illustrate, visualize an ion moving along a magnetic field line in one of the bumps of the torus. There will be an outward (centrifugal) force on the ion, the magnitude of which is given by

$$F_C = \frac{mv^2}{R_c} \tag{20}$$

where the radius of curvature of the magnetic field line is approximated by the mean radius of the coils $R_c$ that generate the toroidal magnetic field. If a radially inward-pointing electric field is applied to the plasma, the charged particle will see a force equal to

$$F_E = eE_r \tag{21}$$

The electric field forces on individual particles will dominate the centrifugal forces when the ratio of equation (21) to equation (20) is greater than unity:

$$\gamma = \frac{F_E}{F_C} = \frac{R_c E_r e}{mv^2} = \frac{R_c E_r}{3\mathscr{T}_i} \tag{22}$$

If we substitute a radius of curvature equal to the mean radius of the bumpy-torus coils of the present experiment ($R_c = 13$ cm), equation (22) can be written

$$\gamma = 4.33 \frac{E_r}{\mathscr{T}_i} \tag{23}$$

where $E_r$ is in volts per centimeter and $\mathscr{T}_i$ is in electron volts.

Figure 51 shows the combinations of ion kinetic temperature and electric fields that result in equality between the electric field and centrifugal forces for the bumpy-torus plasma. The present experiment operated in the shaded region, for which the electric field forces dominated the weak centrifugal forces that drive the MHD instabilities. For this reason, MHD instabilities should not arise. The experimental observations reported herein are consistent with this expectation. If such instabilities were present, they would appear as a prominent, coherent peak in the potential and/or density fluctuation spectra, such as those in figures 11 to 14. Under many operating conditions, however, the fluctuation spectra are quite turbulent, and no such prominent peaks are evident. The peaks that have been observed, such as those in figure 14, are due to E/B drift and the rotating spokes that resulted from the diocotron instability. The absence of low-frequency MHD instabilities in this plasma is also consistent with the requirements of the Bohr - Van Leeuwen theorem (ref. 9), which states that a state of kinetic equilibrium can be achieved if the internal reservoirs of free energy are minimized. The turbulent na-

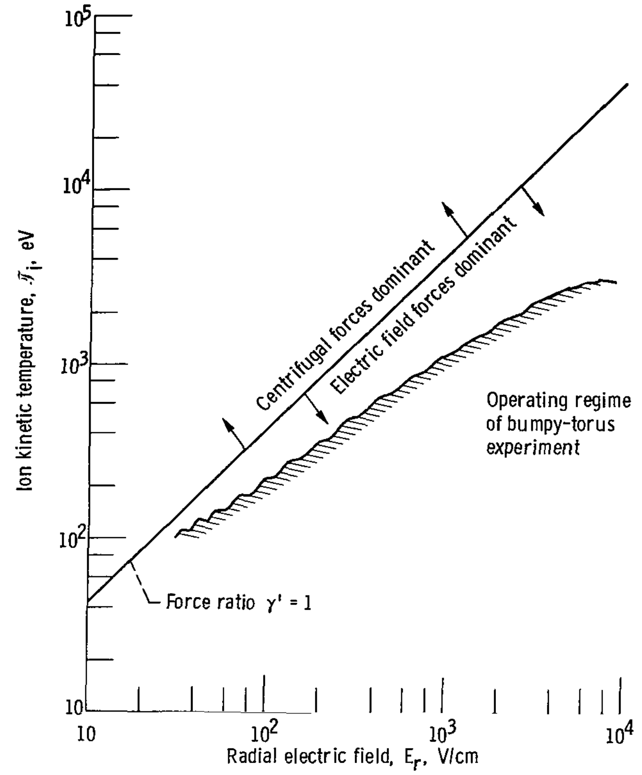

Figure 51. - Ion kinetic temperature as function of radial electric field. (Bumpy-torus experiment operates in region where electric field forces dominate the centrifugal forces that drive MHD instabilities.)

ture of the fluctuations and their Gaussian amplitude statistics therefore are consistent with the absence of MHD instabilities in this plasma.

## Radial Electric Fields

The radial profiles of floating potential presented in figure 26 reveal radial electric fields that varied from less than 10 volts per centimeter, outside the visible plasma boundary, to as high as 135 volts per centimeter at the maximum inward position to which the probes could be inserted. The electric fields increased with increasing radial penetration, at least halfway to the axis of the plasma. The magnitude of these radial electric fields was far greater than could be explained by simple Debye length considerations; it was also greater than would be expected on the basis of ambipolar phenomena.

In several instances, the radial profile of floating potential can be approximated by an exponential dependence on radius, which implies an electric field radial dependence of the form

$$E(r) = E_0 e^{-r/\lambda'} \tag{24}$$

where $\lambda'$ is the scale length of the floating potential.

## Parametric Variations

The effects of the various electrode shapes and configurations that were investigated are consistent with the scaling law of equation (19). When the weak, vertical magnetic field was optimized, the number density and particle confinement times improved as the number of identical electrodes was reduced, as is consistent with the data in figures 45 and 46. The data in figures 28 to 31 indicate not only that negative polarity on the electrodes confines particles much better than positive polarity, but also that a tubular water-cooled electrode passing across the minor diameter of the plasma results in slightly higher densities and confinement times than the D-shaped electrode shown in figure 3. It was also more difficult to optimize confinement for the D-shaped electrode, a consequence of which was the dependence of the density and confinement time on the various parameters investigated.

Consistent with the scaling law of equation (19), smaller diameter electrodes resulted in higher number densities and longer particle confinement times than did larger diameter electrodes. The relevant diameter appearing in equation (19) is apparently the diameter of the sheath and not that of the electrode itself. Particle confinement times of 6 milliseconds and number densities of $3.2\times10^{12}$ particles per cubic centimeter were achieved with an electrode consisting of a single 1.5-millimeter-diameter tungsten wire across the minor diameter of the plasma (fig. 5). This small-diameter electrode had to be cooled by radiation but was not hot enough to be electron emitting. Its current-voltage characteristic was far below that of the water-cooled, stainless-steel tube electrode with which it is compared in figures 48 and 49. Figure 52 shows the current-voltage characteristics of the plasma for these two electrodes. The very low voltages characteristic of the thin tungsten electrode are undesirable in that they imply relatively small electric fields and low ion kinetic temperatures.

Figure 53 shows the effect on plasma impedance of varying the number of identical electrode rings. These data were taken simultaneously with the data in figures 45 and 46. For a large number of electrodes, the density-voltage characteristic of the plasma was quite steep and the plasma impedance was so low that only about 300 volts could be applied. As the number of identical electrodes was reduced, the plasma impedance increased - until finally, for two electrodes, between 2 and 3 kilovolts could be applied.

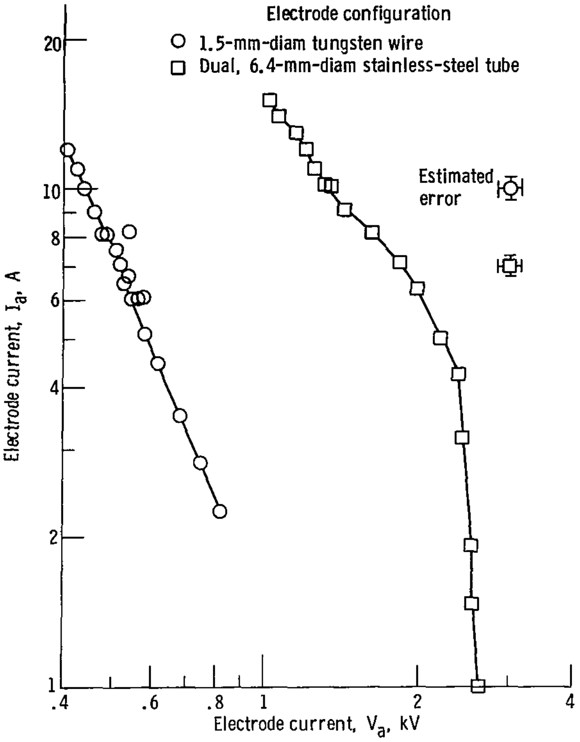

Figure 52. - Current-voltage characteristics for two electrode configurations - run series AJL and AJJ (table VI).

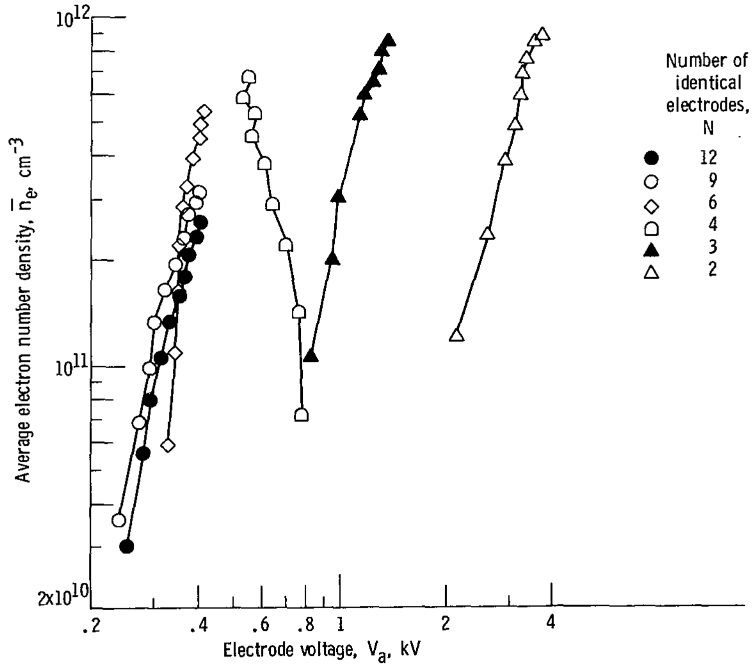

Figure 53. - Average electron number density as function of electrode voltage for various numbers of identical electrode rings - run series AGY, AGZ, AHA, and AHB (table VI).

### Radial Transport

The transport of charged particles along an electric field in a cross-field geometry can occur in at least three ways. A collisionless mechanism for transport along the electric field has been described by Cole (ref. 15), who showed that if the electric field has a strong spatial gradient along its own direction, charged particles will flow in the direction of the electric field if the gradient in the electric field meets the following criterion:

$$\frac{eB^2}{m} - \nabla E < 0 \tag{25}$$

By making use of the exponential falloff of potential with radius that is sometimes observed and the resulting equation (24), equation (25) can be written

$$\frac{eB^2}{m} < \frac{E_r}{\lambda'} \tag{26}$$

where $\lambda'$ is the radial scale length of the potential and is typically between 1 and 2 centimeters in this experiment. Because the conditions specified by inequality (26) are not satisfied in these experiments by approximately a factor of 10, the collisionless mechanism of Cole cannot be responsible for the radial transport of ions. In previous work with higher applied potentials, radial electric fields in excess of 1 kilovolt per centimeter have been observed (ref. 27), and under such conditions the mechanism of Cole could begin to come into play.

A collisional mechanism for transport of particles along the electric field, the Pedersen current, has been discussed by Alfven and Falthammar (ref. 14). The Pedersen current is given by

$$\bar{j}_\perp = \frac{e^2 n\tau}{m} \frac{1}{1 + \omega^2 \tau'^2} \vec{E}_r \tag{27}$$

where $\omega$ is the gyrofrequency and $\tau'$ is the relevant collision time. The Pedersen current is in the direction of the electric field and requires collisions in order to allow the particles to fall toward the bottom of their respective electrostatic potential wells. Experimental data such as that shown in figures 41 and 42 indicate that the ion transport was in the direction of the radial electric field in this plasma, as is consistent with the Pedersen mechanism. What is not clear is what kind of collisional processes could be responsible for the Pedersen currents. Figure 35 shows that for the stainless-steel tube electrode, the average number density and particle confinement time were independent of the background neutral gas pressure over a factor of 3 in the latter quantity. It is clear from equation (27) that this could not be the case if the transport mechanism depended on charged particle - neutral collisions. The independence of confinement time and number density from background gas pressure appears to rule out collisions with neutrals as a collisional mechanism for the Pedersen currents.

Another collisional mechanism to consider is binary collisions between charged particles. Although the ion-electron equilibration time becomes comparable to the particle confinement time at densities of about $10^{12}$ particles per cubic centimeter, these binary collisions are much too infrequent - at the lowest densities investigated - to provide sufficient collisions for radial transport. For example, in figure 32 the particle confinement time is plotted as a function of the average electron number density. When conditions were properly optimized, the particle confinement time was virtually independent of the average number density over a factor of 50 or more in that quantity. If collisions between charged particles were affecting the transport rate, the particle confinement time would probably not remain independent of the charged-particle number density. In addition, the data in figure 32 extend from $10^{10}$ to $10^{12}$ particles per cubic centimeter. The binary collision times at the lower end of this range are too long to account for the observed radial transport.

The experimental data therefore rule out collisional Pedersen currents and the mechanism of Cole as explanations of the observed radial transport. The remaining mechanism is fluctuation-induced transport, which is consistent with the observations of radial ion fluxes made with the transport diagnostic. The probe assembly (fig. 6) was located at the region of weakest magnetic field and most unfavorable field curvature (for MHD instabilities) in the entire confinement volume. On these grounds, the transport at this point should probably be higher than that at a typical point on the plasma surface. Apparently this was not the case. Figures 41 and 42 demonstrate that the particle flux rate near the probe sampling position, when multiplied by the surface area of the plasma, came within a factor of 2 of accounting for the current drawn by the power supply. Transport measurements have not yet been taken at other positions in the plasma, but these results are consistent with the idea that the radial transport is approximately uniform over the plasma surface, except at the sheaths surrounding the electrodes.

Figure 43 demonstrates that both the number density and particle flux are a sensitive function of a weak, vertical magnetic field that penetrates the plasma volume. These vertical magnetic fields were about one-thousandth of the main toroidal magnetic field and 3 to 5 times the vertical magnetic field (0.3 mT) generated by the current loop in the lower liquid-helium manifold, which connects the 12 coils in series. Therefore, this current-loop field has no effect on confinement time.

Transport spectra such as those in figure 44 and their corresponding fluctuation spectra indicate that the vertical field affects the transport by changing the sign of the phase angle between the density and potential fluctuations. What this may correspond to physically is a change in the geometric structure of the rotating disturbances such that the angular separation between the density and potential maxima is altered by the weak, vertical magnetic field.

## Implications of Sink Model

The sink model of confinement describes the functional dependence of the particle confinement time in this plasma. The processes underlying this model are fundamentally different from those that exist in pure magnetic confinement devices. The latter are restricted to outward transport of the plasma only, at rates determined by some modification of classical diffusion. The use of strong inward-pointing radial electric fields in the bumpy-torus plasma admits the possibility of radially inward particle transport, against the density gradient over much of the plasma surface, by physical mechanisms such as fluctuation-induced transport. The strong electric fields that were externally imposed on this plasma were generally much higher than those to be expected from ambipolar phenomena.

The experimental data in figures 45 and 46 are consistent with the assumptions that all other ion loss processes have been minimized and that the dominant loss process in this plasma is withdrawal of ions by the negatively biased electrodes. The particle confinement time decreased as more electrodes were applied to withdraw ions from the plasma. The strong dependence of plasma density and particle confinement time on the number of identical electrodes used to bias the plasma demonstrated that confinement was dominated by physical processes associated with the individual electrodes rather than by processes that took place between the plasma and the surrounding grounded walls. The various forms of classical diffusion would be an example of the latter processes. The electron loss processes in the region between the plasma and the wall were controlled by the ion losses to the electrode in such a way that the ion and electron losses from the plasma volume were in detailed balance in the steady state.

Clearly, there is an intrinsic loss process, not related to the electrode sheaths, that results in confinement times to 12.4 milliseconds. Optimizing the intrinsic confinement time to durations longer than 12.4 milliseconds has not been possible thus far because it represents a small difference between large numbers as long as the electrode sheaths dominate plasma losses. When confinement was optimized to the extent demonstrated by the data presented, the scaling law for particle confinement time given by equation (19) was consistent with the experimental data. Figure 47 demonstrates the proportionality of the particle confinement time to the plasma volume per electrode. The departures from direct proportionality shown by the two sets of experimental data in figure 47 were due to the difficulty of eliminating the intrinsic losses with the relatively crude optimization procedure available at present. The data in figures 48 and 49 were taken for single electrodes with different cross-sectional diameters. The outside diameters of the sheath differed by about a factor of 1.5. The increase in particle confinement time for the electrode with a smaller cross-sectional diameter was consistent with the inverse scaling with sheath diameter predicted by equation (19).

The various modifications of classical diffusion appropriate for plasmas confined only by magnetic fields predicted particle confinement times that would scale as the square of the minor radius of the plasma. The scaling appropriate to the sink model of equation (11), and confirmed by the data presented, predicted confinement times that would scale as the plasma volume if a single electrode was applied to a plasma of fixed minor diameter. Equation (19) predicts that, if the minor and major diameters of a toroidal plasma were scaled up by the same factor, the particle confinement time predicted by the sink model would scale as the product of the major and minor plasma radii. It has been shown previously (ref. 27) that a single electrode will heat the ion population to kilovolt kinetic temperatures as effectively as 12 electrodes. The data presented demonstrate that particle confinement times of 5 milliseconds are possible with a single electrode.

To scale the present experiment to fusion reactor conditions for which the particle confinement time is 1 second, the intrinsic losses were negligible, and all other factors in equations (11) and (19) were constant, the plasma volume must be increased by a factor of 200, or the product aR by the same factor. If the minor diameter were kept constant and the volume increased by adding identical sectors to the toroidal array, the present 12 sectors would have to be increased to 2400, with a total volume of 16.4 cubic meters, and the toroidal major diameter would be 300 meters. If the major and minor radii were increased by the same factor with all other parameters held constant, the mean minor radius a of the 12-coil array would increase from 7 centimeters to 1 meter, the major radius R would increase from 76 centimeters to 10.7 meters, and the plasma volume would increase from 0.082 cubic meter to 212 cubic meters. It thus appears that significant particle confinement times can be obtained in plasmas of modest volumes if the scaling law of equation (11) extrapolates beyond the range of the present data, if the intrinsic losses can be made negligible, and if the electrodes can withstand the conditions in the outskirts of fusion plasmas without damage.

## CONCLUSIONS

The toroidal plasma studied in this series of investigations is subject to intense, turbulent, fluctuating electric fields superimposed on direct-current, radial electric fields. The turbulent plasma rotated about the plasma axis with a velocity appropriate to the local E/B drift velocity. This drift velocity reversed direction when the sign of the electric field was reversed. Under operating conditions that produced the highest densities and particle confinement times, the plasma was turbulent, with no coherent peaks in the spectrum of either the density or the potential fluctuations. Under other conditions, discrete rotating spokes, probably a manifestation of the diocotron instability, were superimposed on the background turbulent spectra and rose from 10 to 20 decibels above it.

The amplitude statistics of both the density and the potential fluctuations were found to be Gaussian for the most part, with near-zero skewness and a kurtosis (fourth moment) of about 3.0. The spectral index of the density and potential fluctuations ranged from 2 to 6 and did not cluster near the theoretically expected value of 5.0, regardless of whether the dispersion relation relating radian frequency and wave number was linear or not.

The radial profiles of floating potential revealed that electric fields, sometimes in excess of 100 volts per centimeter during these experiments, penetrated at least halfway to the axis of the plasma; that the electric field pointed inward when the plasma was negatively biased; and that the electric field pointed outward when the plasma was positively biased. The radial profiles of transport rate indicate that when the weak vertical magnetic field was properly optimized, the transport of ions was in the direction of the electric field and tended to increase as the probe was moved inward toward the plasma axis.

When the operating conditions were properly optimized, the particle confinement time was virtually independent of the plasma number density. Positive electrode polarity confined the plasma much less well than negative polarity, for which the electric field pointed radially inward. Particle electron number densities and confinement times were at least 5 times greater when the electric field pointed inward and resulted in radially inward ion transport.

A water-cooled electrode consisting of a vertical, stainless-steel tube through the minor diameter of the plasma resulted in longer confinement times and higher number densities than a standard D-shaped electrode surrounding the minor circumference of the plasma. In addition, the particle confinement time tended to decrease with increasing number density for the standard D-shaped electrode but was nearly independent of number density for the vertical stainless-steel tube electrode. For the tube electrode, the number density and particle confinement time were independent of background neutral gas pressure. Therefore collisions with neutrals probably did not play a role in radial transport or confinement in this plasma.

It has been shown that the magnitude of the ion flux, when multiplied by the plasma area, differed by less than a factor of 2 from the current drawn by the power supply. Therefore the radial flux of particles is probably relatively uniform over the entire plasma surface, and the probes are probably sampling a typical position insofar as the radial transport rate is concerned. The fact that the electrode current was directly proportional to the observed particle flux over nearly a factor of 100 in these quantities suggests that the fluctuation-induced radial transport mechanism dominated the transport process in this plasma.

The radial transport has been shown to depend critically on the value of a weak, vertical magnetic field applied to the confinement volume. The field must be optimized in order to assure the best possible confinement. Extreme values of this vertical magnetic field can reverse the direction of radial particle transport.

A simple model of particle confinement has been proposed in which the particle confinement time is independent of magnetic field; directly proportional to the plasma volume and electron number density; and inversely proportional to the surface area of the sheath surrounding the electrode, to the ion velocity, and to the number density at the outer surface of the electrode sheath. Direct experimental evidence has confirmed these functional dependences (except that on ion velocity, which was not measured) and has also confirmed that the particle confinement time was approximately independent of the magnetic field. It has been shown that confinement is determined by physical processes associated with the individual electrodes or their sheaths and not by transport processes occurring between the plasma and the surrounding grounded walls. This scaling law for particle confinement time, if extrapolated to the fusion reactor regime, predicts fusion reactors considerably smaller in volume than would be the case if the plasma transport were controlled by classical diffusional processes. The radial transport processes in this plasma are not diffusional in nature, and radially inward transport of ions against a density gradient has been observed.

Lewis Research Center,
National Aeronautics and Space Administration,
Cleveland, Ohio, November 2, 1978,
506-25.

# APPENDIX - SYMBOLS

| | |
|---|---|
| $A$ | area, m$^{2}$ |
| $a$ | minor plasma radius, m |
| $B$ | magnetic field strength, T |
| $d$ | diameter, m |
| $E$ | electric field strength, V/m |
| $\tilde{E}$ | fluctuating electric field, V/m |
| $e$ | electric charge, C |
| $F$ | force, N |
| $I$ | current, A |
| $J$ | current density, A/m$^{2}$ |
| $k$ | wave number, m$^{-1}$ |
| $m$ | mass, kg |
| $N$ | number of identical electrodes |
| $n$ | number density, m$^{-3}$ |
| $p$ | spectral index |
| $p_0$ | background neutral-gas pressure, particles/cm$^{3}$ (torr) |
| $R$ | major plasma radius, m |
| $r$ | radius, m |
| $T$ | transport spectral density function, number/sec$\cdot$m$^{2}$ |
| $\mathcal{T}$ | kinetic temperature, eV |
| $t$ | time, sec |
| $V$ | voltage, V |
| $V'$ | volume, m$^{3}$ |
| $v$ | particle velocity, m/sec |
| $\alpha$ | angle between density and potential, rad |
| $\Gamma$ | total particle flux, number/sec$\cdot$m$^{2}$ |
| $\gamma$ | coherence |
| $\gamma'$ | force ratio |

| | |
|---|---|
| $\theta$ | phase angle between two signals, rad |
| $\lambda$ | wavelength, m |
| $\lambda'$ | scale length, m |
| $\nu$ | frequency, Hz |
| $\sigma$ | standard deviation |
| $\tau$ | confinement time, sec |
| $\tau'$ | collision time, sec |
| $\varphi$ | potential, V |
| $\omega$ | radian frequency, rad/sec |

Subscripts:

| | |
|---|---|
| a | electrode |
| C | centrifugal |
| c | coil |
| ci | ion cyclotron |
| E | electric field |
| e | electrons |
| eo | initial electron velocity |
| f | floating |
| i | ions |
| in | intrinsic |
| $n\varphi$ | density and potential |
| o | single electrode |
| P | plasma |
| p | particle |
| r | radial |
| rms | root mean square |
| s | sheath |
| v | vertical |
| $\theta$ | azimuthal direction |
| 0 | initial value |

| | |
|---|---|
| 1 | channel 1 |
| 2 | channel 2 |
| 12 | channels 1 and 2 |
| ⊥ | perpendicular to magnetic field |

# REFERENCES

1. George, K. A.: Confining a Plasma in Steady Electric and Magnetic Fields. Nature, vol. 190, Apr. 22, 1961, p. 334.
2. Ware, A. A.; and Faulkner, J. E.: Electrostatic Plugging of Open-Ended Magnetic Containment Systems. Nucl. Fusion, vol. 9, no. 4, Dec. 1969, pp. 353-361.
3. Stansfield, B. L.; et al.: Density and Lifetime Measurements in the KEMP II Electromagnetic Trap. Can. J. Phys., vol. 54, no. 18, Sept. 1976, pp. 1856-1861.
4. Lavrentev, O. A.; Potapenko, V. A.; and Stepanenko, I. A.: Particle Lifetime in a Pulsed Electromagnetic Confinement System. Sov. Phys., Tech. Phys., vol. 21, no. 1, Jan. 1976, pp. 63-66.
5. Moir, Ralph W.; Barr, William L.; and Post, Richard F.: Experimental Results on Electrostatic Stoppering. Phys. Fluids, vol. 14, no. 11, Nov. 1971, pp. 2531-2534.
6. Nishida, Y.; Kawamata, S.; and Ishii, K.: Electrostatic Ion Confinement in a Magnetic Mirror Field. J. Phys. Soc. Jap., vol. 43, Oct. 1977, pp. 1364-1370.
7. Alexeff, I.; et al.: Understanding Turbulent Ion Heating in the Oak Ridge Mirror Machine "Burnout V." Phys. Rev. Lett., vol. 25, no. 13, Sept. 28, 1970, pp. 848-851.
8. Reinmann, J. J.; et al.: Hot Ion Plasma Heating Experiments in SUMMA. IEEE Trans. Plasma Sci., vol. PS-3, no. 1, 1975, pp. 6-14.
9. Roth, J. Reece: Plasma Stability and the Bohr - Van Leeuwen Theorem. NASA TN D-3880, 1967.
10. Kovrizhnykh, L. M.: Transport Phenomena in Toroidal Magnetic Systems. Sov. Phys. JETP., vol. 29, no. 3, Sept. 1969, pp. 475-482.
11. Kovrizhnykh, L. M.: Effect of an Electric Field on Transfer Processes in Axially Symmetric Magnetic Traps. Sov. Phys. JETP, vol. 35, no. 4, Oct. 1972, pp. 709-716.
12. Stix, Thomas H.: Some Toroidal Equilibria for Plasma under Magnetoelectric Confinement. Phys. Fluids, vol. 14, no. 3, Mar. 1971, pp. 692-701.
13. Stix, Thomas H.: Stability of a Cold Plasma under Magnetoelectric Confinement. Phys. Fluids, vol. 14, no. 3, Mar. 1971, pp. 702-712.
14. Alfven, H.; and Falthammar, Carl-Gunne: Cosmical Electrodynamics. Second ed., Oxford, Clarendon Press, 1963, p. 181.

15. Cole, K. D.: Effects of Crossed Magnetic and (Spatially Dependent) Electric Fields on Charged Particle Motion. Planet Space Sci., vol. 24, no. 5, 1976, pp. 515-518.

16. Gibson, G.; Jordan, W. C.; and Lauer, E. J.: Bumpy Torus. Phys. Rev. Lett., vol. 4, no. 5, Mar. 1, 1960, pp. 217-219.

17. Gibson, G.; et al.: Guiding Center Motion and Plasma Behavior in the Bumpy Torus. Phys. Fluids, vol. 7, no. 2, Apr. 1964, pp. 548-557.

18. Geller, R.: A Pulsed Toroidal P.I.G. Discharge. Appl. Phys. Lett., vol. 2, no. 11, June 1, 1963, pp. 218-219.

19. Geller, R.: Experimental Results of a Bumpy Torus Discharge. Phys. Rev. Lett., vol. 10, no. 11, June 1, 1963, pp. 463-465.

20. Fanchenko, D. S.; et al.: Turbulent Plasma Heating in a Torus. Phys. Rev. Lett., vol. 21, no. 12, Sept. 1968, pp. 789-791.

21. Dandl, R. A.; et al.: Plasma Confinement and Heating in the ELMO Bumpy Torus. Plasma Physics and Controlled Nuclear Fusion Research 1974. Vol. 2. International Atomic Energy Agency (Vienna), 1975, pp. 141-149.

22. Roth, J. R.: Origin of Hot Ions Observed in a Modified Penning Discharge. Phys. Fluids, vol. 16, no. 2, Feb. 1973, pp. 231-236.

23. Roth, J. R.: Hot Ion Production in a Modified Penning Discharge. IEEE Trans. Plasma Sci., vol. PS-1, no. 1, Mar. 1973, pp. 34-45.

24. Roth, J. R.: Energy Distribution Functions of Kilovolt Ions in a Modified Penning Discharge. Plasma Phys., vol. 15, no. 10, Oct. 1973, pp. 995-1005.

25. Roth, J. R.: Experimental Study of Spectral Index, Mode Coupling, and Energy Cascading in a Turbulent, Hot-Ion Plasma, Phys. Fluids, vol. 14, no. 10, Oct. 1971, pp. 2193-2202.

26. Roth, J. R.; Gerdin, G. A.; and Richardson, R. W.: Characteristics of the NASA Lewis Bumpy Torus Plasma Generated with Positive Applied Potentials. IEEE Trans. Plasma Sci., vol. PS-4, no. 3, Sept. 1976, pp. 166-176. (Also NASA TN D-8114, 1976.)

27. Roth, J. Reece; and Gerdin, Glenn A.: Characteristics of the NASA Lewis Bumpy Torus Plasma Generated with High Positive or Negative Applied Potentials. Plasma Phys., vol. 19, no. 5, 1977, pp. 423-446. (Also NASA TN D-8211, 1976.)

28. Roth, J. Reece: Factors Affecting Ion Kinetic Temperature, Number Density, and Containment Time in the NASA Lewis Bumpy-Torus Plasma. NASA TN D-8466, 1977.

29. Roth, J. R.: Effects of Applied dc Radial Electric Fields on Particle Transport in a Bumpy Torus Plasma. IEEE Trans. Plasma Sci., vol. PS-6, no. 2, June 1978, pp. 158-165.

30. Powers, E. J.: Spectral Techniques for Experimental Investigation of Plasma Diffusion due to Polychromatic Fluctuations. Nucl. Fusion, vol. 14, no. 5, Nov. 1974, pp. 749-752.

31. Smith, D. E.; Powers, E. J.; and Caldwell, G. S.: Fast-Fourier-Transform Spectral Analysis Techniques as a Plasma Fluctuation Diagnostic Tool. IEEE Trans. Plasma Sci., vol. PS-2, no. 4, Dec. 1974, pp. 261-272.

32. Singh, Chandra M.; et al.: Fluctuation Spectra in the NASA Lewis Bumpy-Torus Plasma. NASA TP-1257, 1978.

33. Singh, Chandra M.; et al.: Low-Frequency Fluctuation Spectra and Associated Particle Transport in the NASA Lewis Bumpy-Torus Plasma. NASA TP-1258, 1978.

34. Roth, J. R.; et al.: Inward Transport of a Toroidally Confined Plasma Subject to Strong Radial Electric Fields. Phys. Rev. Lett., vol. 40, May 29, 1977, pp. 1450-1453. (Also NASA TM-73800, 1977.)

35. Roth, J. R.; et al.: A 12-Coil Superconducting Bumpy Torus Magnet Facility for Plasma Research. Fifth Applied Superconducting Conference, IEEE, Inc., 1972, pp. 361-366.

36. Roth, J. Reece; et al.: Characteristics and Performance of a Superconducting Bumpy-Torus Magnet Facility for Plasma Research. NASA TN D-7353, 1973.

37. Roth, J. Reece: A Model for Particle Confinement in a Toroidal Plasma Subject to Strong Radial Electric Fields. NASA TM X-73814, 1977.

38. Perkins, Raymond T.: Interpreting the Plasma Phase Shift of a Polarization-Diplexing Microwave Interferometer. M.S. Thesis, Brigham Young Univ., 1977.

39. Krawczonek, Walter M.; et al.: A Data Acquisition and Handling System for the Measurement of Radial Plasma Transport Rates. NASA TM-78849, 1977.

40. Roth, J. R.; and Krawczonek, W. M.: Paired Comparison Tests of the Relative Signals Detected by Capacitive and Floating Langmuir Probes in Turbulent Plasma from 0.2 to 10 MHz. Rev. Sci. Instrum., vol. 42, no. 5, May 1971, pp. 589-594.

41. Smith, D. E.; and Powers, E. J.: Experimental Determination of the Spectral Index of a Turbulent Plasma from Digitally Computed Power Spectra. Phys. Fluids, vol. 16, no. 8, Aug. 1973, pp. 1373-1374.

42. Kim, Y. C.; and Powers, E. J.: Effects of Frequency Averaging on Estimates of Plasma Wave Coherence Spectra. IEEE Trans. Plasma Sci., vol. PS-5, Mar. 1977, pp. 31-40.

43. Hedrick, C. L.; et al.: A Simple Neoclassical Point Model for Transport and Scaling in EBT. Nucl. Fusion, vol. 17, no. 6, 1977, pp. 1237-1243.

44. McBride, J. B.; and Sulton, A. L., Jr.: Stability of Neoclassical EBT Operating Points. Nucl. Fusion, vol. 18, no. 2, Feb. 1978, pp. 285-289.

45. Sprott, J. C.: Effect of Magnetic Field Errors on Confinement in Bumpy Tori. Phys. Fluids, vol. 16, no. 7, July 1973, pp. 1157-1159.

46. Quon, B. H.; et al.: Effects of Global Field Errors on ELMO Bumpy Torus. ORNL-TM-6075, Oak Ridge National Lab., 1977.

1. Report No.
NASA TP-1411

2. Government Accession No.

3. Recipient's Catalog No.

4. Title and Subtitle
ION CONFINEMENT AND TRANSPORT IN A TOROIDAL PLASMA WITH EXTERNALLY IMPOSED RADIAL ELECTRIC FIELDS

5. Report Date
March 1979

6. Performing Organization Code

7. Author(s)
J. Reece Roth, Walter M. Krawczonek, Edward J. Powers, Young C. Kim, and Jae Y. Hong

8. Performing Organization Report No.
E-9754

9. Performing Organization Name and Address
National Aeronautics and Space Administration
Lewis Research Center
Cleveland, Ohio 44135

10. Work Unit No.
506-25

11. Contract or Grant No.

12. Sponsoring Agency Name and Address
National Aeronautics and Space Administration
Washington, D. C. 20546

13. Type of Report and Period Covered
Technical Paper

14. Sponsoring Agency Code

15. Supplementary Notes
J. Reece Roth, Lewis Research Center (present address: Dept. of Electrical Engineering, University of Tennessee, Knoxville, Tenn.); Walter M. Krawczonek, Lewis Research Center; Edward J. Powers, Young C. Kim, and Jae Y. Hong, University of Texas, Austin, Texas

16. Abstract
In the NASA Lewis bumpy-torus experiment, strong electric fields were imposed along the minor radius of the toroidal plasma by biasing it with electrodes maintained at kilovolt potentials. Coherent, low-frequency disturbances characteristic of various magnetohydrodynamic instabilities were absent in the high-density, well-confined regime. High, direct-current radial electric fields with magnitudes up to 135 volts per centimeter penetrated inward to at least one-half the plasma radius. When the electric field pointed radially inward, the ion transport was inward against a strong local density gradient; and the plasma density and confinement time were significantly enhanced. The radial transport along the electric field appeared to be consistent with fluctuation-induced transport and not with either collisional Pedersen-currents or the collisionless $\nabla E$ mechanism described by Cole. With negative electrode polarity the particle confinement was consistent with a balance of two processes: a radial infusion of ions, in those sectors of the plasma not containing electrodes, that resulted from the radially inward electric fields; and ion losses to the electrodes, each of which acted as a sink and drew ions out of the plasma. A simple model of particle confinement was proposed in which the particle confinement time is proportional to the plasma volume. The scaling predicted by this model was consistent with experimental measurements.

17. Key Words (Suggested by Author(s))
Plasma diffusion; Plasma transport; Plasma confinement; Plasma instabilities; Plasma diagnostics; Radial diffusion; Radial transport

18. Distribution Statement
Unclassified - unlimited
STAR Category 75

19. Security Classif. (of this report)
Unclassified

20. Security Classif. (of this page)
Unclassified

21. No. of Pages
84

22. Price*
A05

* For sale by the National Technical Information Service, Springfield, Virginia 22161

NASA-Langley, 1979

National Aeronautics and
Space Administration

Washington, D.C.
20546

Official Business
Penalty for Private Use, $300

THIRD-CLASS BULK RATE

Postage and Fees Paid
National Aeronautics and
Space Administration
NASA-451

U.S.MAIL

2 1 1U,H, 021079 S00903DS
DEPT OF THE AIR FORCE
AF WEAPONS LABORATORY
ATTN: TECHNICAL LIBRARY (SUL)
KIRTLAND AFB NM 87117

S

NASA

POSTMASTER: If Undeliverable (Section 158 Postal Manual) Do Not Return